Experimental and Numerical Modeling of NOx Formation in Premixed Combustion of Pure and Renewable Liquid Fuels

Arshiya Hoseyni Chime

A dissertation submitted in partial fulfillment of the
requirements for the degree of

Doctor of Philosophy

University of Washington

2018

Reading Committee:

Philip Malte, Chair

John Kramlich

Megan Karalus

Program Authorized to Offer Degree:
Mechanical Engineering

University of Washington

Abstract

Experimental and Numerical Modeling of NOx Formation in Premixed Combustion of Pure and Renewable Liquid Fuels

Arshiya Hoseyni Chime

Chair of the Supervisory Committee:
Professor Philip Malte
Mechanical Engineering

A jet stirred reactor (JSR) is used to study the effects of fuel type and composition on NO_x emissions. The reactor temperature is varied from $1700K$ to $1900K$. Both pure and blended fuels are used in the experiments with the C/H ratio of fuels varying from 0.429 to 0.875. The fuels studied are: methane (as the baseline), n-hexane, n-octane, n-dodecane, isooctane, cyclo-hexane, toluene,1,3,5 tri-methyl benzene (135-TMB), jet-A, jet fuel made by Fischer-Tropsch processing of natural gas, and renewable jet fuel made from camelina, tallow, or bio-alcohol. The combustion of alternative and traditional commercial jet fuels show relatively minor differences in NO_x. The trend observed at three different temperatures of the recirculation zone shows: HRJ-tallow $<$ FT-natural gas $<$ alcohol-based jet$<$ HRJ-camelina. The largest difference in NO_x is between aliphatic and aromatic fuels. Aromatics produce about 30% more NO_x than aliphatic fuels.

A Computational Fluid Dynamic (CFD) model of the JSR is created to study the fluid structure and chemistry inside the reactor for gaseous fuels such as hydrogen and methane. Reynolds Average Navier Stokes (RANS) turbulence modeling is initially used for each case to develop a solution that is later utilized to initialize the Large Eddy Simulation (LES) modeling of the flow. Modeling chemistry correctly is essential for this study, therefore, the Complex Chemistry model with the Laminar Flame Concept (LFC) is utilized. This model

solves transport equations for species and calculates reaction rates by modified Arrhenius kinetic expressions. LES is used to determine the temperature and composition fluctuations in the recirculation zone, specifically at the location of sampling.

LES modeling of H_2 combustion with NO_x chemistry shows that most of the radicals are mainly formed in the flame brush. O-atom, H-atom, and OH radical have the highest concentrations in this region. These radicals react with nitrogen molecules and form important NO_x species such as N_2O, NNH, and NH. Since the concentration of O-atom and H-atom are highest in the flame brush, the Rate of Production (ROP) of NO_x species are highest in the flame brush as well. NO_x has the highest concentration in the recirculation zone due to the high residence time this zone provides. LES modeling of CH_4 combustion shows that the jet occupies a larger volume in the JSR compared to the jet observed in the combustion of hydrogen. This is due to the slower chemistry of methane compared to hydrogen.

Based on the CFD results, chemical kinetic modeling is performed to study NO_x formation from liquid fuel combustion. A 3-zone chemical reactor network (CRN) model is developed and implemented to model the flame zones inside the JSR. The goal of this work is to predict emissions and explain the experimental trends observed for combustion of fuels such as methane, iso-octane, n-octane, n-dodecane, 135-trimethylbenzene (TMB), and toluene. Two sets of hydrocarbon mechanisms are utilized in the CRN model, the individual fuel hydrocarbon mechanisms and a surrogate jet fuel mechanism. NO_x is modeled using 2011 Klippenstein et al. H-N-O mechanism as well as two different prompt mechanisms of Konnov and Glarborg et al. The following findings are observed by analyzing the results of the CRN modeling. NO_x is predicted well when the individual fuel hydrocarbon mechanisms or the surrogate jet fuel mechanism are used with Klippenstein et al. H-N-O and Konnov prompt NO_x mechanisms. These emissions are slightly under-predicted for n-alkanes and iso-octane. These results are consistent among three different recirculation zone temperatures of 1700, 1800, and 1900 K. Sensitivity analysis on NO_x pathways shows that N_2O is the

major pathway to NO_x formation in the JSR at the recirculation zone temperature of 1800K. The Zeldovich route is the second most important route followed by the prompt pathway. The NNH route has a small contribution to overall NO_x for these fuels in the lean premixed combustion of these fuels. Aromatic fuels emit more CO and NO_x compared to aliphatic fuels as shown in both the experiments and the models. CRN results show that this is due to the higher concentrations of O-atom and H-atom present. Having a higher concentration of CO available produces more H-atom from oxidation of CO by the OH radical. The higher concentration of H radical promotes higher O-atom production from the oxidation of H-atom with oxygen. Higher H-atom and O-atom concentrations lead to higher NO_x production for aromatics compared to aliphatics.

TABLE OF CONTENTS

LIST OF TABLES

LIST OF FIGURES

ACKNOWLEDGMENTS

This journey has been full of adventures, challenges, and growth. I would like to acknowledge people who made it all possible.

Firstly, I want to express my sincere gratitude to my advisor Professor Philip Malte. It has been an honor to learn from one of the best in the field of experimental combustion and kinetic modeling. I always enjoyed our conversations about research, politics, and life. Thank you for all your care, patience, and encouragement. I am deeply grateful to Professor Kramlich for his guidance, mentoring, and meaningful conversations that we have had. I also wish to thank Professor Riley for answering my endless questions about turbulence modeling and teaching me about humility. I appreciate the mentoring and support of Dr. Megan Karalus throughout my journey in graduate school. I would also like to thank Wanwisa Kisalang for her unlimited support as my graduate academic advisor.

Financial support for this project was provided by the State of Washington JCATI (Joint Center for Aerospace Technology Innovation) program, Zonta International Amelia Earhart Fellowship, and the support of the Mechanical Engineering department at University of Washington through teaching assistantships, instructor positions, and fellowships. This work would have not been possible without the use of advanced computational, storage, and networking infrastructure provided by the HYAK supercomputer system at University of Washington.

My gratitude extends to Professor Tom Acker for introducing me to the field of renewable energy and giving me the opportunity to do research in this field as an undergraduate student at Northern Arizona University. I am also deeply grateful to Coach Saatara for providing me with the opportunity to pursue my dream of being a student-athlete in the U.S.

I wish to thank all my friends who made Seattle (and Flagstaff) feel like home without the presence of my family, for being there for me in both joyous and gloomy days, and for providing advice and support throughout this journey. Their friendship means the world to me. Thank you to my parents and sisters for teaching me selfless love, for inspiring me to pursue big dreams, and for building the foundation to my success. Finally, I owe thanks to the love of my life, Terrence, for his endless love and support, for bringing a smile on my face everyday, for teaching me to slow down and enjoy the moment, and for dreaming of building a beautiful future together.

DEDICATION

To my mom, who taught me perseverance and dedication.

To my sister, Mahsa, who fills my life with love.

To my sister, Atoosa, who dedicated her life to my success.

To my sister, Niyousha, who inspired me to become an engineer.

Chapter 1

INTRODUCTION

1.1 Overview and Motivation

Over the past few decades, gas turbines have become a dominant source of power for large scale power generation and for mechanical drive applications. Factors that have resulted in this increased utilization include their improved thermal efficiency, availability, and the ability to operate on a wide spectrum of gaseous and liquid fuels. While natural gas has been the fuel of choice, there is a large population of engines worldwide that burn liquid fuels. Liquid fuels play an important role in transportation and the manufacturing industry due to their high energy density. Environmental concerns have incentivized the search for renewable fuels. However, any potential alternatives must be thoroughly characterized and tested for emissions, sooting tendency, thermal stability, and seal/materials compatibility.

Gas turbine combustors are complex devices. They include a primary zone, intermediate zone, and dilution zone. The fluid dynamics and chemistry in each zone are complicated which makes it difficult to study the relation between fuels, flame stability, and emissions. In order to reduce complexity and number of parameters, a Jet Stirred Reactor (JSR) is used in this study which serves as the laboratory-scale idealization of the primary zone of a gas turbine engine. JSRs have been used since the 1950's to isolate temperature and fuel chemistry to study the effects of different fuels on blowout and emission production.

Natural gas fired gas turbine engines used for power generation and mechanical drive have undergone a major improvement in NO_x emissions over the past twenty years. The engines have changed from high-NO_x diffusion flame combustors to low-NO_x lean-premixed combustors resulting in a 10 to 30 fold decrease in NO_x. The remaining challenge is the liquid-fired gas turbine engine, especially the aero engine is to what extent can lean com-

bustion and premixing be used to control the NO_x of these engines, while retaining the exceptional flame stability required of aero engines.

The present study aims to examine NO_x emissions of pure and surrogate liquid fuels under lean, premixed combustion conditions both experimentally and numerically at a given temperature and fuel-air equivalence ratio. A wide range of pure and renewable/alternative fuels are used in the experiments to study lean-flame NO_x behavior. In order to obtain a better understanding of the fluid structure in the JSR, a CFD-LES model of the reactor is developed for gaseous fuels. This model is then used to develop a Chemical Reactor Network (CRN) model of the JSR that allows one to explore emissions using detailed combustion chemistry of liquid fuels.

1.2 Literature Review

1.2.1 Oxides of Nitrogen

Oxides of nitrogen are formed during the combustion process mainly as a result of chemical reactions of oxygen and nitrogen. The oxides of nitrogen, NO_x, collectively refer to as the sum of nitric oxide (NO) and nitrogen dioxide (NO_2). Emissions of these species are precursors to photochemical smog and acid rain once in the atmosphere.

There are five major NO_x formation pathways: (1) Zeldovich [88], (2) N_2O [54], (3) NNH [10], (4) prompt [27], and (5) the oxidation of fuel bound nitrogen. All fuels that are studied here are free of fuel-bound nitrogen, therefore, the fifth pathway is neglected.

- The Zeldovich pathway contains the principal reactions governing the formation of NO from molecular nitrogen and oxygen during the combustion of the fuel-air mixture. This pathway is extended to include the reaction of OH radical with N-atom which is mostly important near-stoichiometric and rich conditions. The formation of Zeldovich NO_x is highly temperature-dependent and contributes most under high temperature combustion processes.

$$\begin{aligned} N_2 + O &\iff N + NO \\ N + O_2 &\iff NO + O \\ N + OH &\iff NO + H \end{aligned} \tag{1.1}$$

- The N_2O pathway was proposed by Malte and Pratt [54] to explain pathways for formation of NO_x in high-intensity, lean, premixed combustion. N_2O is mainly formed by reaction of nitrogen with O-atom and a third-body. This intermediate specie, N_2O, reacts with H-atom and O-atom to form NO as shown below.

$$\begin{aligned} N_2 + O + M &\iff N_2O + M \\ NH + NO &\iff N_2O + H \\ N_2O + O &\iff NO + NO \end{aligned} \tag{1.2}$$

- The NNH pathway is an additional pathway to NO_x formation. The NNH molecule is mainly produced by the reaction of H-atom and nitrogen molecules. NNH then reacts with O-atom to create NH and NO. Additionally, NNH reacts with O-atom to form N_2O as shown below. This is an important reaction for formation of N_2O

$$\begin{aligned} N_2 + H &\iff NNH \\ NNH + O &\iff NH + NO \\ NNH + O &\iff N_2O + H \end{aligned} \tag{1.3}$$

- The prompt pathway was proposed by Fenimore in 1971. This is the specific pathway that forms NO via N_2 reacting with hydrocarbon radicals. This NO is formed rapidly in the flame front long before there is time for it to via the Zeldovich pathway. Previously, it was thought that the pathway was initiated from a CH radical reacting with nitrogen to produce HCN and N-atom. More recent studies however suggest

that reaction is spin forbidden. An alternative initiation reaction is proposed to be $CH + N_2 \iff NCN + H$ [39]. This is discussed in more detail in Chapter 4.

Each reaction in these mechanisms is represented by the modified Arrhenius expression shown in Equation 4.1. In this equation, A is the pre-exponential constant with unit of $[moles - cm - s - K]$, E_A is activation energy with unit of $[cal/mol]$, T is temperature in $[K]$, and k is the reaction rate.

$$k = A\ T^b exp(-\frac{E_A}{RT}) \tag{1.4}$$

1.2.2 Renewable/Alternative Fuel Combustion

Emissions from alternative jet fuels have been studied and compared to conventional jet fuels. Multiple studies by the Air Force Research Laboratories (Monroig et al. [59], Cain et al. [12], DeWitt et al. [17], Corporan et al. [13, 14], and Klingshirn et al. [37]) were performed using an Allison T63 turboshaft engine and a laboratory scale combustor.

Corporan et al. [13, 14] studied six alternative jet fuels derived from different feedstocks such as coal, natural gas, camelina, and animal fat (Fischer-Tropsch and hydro-processing methods). Chemical analyses showed that these alternative fuels were comprised of mostly paraffinic compounds with negligible aromatic content. Material capability tests showed that the alternative fuels possess significant seal swelling capability in conditioned nitrile O-rings, however, elastomer swelling was significantly lower than for JP-8 [17].

Cain et al. [12] and DeWitt et al. [17] examined the operability and gaseous (CO and CO_2) and particulate matter emissions of JP8 and a synthetic fuel derived from Fischer-Tropsch processing of coal as well as four different surrogate mixtures of the two fuels. Paraffinic fuels were found to produce significantly lower Particle Matter (PM) emissions than fuels containing aromatic compounds. Additionally, major gaseous emissions were only slightly affected, with trends consistent with that expected based on the overall hydrogen content of

the fuels (JP8 producing the highest levels of emissions). However, minor hydrocarbon and aldehyde emissions were significantly more sensitive to the fuel composition. The speciated aromatic emissions were highly sensitive to chemical composition, as evidenced by their high formation rates from fuels that contained aromatics or had high selectivity to produce reactive intermediates prone to ring closure and addition.

Klingshirn et al. [37] and Monroig et al. [59] further studied blends of JP-8 with hydro-processed tallow and camelina as well as 135- trimethylbenzene (TMB) blended with tallow. This study also showed that aromatic content in the fuels increases soot emission.

Some studies measured NO_x emissions from combustion of alternative and traditional jet fuels and their surrogates. Timko et al. [79, 80] found changes in NO_x that they attributed to small variations in temperature or NO_x decrease due to the presence of high concentrations of fatty acid methyl esters (FAMEs) and their effect on flame structure. Two studies (Moses and Roets [60] and Lobo et al. [50]) found decreased NO_x emissions from coal-based synthetic fuels compared to Jet A-1. Moses and Roets [60] found that there was not much difference between lean flame blowout characteristic of coal-based synthetic fuel and Jet A -1.

Khandelwal et al. [36] found that synthetic fuels blended with aromatic additives produced marginally less NO_x emissions. Emissions data demonstrated that the alternative fuels produced significantly lower soot and moderately lower unburned hydrocarbons and carbon monoxide than baseline JP-8 fuel.

Blust et al. [6, 7] used a toroidal jet stirred reactor to study NO_x, CO, and UHC emissions as well as flame stability for fuels such as n-dodecane, cyclo-hexane, toluene and jet-A. They found that hydrocarbon structure and C/H ratio produce different NO_x emissions for temperatures above 1800 K and the same residence time, and that increased residence time increased NO_x production. One of the important results found was that aliphatic fuels produced less NO_x than aromatics and cycloalkanes. Blust et al. [6, 7] also performed lean-blow out experiments using a toroidal jet stirred reactor. The experiments showed that Jet-A and cyclohexane had the highest flame stability while the flames of toluene and n-dodecane

blew out at higher temperatures respectively.

In 2000, Lee et al. [48] published a study that analyzed a range of aliphatic and aromatic fuels under lean pre-mixed and pre-vaporized conditions using a jet-stirred reactor (JSR) at a fixed temperature. The liquid fuels burned were methanol, normal alkanes from pentane to hexadecane, benzene, toluene, two grades of light naphtha and four grades of No. 2 diesel fuel. A staged prevaporizer-premixer (SPP) was utilized to reduce the emissions of NO_x. NO_x and CO emissions were measured and found to correlate with the carbon to hydrogen ratio of the fuel. NO_x emissions increased linearly as the carbon to hydrogen ratio of the fuels increased. It was also found that aromatic fuels emit higher levels of NO_x. CO emissions showed similar trend as NO_x emissions.

Later in 2014, NO_x emissions of alternative jet fuels blended with different amounts of aromatic fuel were tested by Vijlee [83] in the JSR of Lee. Vijlee studied four synthetic fuels made from Fischer-Tropsch or hydro-processing methods. The experiments showed that NO_x has the following order for synthetic fuels: HP Camelina > FT Coal > FT Natural Gas > HP Tallow. JP-8 was also used in the experiments for comparison with alternative and aromatic fuel blends. The differences in NO_x emissions between the fuels tested was small. The blends of aromatic with the synthetic fuels did not show a clear trend in NO_x with added aromatic in the 10-20% (by weight) range.

Vijlee [84] also used a toroidal reactor to measure flame stability of alternative/synthetic jet fuels. He showed that blowout temperature and fuel-air equivalence ratio of these fuels did not show much variation. However, aromatic fuels had a lower resistance to flame blowout.

1.2.3 Chemical Kinetic Modeling

In 2000, Rutar and Malte [73] and [72] used a High-Pressure JSR (HP-JSR) to measure NO_x and CO in methane-fired, lean-premixed combustion. These measurements were then compared to a simple chemical reactor model that utilized the GRI3.0 mechanism. A single perfectly stirred reactor (PSR) or two PSRs in series were used. When the residence time was short, and thus, the velocities in the reactor were high, estimates of the turbulent flame

thickness indicated the turbulent flame zone fully filled the HP-JSR. Under this condition, the NO_x and CO were well modeled assuming the full reactor to be a single perfectly stirred reactor. For long residence times, velocity is relatively low in the reactor and in this case the flame zone is situated around the center jet of the reactor and is surrounded by the recirculation zone of the reactor. In this case, an adiabatic PSR represented a small flame zone followed by another PSR which represented a large post-flame zone. The results showed that Fenimore prompt pathway was significant when the fuel-air equivalence ratio was higher than 0.7 or when the residence time of the flame zone was very short. This was determined to be the consequence of the short lifetime of the CH radical in flames. NO_x formed by the prompt pathway played a significant role in such high pressure conditions.

In 2006, Rutar et al. [71] modeled gaseous and liquid fuels, with C/H ratios varying from 0.25 to 0.88, tested by Lee in two JSRs: 1) the 15.8 cc JSR of Lee [47] and 2) a geometrically similar JSR of 64 cc volume (nominal residence times of 2 and 4 ms, respectively). The authors used 2, 3 or 4 PSRs in series depending on how well experimental NO_x and CO matched the modeling results. Several volume variations were studied for each fuel. It was found that for methanol and toluene a PSR+PSR model had the closest agreement with the experiments since a single PSR or 3 PSR models over predicted or under predicted NO_x and CO. Other fuels studied such as methane, ethane, propane, n-butane, and ethene used a 3 PSR model. Toluene showed the best match with experiment with the ratio of PSR to total volume, V_{PSR}/V_{total}, of 30/70. NNH pathway to NO_x formation was significant for this fuel followed by N_2O, Zeldovich, and the Fenimore prompt.

The 15.8 cc JSR of Lee [47] is used in the present study, with the 4 mm jet of Lee replaced with a 2 mm jet. The Lee JSR with a 2 mm jet was used by Fackler [25] and Vijlee [83]. Fackler [25] modeled this reactor using CFD. Fackler used 3D Reynolds-Average Navier-Stokes (RANS) with the 9-equations Reynolds Stress Model and the eddy dissipation concept (EDC) model [52] for turbulence-chemistry interaction. A 3-step global mechanism of Nicol et al. [64] for methane was used. The CFD results were used to create a 3-zone CRN for predicting NO_x formation of alternative gaseous fuels which included mixtures of methane

and hydrogen. Experimental results and chemical kinetic modeling were in best agreement when the Konnov and Ruyck [40] rate data for the reaction $NNH + O \longrightarrow NO + NH$ were substituted into GRI 3.0 [9].

1.2.4 CFD and Turbulence Modeling

With the increase in computing power, Large Eddy Simulation (LES), emerges as a promising technique to improve both knowledge of complex physics and reliability of flow solver predictions. In computational expense, LES lies between Reynolds-stress models and Direct Numerical Simulations (DNS), and it is motivated by the limitations of each of these approaches. DNS involves solving Navier-Stokes equations while resolving all scales of motion. This modeling approach is the simplest conceptually but its computational cost is extremely high. The computer requirement increases with the cube of the Reynolds number which limits the applicability of this approach when modeling a turbulent jet. On the other hand, Reynolds-Averaged Navier-Stoke (RANS) are computationally cheap but only predict the time-averaged effects of unsteady flows. Even in unsteady RANS all turbulent scales are modeled so turbulence is not directly represented. Because the large-scale unsteady motions are represented explicitly in LES, it can be expected to be more accurate and reliable than Reynolds-stress models.

A filtering operation is used to derive the governing equations for LES. This decomposes the major variables into a filtered (resolved) component, $\hat{\mathbf{U}}(\mathbf{x}, t)$, and a residual (or subgrid-scale, SGS) component,$\mathbf{u}'(\mathbf{x}, t)$.

$$\mathbf{U}(\mathbf{x}, t) = \hat{\mathbf{U}}(\mathbf{x}, t) + \mathbf{u}'(\mathbf{x}, t) \tag{1.5}$$

The governing equations are derived for evolution of resolved major variables (velocity, temperature, density, etc.) by filtering the Navier-Stokes equations. These equations contain

residual components such as residual stress tensor or subgrid scale stress tensor ($(\tau_{ij})_{sgs}$).

$$(\tau_{ij})_{sgs} = 2\mu_{sgs}S_{ij} \tag{1.6}$$

In this equation, μ_{sgs} is the subgrid scale viscosity and S_{ij} is the strain rate tensor. This tensor must be modeled to achieve closure. The simplest model is the Smagorinsky subgrid scale model where a mixing length hypothesis is used to model the subgrid scale stress tensor [69]. A more modern subgrid scale model is WALE (wall-adapting local-eddy viscosity) subgrid scale model. In this model, the SGS stress tensor is solved algebraically. This is preferred over the Smagorinsky SGS model because of its lower computational cost and equivalent accuracy. Similar to Smagorinsky subsgrid scale model, WALE model suffers from the limitation that the model coefficient, C_w in equation 1.8, is not universal. Validation studies by Simcenter STAR-CCM+ has shown that the WALE model is less sensitive to this coefficient compared to Smagorinsky model. Another advantage of the WALE model is that it does not require any form of near-wall damping as it automatically gives accurate scaling at walls [77].

The subgrid scale viscosity in the subgrid scale tensor, (μ_{sgs}, of equation 1.6) is modeled as the following in the WALE subgrid scale model.

$$\mu_{sgs} = \rho\triangle^2 S_w \tag{1.7}$$

where ρ is the density, $\triangle$ is the grid filter width as defined in Equation 1.8, and S_w is the tensor defined in Equation 1.9.

$$\triangle = C_w V^{1/3} \tag{1.8}$$

In this equation V represents the cell volume and $C_w = 0.544$

$$S_w = \frac{(S_{ij}^d S_{ij}^d)^{3/2}}{(S_{ij}^d S_{ij}^d)^{5/4} + (S_{ij} S_{ij})^{5/2}} \tag{1.9}$$

The accuracy of an LES simulations relies on the resolution of the mesh. By using proper low-pass filtering, scales lower than the mesh length or filter width, $\triangle$, are eliminated and suitable equations for large scales are developed for solving the flow property variations in both time and spatial variables. This means all wave numbers lower than the cut off wave number, $\kappa_c = \frac{2\pi}{\triangle}$ are resolved and the rest are modeled as illustrated in Figure 1.1. Based on Pope Criterion [68], the subgrid region holds only about 5% of total energy of the spectral space for a well-resolved LES.

combustion models are broken down into tabulated chemistry models, and species transport models. Two common methods for modeling combustion in gas turbines are Flamelet Generated Manifold (FGM) and the Complex Chemistry. The FGM model tabulates chemistry for mixture fraction, mixture fraction variance, progress variable, progress variable variance, and heat loss ratio. The Complex Chemistry model solves transport equations for all species and integrates the chemistry during the calculations. The FGM model is faster than Complex Chemistry but the accuracy of the models depend on the application.

Mallouppas et al. [53] examined the performance of the Flamelet Generated Manifold (FGM) model vs Laminar Flame Concept (LFC) with the Complex Chemistry model using LES modeling for a natural gas/air premixed swirl flame industrial gas turbine. The FGM model is a tabulated chemistry approach while LFC with Complex Chemistry solves species transport equations and integrates the chemistry during the calculation. They further compared the predicted pollutant formation (NO and CO emissions) obtained by these models to experiments. The experimental and computational work used the Siemens SGT-100 Dry Low Emission gas turbine at 3 bar with premixed natural gas and air. This work showed that mixture fraction was consistently over-predicted using both FGM and LFC, but values

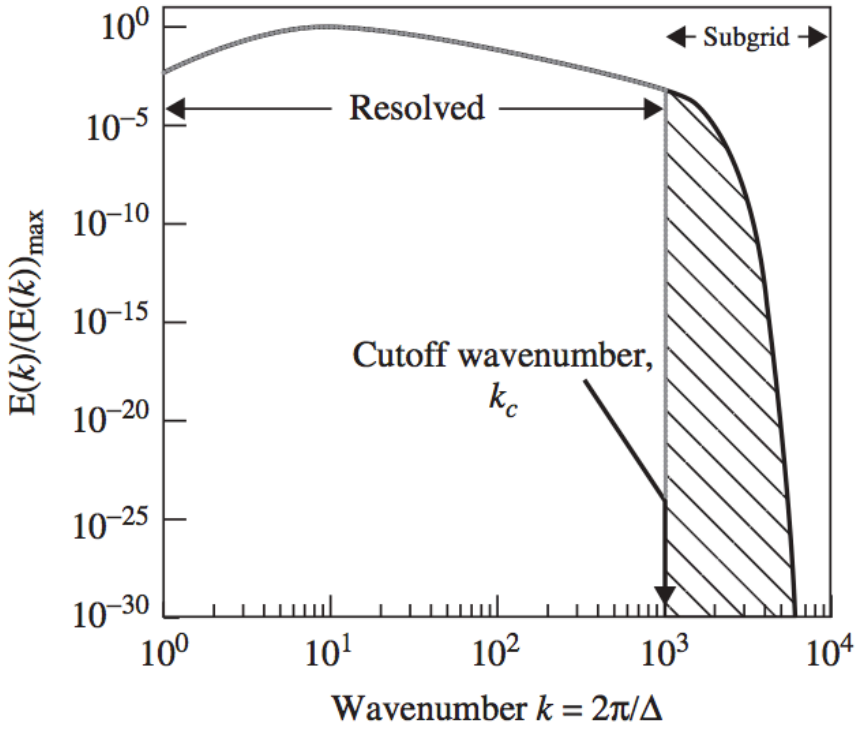

Figure 1.1: Spectral space with an example of cut off wavelength. The subgrid region is presented with hatched lines [42]

where within experimental error. It was found that the velocity field predicted using CFD was in agreement with measurements, where the recirculation and shear zone structures were captured correctly. FGM and LFC both over-predicted CO and NO levels.

Previously, Bulat et al. [11] used the same rig and experimental data as Mallouppas et al. [53] to model the gas turbine using LES with the Eulerian stochastic subgrid PDF method. In this method, subgrid stresses are represented by a dynamic version of the Smagorinsky model and subgrid species fluctuations are characterized by eight stochastic fields. Bulat et al. [11] showed that using LES with a 4-step global mechanism of Jones and Lindstedt [33] predicted mean and RMS velocity fields well compared to PIV measurements. However, temperature and species fields were over-predicted and flame location was predicted incorrectly compared

to 1D Raman Scattering data. For this reason, additional chemistry was included by using a reduced GRI 3.0 mechanism with 15 reaction steps and 19 species of Sung et el.[78]. With this, an accurate simulation of the flow field, temperature and species concentration was achieved.

Bulat et al. [11] performed LES modeling that showed that the rates of production of NO were relatively small compared to CO and OH, however, NO production was concentrated in small pockets in the flame region or in the vicinity of the flame front. Overall, the measured emission levels of NO were reproduced to a good accuracy. Prompt pathway dominated NO production with some influence from thermal NO_x. However, N_2O pathway constitutes only 5% of the total NO formation.

1.3 Research Objectives

The literature review shows that diffusion flame combustors are mainly used to study the emissions and flame stability of renewable/alternative fuels. Only a limited amount of information is available for NO_x emissions and flame stability of pure and renewable/alternative jet fuels under lean-premixed combustion such as the work of Vijlee [83]. Chapter 2 in this dissertation aims to fill this gap in the literature.

Another possible gap in the literature is studying the effects of temperature and species fluctuations on NO_x formation in the recirculation zone of a JSR. Previous CFD simulations of the JSR by Fackler [24] and Karalus [34] used the RANS turbulence model which only provides the mean fields. In this work, LES modeling of a JSR is performed in Chapter 3 and the importance of unsteady behavior of temperature and species with respect to NO_x formation are discussed.

Further contribution to the literature is provided by analyzing the reaction pathways to NO_x formation for pure liquid fuels. This information is largely missing in the literature. Chapter 4 of this dissertation uses chemical kinetic modeling to provide information about the importance of various NO_x mechanisms in the JSR and attempts to explain the difference in NO_x emissions of aliphatic and aromatic fuels.

The research objectives are summarized below:

- Experimentally determine lean-premixed NO_x emissions of a wide range of pure and renewable/alternative fuels burned in the JSR at a fixed temperature. These experiments are performed for recirculation zone temperatures of 1700, 1800, and 1900 K. Methane is used as a reference fuel.

- Simulate the flow inside the JSR using CFD for simple gaseous fuels while utilizing the LES turbulence model along with Complex Chemistry and laminar flame concept to explore the temperature and species fluctuations in the sampling region. NO_x chemistry is included in the case of hydrogen combustion to study the formation/destruction of important nitrogen species.

- Utilize the CFD findings to develop a CRN model that best characterizes the zones inside the JSR. This CRN model is used to explain the trends seen in NO_x emissions for pure liquid fuels. Various well-stablished hydrocarbon fuel and NO_x mechanisms are used for CRN modeling and comparison among them is performed. Contribution of various NO_x pathways is examined for combustion of pure liquid fuel. Attention is also directed to modeling the greater amount of NO_x formed by single-ring aromatic fuels compared to the liquid aliphatic fuels tested.

Chapter 2

EXPERIMENTAL WORK

The experimental work mainly focuses on measuring NO_x emissions at three different fixed temperatures in the range of 1700K-1900K and finding the lean-flame blowout (LFBO) temperature for renewable and pure liquid fuels. This chapter describes the experimental setup, the measurement tools used, and presents the data obtained. Finally, the experimental data are analyzed and further conclusions are made.

2.1 Experimental setup and procedure

The experiments utilize a single-jet JSR and staged pre-vaporizer premixer (SPP) designed and fabricated by Lee [47]. This reactor is made of cast alumina (Al_2O_3) that rests on an Inconel nozzle block with a nozzle diameter of 2 mm. A CAD drawing of the JSR is provided in Figure 2.1. The height of the reactor is about 45.5 mm and the radius is 12.5 mm at the widest section. The volume of the reactor is 15.8 cm^3 (i.e., the combustion volume). Detailed drawings of the JSR can be found in the work of Lee [47].

There are four measuring access ports in the reactor, but only two are used in the present work to measure the temperature using a thermocouple and the sample gases using a gas sampling probe. The other two ports are plugged during experiments with ceramic tubes to avoid heat loss. There are four exhaust ports (only two shown in Figure 2.1) with the diameter of about 1 mm each.

Air enters the combustion rig from three stages as seen in Figure 2.2. Initially, air enters the rig at 30 $PSIG$ and room temperature for light-off. Hydrogen at 35 $PSIG$ is injected into the reactor from the gaseous fuel inlet for light-off. Due to the long period of time that is required for the reactor to reach a steady state temperature, inexpensive propane is used to

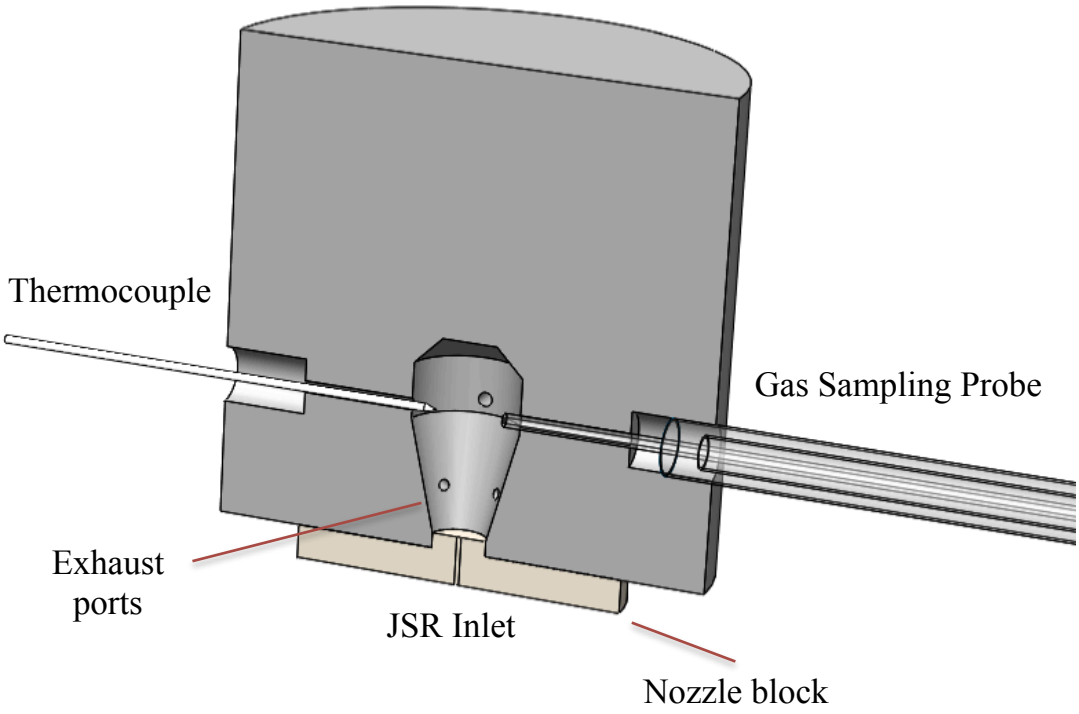

Figure 2.1: Slice of the JSR with thermocouple and quartz gas sampling probe.

warm up the reactor. Once a stable flame is obtained inside the JSR, a smooth fuel transition from hydrogen to propane is performed by lowering the mass flow rate of hydrogen, while increasing propane.

While the reactor warms up using propane, air is heated at two stages using in-line pipe heaters before entering the SPP as shown in Figure 2.2. Both in-line pipe heaters are Convectronics $1/2''$ NPT steel heaters (Part No.007-10135) that are fed with Powerstat $120V$ variable autotransformers. The heaters raise the temperature of the 1^{st} and 2^{nd} stage air to about 320°C.

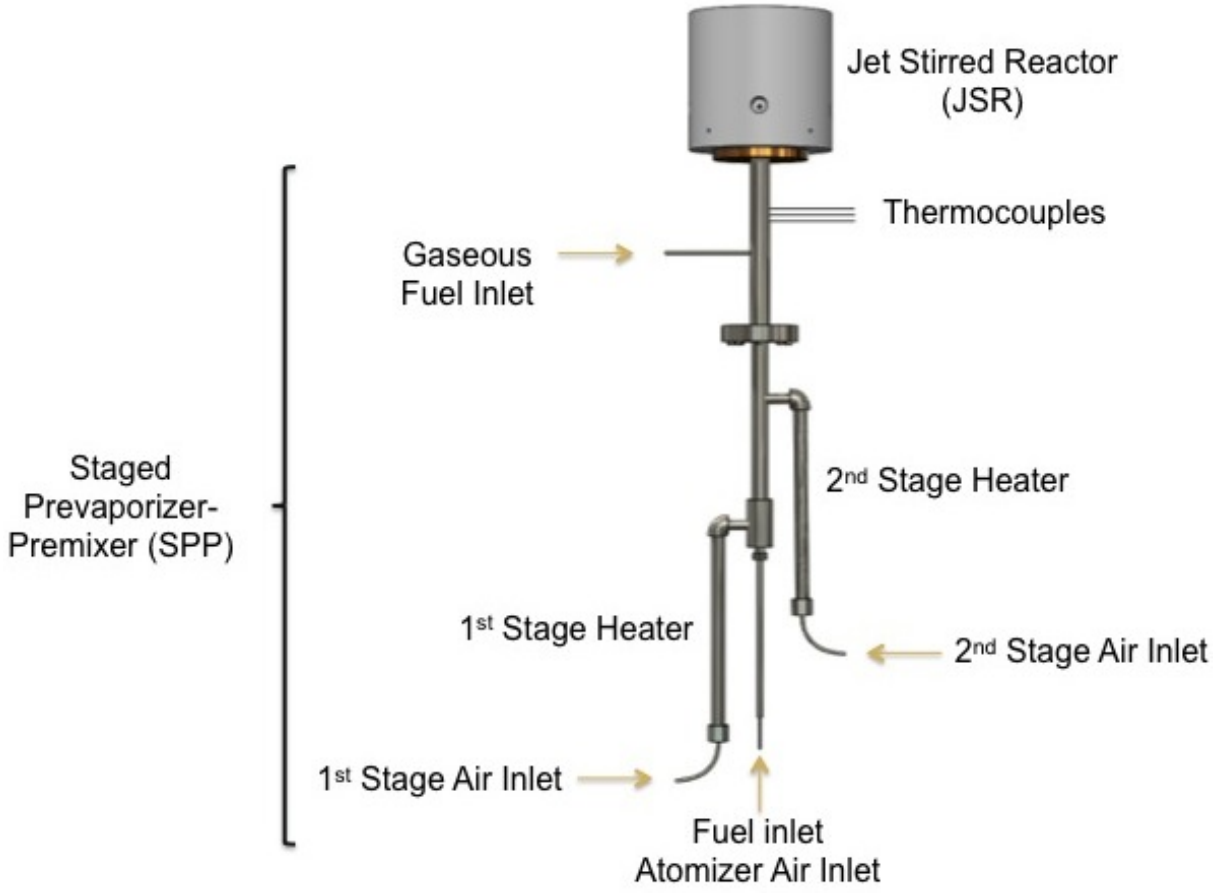

Figure 2.2: Slice of the JSR with thermocouple and quartz gas sampling probe.

Once the temperature inside the reactor reaches steady state (around $1700K$), liquid fuel is pressurized in the fuel tank to 60 $PSIG$ using nitrogen. The fuel passes through a $15\mu m$ filter (Swagelok Part No. SS-4F-15) before passing through the fuel rotameter and then is injected into the plane jet atomizer design by Lee [45]. Air at room temperature is delivered to the plane jet atomizer at 48 $PSIG$. The atomized fuel and air mixture enter the first stage of the SPP. Air from the 1^{st} stage vaporizes the liquid fuel and mixes with warm air from the 2^{nd} stage. The temperature of the prevaporized-premixed fuel and air is measured using three thermocouples before it enters the JSR as shown in Figure 2.2.

Premixed fuel and air enter the JSR at a nominal temperature of 350 °C ($605K$) through

a choked 2 mm diameter nozzle with a sonic jet velocity of approximately 450 m/s (according to Fackler [24] and Karalus [34]). The total mass flow rate of air entering the JSR is kept at 1.05 g/s while the mass flow rate of fuel is varied to change the temperature of the JSR. The nominal residence time inside the JSR is 3 ms, with a variation from 2.8 to 3.1 ms for the temperature range. The JSR operates lean-premixed at a nominal pressure of 1 atm. A summary of the JSR operating conditions is given in Table 2.1.

Condition	Value
Reactor Volume	15.8 (m^3)
Mass Flow rate of Air	1.05 g/s
Residence time	$2.8 - 3.1ms$
Temperature (measured in the recirculation zone)	$1700K - 1900K$
Reactor Nominal Pressure	1 atm
Unburnt Premix Temperature	605 K

Table 2.1: Summary of experimental conditions.

Thermocouple and gas sampling probes are inserted into the JSR from two different ports but placed at the same reactor height and radius as shown in Figure 2.1. The tips of these two probes are 10 mm from the centerline at 2/3 height of the JSR. This location is in the recirculation zone of the JSR, outside of the wall boundary layer.

The temperature of the combustion gases is measured with an R-type thermocouple with its tip coated with a thin layer of cast alumina to prevent catalytic surface reactions. The measured temperature is affected by the convection from the combustion gases and losses due to radiation from the thermocouple to the reactor walls. Heat transfer analysis by Vijlee [83] has shown that the measured combustion temperature is nominally 40 degrees cooler than the reported thermocouple temperature (when the recirculation gas temperature is 1800 K). Equation 2.1 shows the correction to the temperature of the R-type thermocouple to

find the correct combustion temperature [83]. In this equation, T is the raw thermocouple temperature and $T_{corrected}$ is the corrected thermocouple temperature.

$$T_{corrected} = 1.0621T - 66.55 \tag{2.1}$$

Combustion gases are extracted using a warm water-cooled quartz probe. The probe's orifice is roughly 0.03 $inch$ in diameter with an uncooled portion at the tip which is an inch long. Since most of the NO_x formed in the JSR converts to NO_2 in the sample probe, care is taken to prevent loss of NO_2 to the water of combustion in the sample line and knock-out water trap [41]. Sample gases are pumped through $1/4''$ Teflon lines that are heated using heating tapes to two quartz impingers that are housed in s in an ice-bath to remove the water vapor.

The dry sample gases are then pumped to a multi-gas analyzer that measures CO, CO_2, and O_2, and a NO_x/NO analyzer. The CO and CO_2 analyzers are NDIR, the O_2 analyzer is paramagnetic, and the NO_x analyzer is chemiluminescent. Experiments by Gandara et al. [29], using a vitreous carbon converter placed immediately downstream of the sample probe indicated very little loss of NO_2 in the JSR sampling system used here. The vitreous carbon converted all of the probe NO_2 output to NO. The NO measured with the pre-converter installed was nearly equal (i.e., 2% higher) than the NO_x measured by the conventional sampling system used here [29]. Each analyzer is calibrated multiple times before, during, and after the experiments to ensure reliability of measured concentration. A summary of span gases used to calibrate these analyzers is given in the Table 2.2.

Emissions	Analyzer	Span Gas (% by volume)	Zero Gas
CO	Horiba VA-3000	0.15%	N_2
CO_2	Horiba VA-3000	1.9%	N_2
O_2	Horiba VA-3000	8%	N_2
NO_x	CAI 600 Series	9.14% and 22.4%	N_2

Table 2.2: Gas analyzers used to measure emissions and the span gases used to calibrate them.

2.2 Fuels

Both pure and blended fuels are used in the experiments with C/H ratios of fuels varying from 0.25 to 0.875. A list of all fuels with their corresponding chemical formulas is provided in Table 2.3. Methane, n-hexane, n-octane, cyclo-hexane, iso-octane (2,2,4 trimethyl pentane), n-dodecane, 1,3,5 trimethylbenzene (135-TMB), and toluene are pure fuels from petroleum. All of the single-component liquid fuels are purchased with 99% purity from Sigma-Aldrich.

The rest of the fuels are blended types with different processing methods. Renewable jet fuels such as HRJ-tallow and HRJ-camelina are among the synthetic fuels that are made using the hydroprocessing of animal fat and camelina seeds, respectively. Another synthetic fuel is Fischer Tropsch Natural Gas (FT-Natural Gas), which is produced by Fischer Tropsch synthesis of natural gas. The bio-alcohol based renewable jet fuel (alcohol-based jet) is made by first generating sugars from biomass, then fermenting the sugars to alcohol, and processing the alcohol to liquid fuel suitable for aviation. These jet fuels were obtained from the Air Force Research Laboratory (AFRL) [21].

The only petroleum-based blended fuel is Jet-A, which is used for commercial aircraft purposes. The two pure aromatic fuels tested are 135-TMB and toluene. Aviation fuels typically contain 10-20% aromatic compounds. Aromatic compounds are essential in jet fuels for proper operation of the fuel systems. The fuel system contains o-rings and gaskets

	Formula	C/H	LHV [MJ/kg]	MW $[kg/kmol]$	Density $[kg/m^3]$	$(\dot{m}_f/\dot{m}_a)_{st}$
Methane	CH_4	0.25	50	16	0.663	0.0581
n-Hexane	C_6H_{14}	0.429	44.7	86	655	0.0657
n-Octane	C_8H_{18}	0.444	44.4	114	703	0.066
iso-octane	C_8H_{18}	0.444	44.3	114	690	0.066
HRJ-Tallow	$C_{12.1}H_{26.3}$	0.460	44.1	172	758	0.0664
FT-Natural Gas	$C_{12.1}H_{26.3}$	0.460	44.2	168	755	0.0664
n-Dodecane	$C_{12}H_{26}$	0.462	44.1	170	750	0.0667
HRJ-Camelina	$C_{12}H_{25.9}$	0.463	44.3	170	751	0.066
Alcohol-based Jet	$C_{12.5}H_{27}$	0.463	43.1	178	761	0.0669
cyclo-Hexane	C_6H_{112}	0.5	43.3	84	770	0.0675
Jet-A	$C_{11.4}H_{22.1}$	0.551	42.9	159	820	0.0681
135-TMB	C_9H_{12}	0.750	42.5	120	864	0.073
Toluene	C_7H_8	0.875	42.5	92	867	0.0745

Table 2.3: Fuels with their corresponding chemical formula, C/H ratio, Lower Heating Value (LHV) [3], density, and stoichiometric fuel to air ratio [21]

that swell when aromatic compounds are present. These seals do not work properly if the aromatic content of jet fuels is low (or zero).

The chemical composition for the blended fuels are based on two-dimensional gas chromatography (GCxGC) performed by the AFRL [21]. The chromatograms of the synthetic fuels tested are shown in Figure 2.3. The plots show the concentration in terms of detector response on the ordinate axis and the time on the abscissa. Each peak is proportional to a component present in the sample. The concentration of each component is the area under the peak. The retention time is defined as the time interval between sample injection and the maximum of the peak. Higher retention times are associated with heavier molecules. A few spikes indicate that a few species dominate the composition, whereas many spikes indicate a large number of species are present.

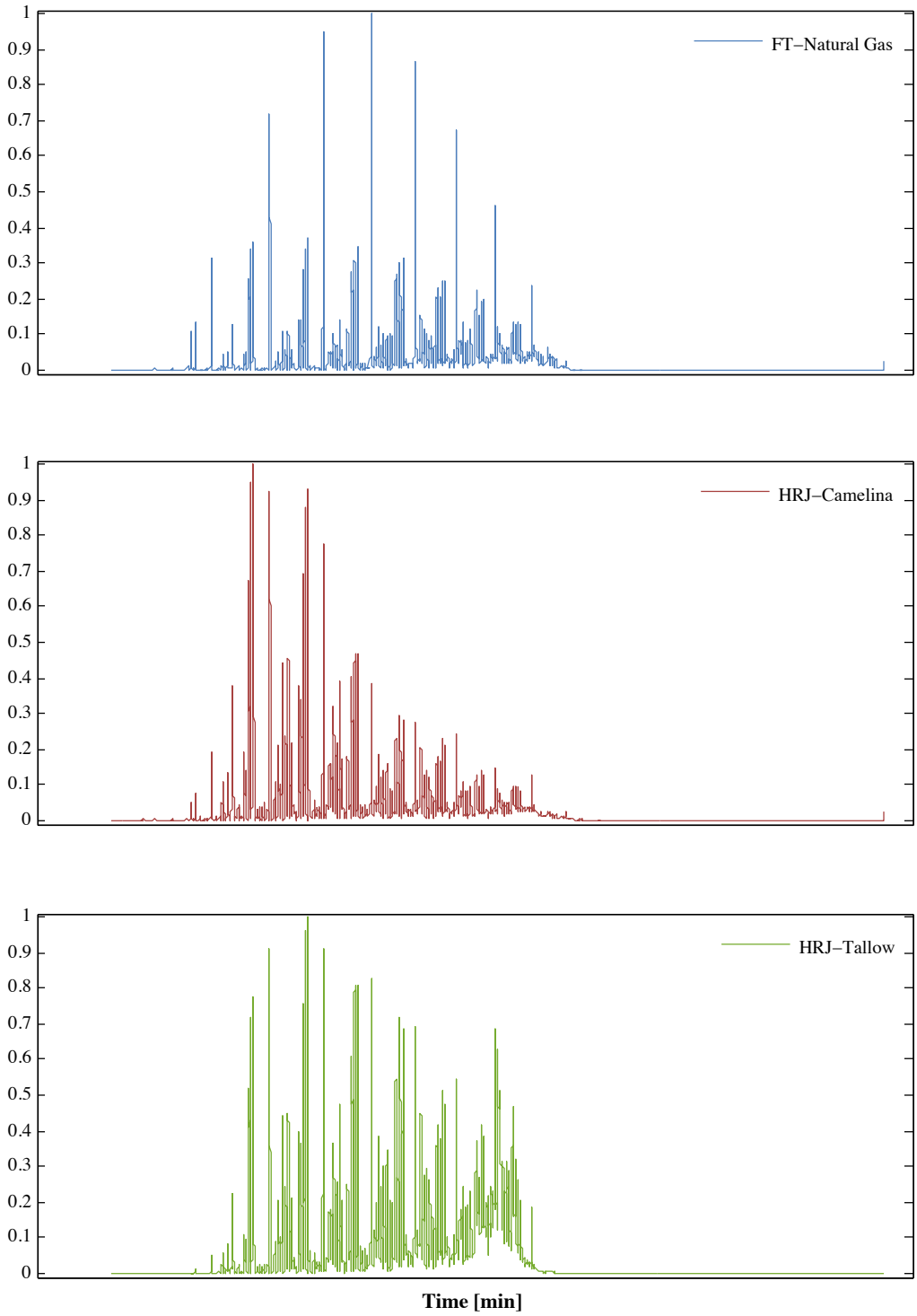

Figure 2.3: Normalized signal amplitude as a function of time for the alternative fuels provided by AFRL [21].

The chromatograms for each fuel are converted to species concentration with careful calibration of the device. Appendix A.2, also from the AFRL, lists the concentrations by carbon number for each molecular type: n-alkane, iso-alkanne, cyclo-alkane, and aromatic.

Figure 2.3 shows that major peaks are fairly wide apart across the time range for FT-natural gas. For HP-camelina the major peaks are grouped at the shorter times while HP-tallow peaks are fairly large in number and spread across the time range.

The fuel components can be grouped into the two broad categories of hydrocarbons present: aliphatic and aromatic. The aliphatic species are differentiated as normal alkanes, isomers of alkanes, and cyclo-alkanes. The aromatic species are differentiated as alkylbenzenes, indans/tetralins, and alkylnapthalenes. Figure 2.4 shows the composition of all fuels tested.

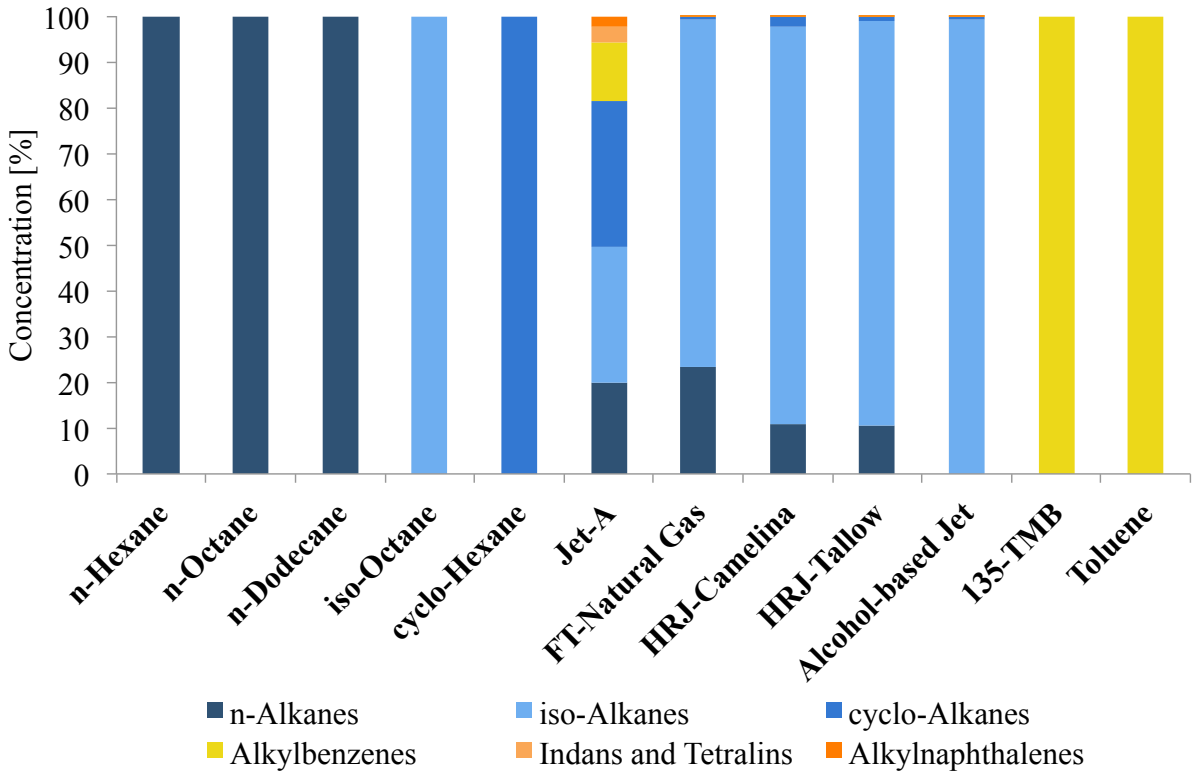

Figure 2.4: Composition of fuels (by weight %) used in experiments as obtained from AFRL [21].

Renewable jet fuels mainly contain iso-alkanes, with also about 10% n-alkanes in the HRJ-tallow and HRJ-camelina fuels. In FT-natural gas, the n-alkanes increase to about 20%. Alcohol-based jet fuel is mostly all iso-alkanes. The jet-A tested is about 30% iso-alkane, 30% cyclo-alkane, 20% n-alkane, and 20% aromatic.

2.3 Flow Control and Calibration

In this work, three different rotameters are used to measure the flow rate of 1^{st} stage, 2^{nd} air stage, and atomizor air. Each of these rotameters is calibrated using Precision Scientific Company's Wet Test Meter (WTM). The WTM is used to determine the flow rate of air at a given rotameter setting. Air is delivered to the rotameter from facility services compressed air after passing a filter. Throughout the calibration, pressure of air passing through the rotameter is maintained at the experimental value of 30 $psig$ for 1^{st} and 2^{nd} stage air and 48 $psig$ for atomizor air. Figure A.1 shows the rotameters used to regulate the three stages of air entering the SPP.

Detailed measurements and calibration curves for the three stages of air are given in Appendix A.3. Throughout the experiments, air flow rate is fixed while fuel flow rate is changed to vary temperature (and fuel-air equivalence ratio). Table 2.4 summarizes the mass flow rate of air for the three different stages. The total flow rate of air is fixed at 1.05 g/s when burning liquid fuels in the JSR.

	Pressure $[psig]$	Rotameter Setting	Mass Flow Rate $[g/s]$
1^{st} Stage Air	30	31	0.475
2^{nd} Stage Air	30	33	0.44
Atomizor Air	48	22	0.14

Table 2.4: Summary of rotameter settings and corresponding mass flow rate of air. These conditions are fixed throughout the experiments.

A different rotameter is used to measure the flow rate of liquid fuels. This rotameter is calibrated to determine the mass flow rate of each fuel for a given rotameter setting. Nitrogen is used to pressurize the fuel tank to 60 $psig$. After fuel passes through a $15\mu m$ filter, it enters the rotameter. Calibration is performed by measuring the volume of liquid fuel exiting the rotameter over a measured period of time. Detailed measurement and calibration curves of liquid fuels are presented in Appendix A.3. Liquid fuel flow rate is varied roughly from 0.045 to 0.06 g/s in experiments. Figure A.2 shows the liquid fuel handling system.

A few experiments are performed with methane. This gaseous fuel is injected in the SPP from the top section as shown in Figure 2.2 (hydrogen and propane are also injected from this port, but calibration is not performed since these fuels are only used for lighting-off and warming up the reactor). Calibration for methane flow rate is performed using the same WTM used to for air flow rate calibration. Detailed measurement and calibration curves of methane is presented in Appendix A.3.

The fuel-air equivalence ratio is found both using the flow meter measurements and gas analyzer measurements. The method used for the former is shown in Equation 2.2.

$$\phi_{flowmeter} = \frac{\dot{m}_{fuel}/\dot{m}_{air} \mid measured}{\dot{m}_{fuel}/\dot{m}_{air} \mid stoich} \tag{2.2}$$

The latter method uses the measured concentrations of CO, CO_2, and O_2 to calculate ϕ. The chemical equation for complete combustion of each fuel can be written as Equation 2.3, where x,y, and z subscripts correspond to the number of atoms of carbon, hydrogen, and oxygen in the fuel respectively.

$$\begin{aligned} \phi\ C_xH_yO_z + (x + y/4 - z/2)\ (O_2 + 3.773N_2) \Longrightarrow (x)\phi CO_2 + (y/2)\phi H_2O \\ +(x + y/4 - z/2)(1 - \phi)O_2 + 3.773(x + y/4 - z/2)N_2 \end{aligned} \tag{2.3}$$

The fuel-air equivalence ratio is calculated by first finding the CO_2 and O_2 measured if

combustion was complete. This is done by correcting for the amount of CO produced as showing in Equation 2.4. Then, the ratio $(\frac{O_2}{CO_2})_{complete\ combustion}$ along with Equation 2.3 are used to find the fuel-air equivalence ratio as presented in Equation 2.5.

$$(\frac{O_2}{CO_2})_{complete\ combustion} = \frac{(O_2)_{measured} - \frac{1}{2}\ (CO)_{measured}}{(CO_2)_{measured} + (CO)_{measured}} \tag{2.4}$$

$$\phi_{gas\ analyzer} = \frac{(x + y/4 - z/2)}{(x + y/4 - z/2) + x(O_2/CO_2)_{complete\ combustion}} \tag{2.5}$$

Both values of fuel-air equivalence ratio obtained for each test are presented in Appendix B.

2.4 Fuel Vaporization

Liquid fuel is atomized using a Nukiyama-Tanasawa type plane-jet airblast atomizer designed originally by Lee [47] and further modified a few years later by Lee [45]. The Sauter mean diameter (SMD) of the particles is approximately 10 to 20 μm according to Lee [45]. It was determined that the residence time required to fully vaporize the fuels with a SMD of 50 μm or less is about 10 ms or less [45].

The atomized fuel along with atomizer air enter the 1^{st} stage of the SPP. At this stage air enters at the temperature of about 320°C which has a residence time of approximately 9 ms. The second stage air enters downstream at about 320°C with an approximate residence time of 8 ms. Finally, the fluid enters a mixing tube with a residence time of approximately 5 ms. The summation of all residence times are larger than the required 10 ms to vaporize the fuels. The premixed-prevaporized fuel enters the JSR at approximately 330 °C (this value is higher than 320°C because of the back-heat of the JSR).

Figure 2.5 shows the boiling point distribution for all synthetic fuels and jet-A. The final

boiling point of all fuels lie below 280 °C. Given the temperature of fluid measured before entering the JSR is about 330 °C, it is believed that all fuels are fully vaporized before entering the JSR. The boiling curve of HRJ-camelina is lower than HRJ-tallow and FT-natural gas, consistent with the chromatograms shown above.

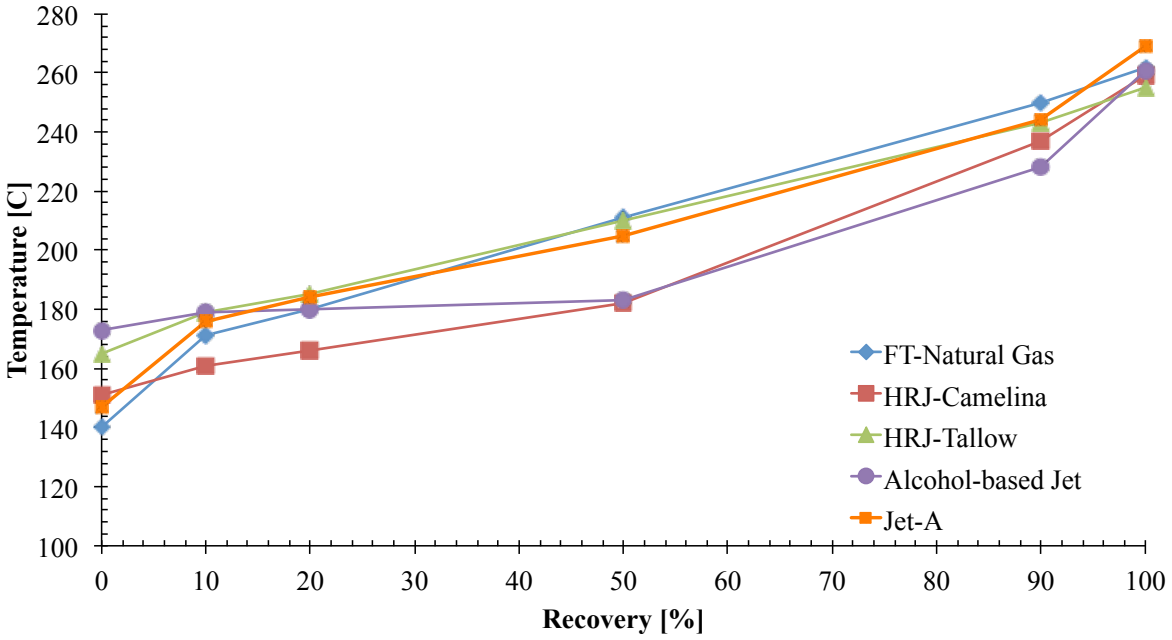

Figure 2.5: Boiling point distribution for the synthetic fuels tested [21], [14], and [15].

2.5 Experimental Results

Figure 2.6 shows the NO_x measurements at the recirculation zone temperature of 1800 K. These values are corrected to 15% dry O_2 using Equation 2.6. These data do not show much variation among the non-aromatic pure fuels, the alternative jet fuels, and jet-A. The main difference in NO_x is observed between aliphatic and aromatic fuels, with aromatics producing about 30% more NO_x than the aliphatic fuels.

$$NO_{x_{corrected\ to\ 15\%O_2}} = NO_{x_{measured,dry}} \frac{(20.95 - 15)}{(20.95 - O_{2_{measured,dry}})} \tag{2.6}$$

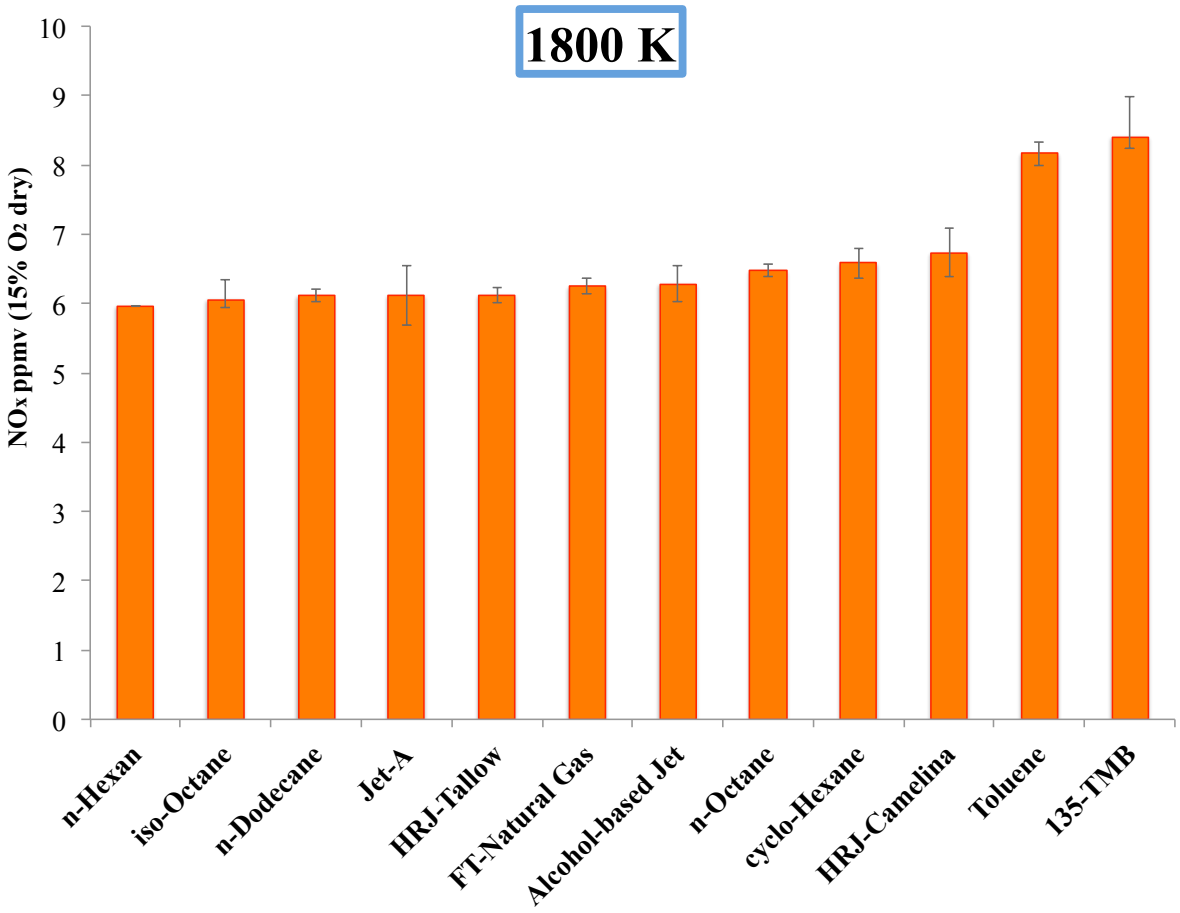

Figure 2.6: NOx measurements corrected to 15% dry O_2 for all fuels studied at 1800 K

The experiments are also performed at two other temperatures. Figure 2.7 shows the NO_x measurements (corrected to 15% dry O_2) at three different temperatures. The JSR air flow rate is fixed throughout the experiments. Fuel flow rate is increased to reach the (corrected) temperatures of 1700K, 1800K and 1900K in the recirculation zone. At least two experiments are performed on different days for each fuel to assess the variability of NO_x

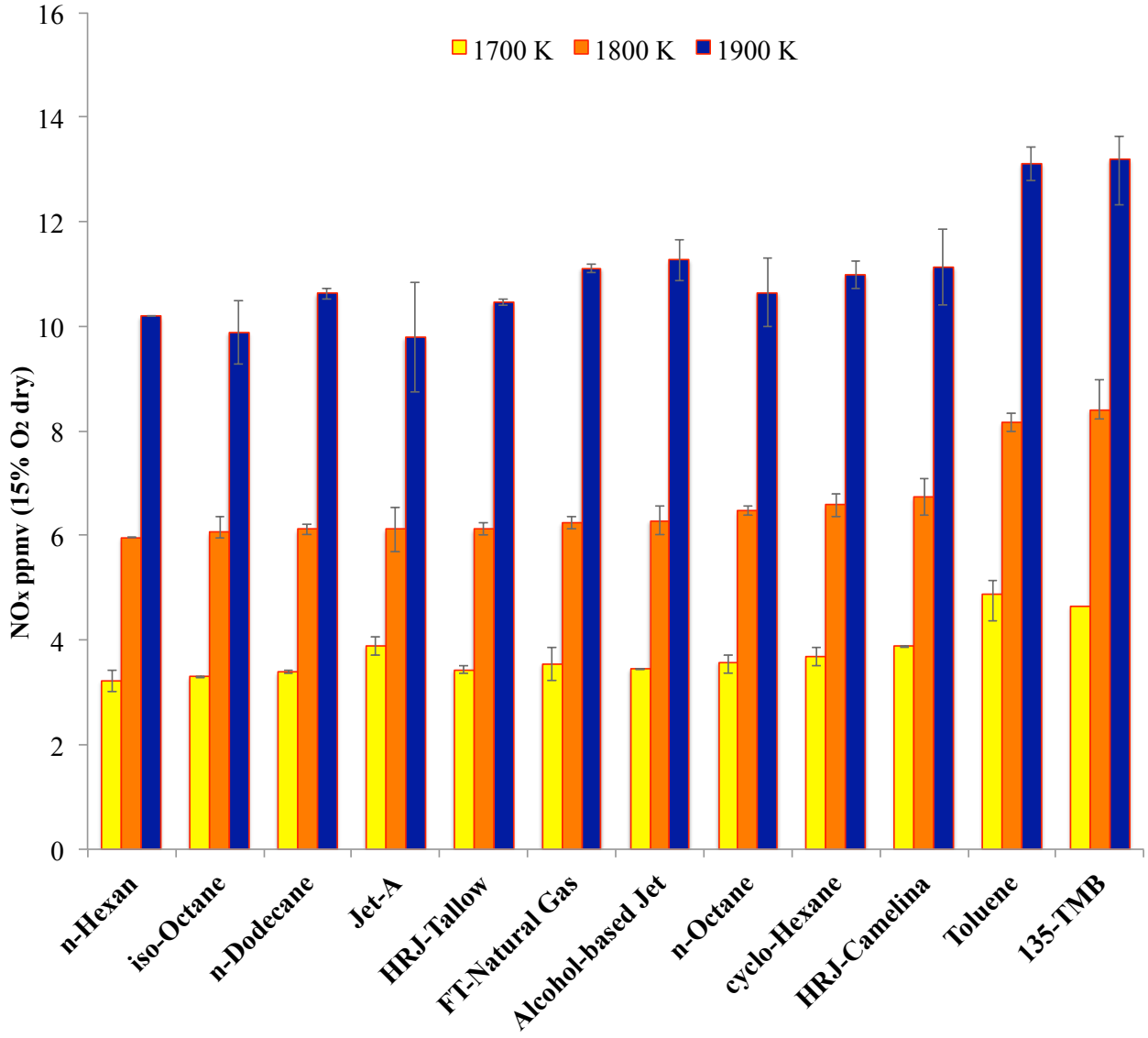

Figure 2.7: NOx measurements corrected to 15% dry O_2 for all fuels studied at 1700 K, 1800 K, and 1900 K.

measurements (except for n-hexane that was tested only once). The error bars shown in Figure 2.7 indicate this variation. Jet-A exhibits the greatest variability.

Figure 2.7 also shows that NO_x increases for all fuels as temperature is increased from 1700 K to 1900 K. Among all fuels, the pure aromatic fuels emit the greatest NO_x, without much variation in NO_x between the two aromatics tested. This result is consistent with the findings of Lee et al. [48] and Vijlee [83] for the same JSR as used for the current experiments. Among the fuels remaining (when the two pure aromatics are removed), the variation in NO_x across the fuel range is about 15% (relative) for 1800 and 1900 K. Previous work by Corporan et al. [13, 14] and Klingshirn et al. [37] also found little difference in NO_x emissions from a gas turbine engine running a variety of traditional and alternative jet fuel blends.

In Figure 2.8, the data for 1800K are compared to Lee's [48], taken at 1790K, for a range of n-alkanes, naphthas, diesel fuels (with fuel-NO_x subtracted), and aromatics. Lee's data show an increase in NO_x for the aliphatic and blended fuels from C/H ratio of 0.25 (methane) to about 0.6, followed by a leveling off for the two aromatics tested (benzene and toluene). Fuels tested in this work show a similar trend to that of Lee.

Fuels tested in the current work, except for methane and the aromatics, have a narrower range of C/H than the fuels examined by Lee. Most of the fuels used in this study are in the cluster from about 0.43 to 0.46 C/H ratio. Thus, it is difficult to discern a C/H dependency for these fuels. Only when methane and the aromatics are added is the trend with C/H ratio noted.

Figure 2.8 shows somewhat lower amounts of NO_x for the current study compared to Lee's data. This is thought to be caused by the smaller and faster reactor feed jet used in this set of experiments compared to Lee's. The faster and smaller jet should lead to improved mixing inside the reactor cavity.

Figure 2.9 shows all of the NO_x data points for all of the current experiments. The dashed line fits are assumed based on the trends of NO_x versus C/H seen in Figure 2.8. Measurements at all three temperatures follow the same trend in NO_x.

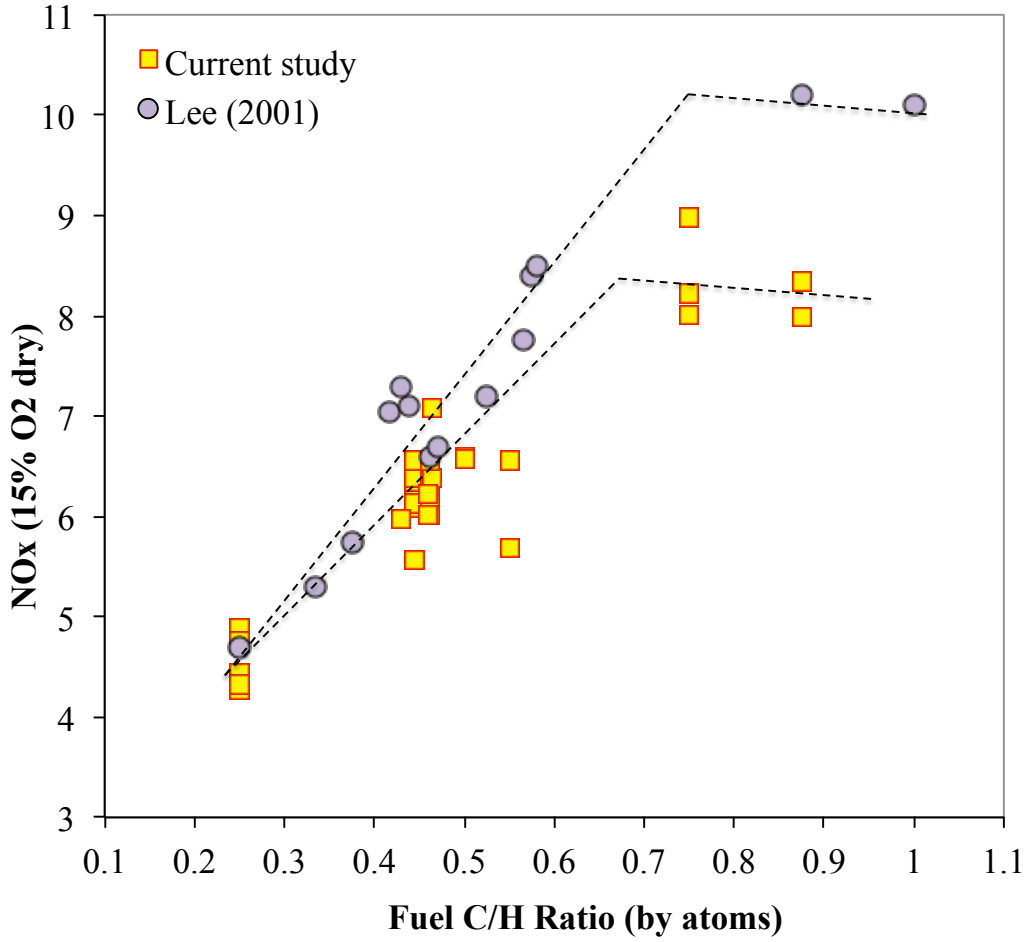

Figure 2.8: NO_x measurements of this study (at 1800K) compared to Lee's data (at 1790K) plotted against C/H ratio.

Figure 2.9 shows, for each temperature, the cluster of data for C/H ratio of 0.43 to 0.46. This cluster includes the pure, non-aromatic fuels and the blended alternative fuels. The cluster is located between the methane and pure aromatics NO_x levels. Each cluster shows a scatter in the NO_x data of +/- 15% (relative). The pure aromatic fuels give the greatest NO_x, without much variation in NO_x between the two aromatics tested. The aromatics tested do not shown an increase in NO_x with increasing C/H ratio. For each temperature, the mean of the aromatic NO_x data is about 30% (relative) greater than the mean of the cluster.

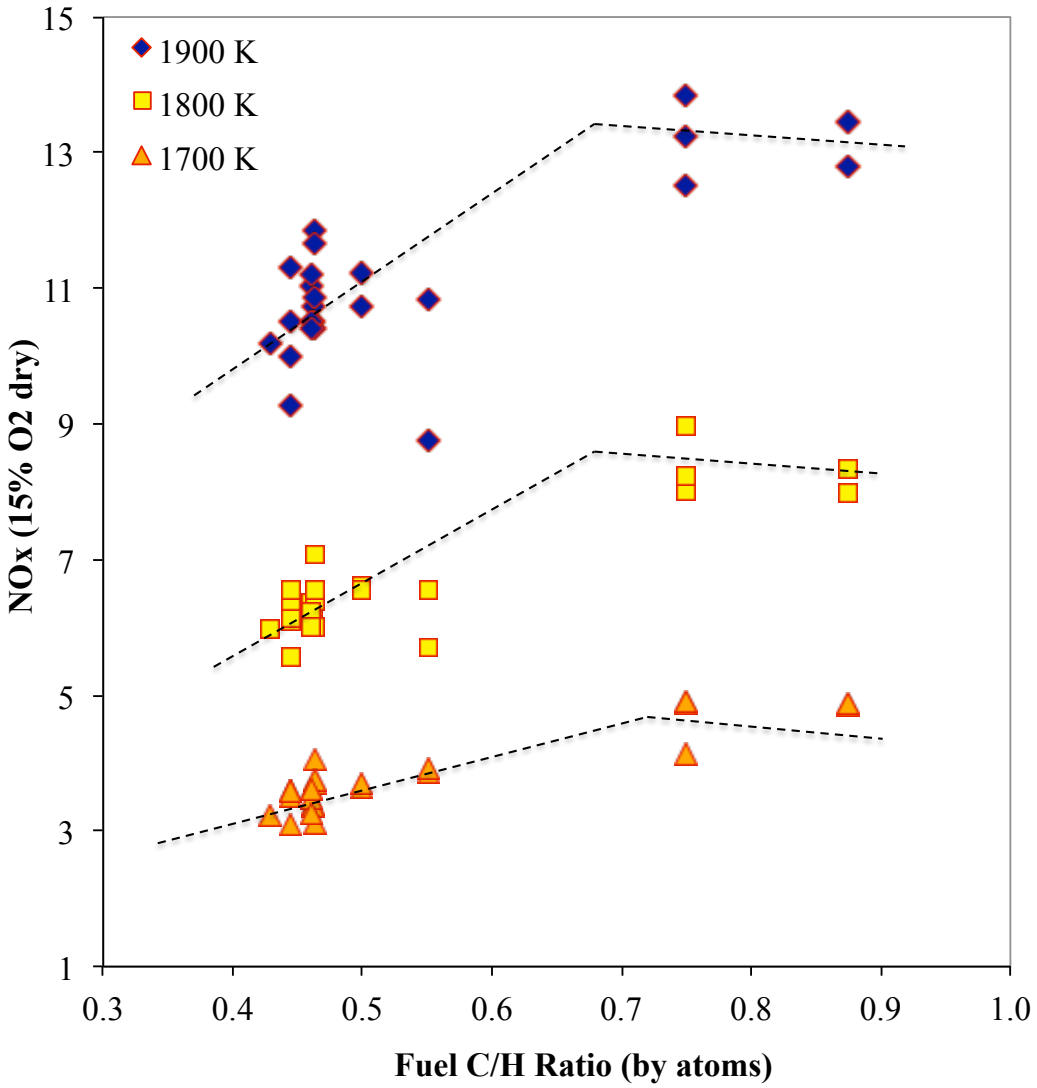

Figure 2.9: NO_x measurements corrected to 15% O_2 versus C/H ratio for recirculation zone temperatures of 1700 K, 1800 K, and 1900 K.

A closer look at the alternative jet fuels shows a small increase in NO_x in the following order for all temperatures: HRJ-tallow < FT-natural gas < alcohol-based jet< HRJ-camelina. This trend is similar to the findings of Vijlee [83] (as discussed in Chapter 1). Figure 2.10 shows a comparison between experimental data of this work and Vijlee [83] at 1900 K. It also shows that for similar fuels, NO_x levels in the current measurements are somewhat greater than in Vijlee [83]. This occurs because of the slightly larger reactor residence time in this study.

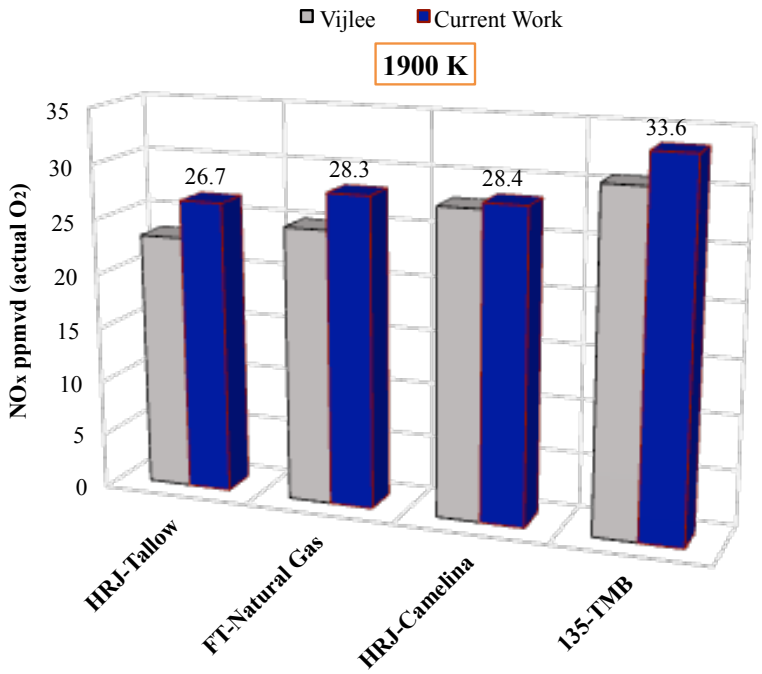

Figure 2.10: NO_x measurements of this study compared to Vijlee's data at 1900K.

The small variation in NO_x among these fuels is not clear. HRJ-tallow, FT-natural gas, alcohol-based jet, and HRJ-camelina have a very close range of C/H ratio, 0.460 to 0.463. At the two ends of Figure 2.10, HRJ-Tallow and HRJ-camelina produce the lowest and highest NO_x, respectively. By weight %, based on the AFRL data, HRJ -tallow is 88%

iso-alkane, 11% n-alkane, 1% cyclo-alkane, and 0.1% aromatic, HRJ-camelina is very similar: 87% iso-alkane, 11% n-alkane, 2% cyclo-alkane, and 0.2% aromatic. The measured NO_x data analyzed by Vijlee showed that aromatic content can increase NO_x. However, the aromatic content of these fuels is so small that this is not believed to explain the difference in NO_x measured. Cyclo-alkane content may increase NO_x, though the cyclo-alkane content of these fuels is only 1-2%.

Chromatograms in Figure 2.3 show differences between the two hydro-processed fuels. HRJ-tallow shows concentrated peaks at high retention times. This suggests that the isomers contained in these two fuels are quite different and this could be causing the small difference in measured NO_x. However, lacking further analysis of the chromatograms, it is difficult to say more. What is clear from the current experiments is that the alternative fuels show minor differences in NO_x amongst themselves and compared to jet-A.

The most significant difference in NO_x is observed between aliphatic and aromatics fuels. The reasons behind this difference cannot be answered using experimental methods without having access to laser diagnostics. Thus, in this work, in order to explain the NO_x trends observed experimentally, chemical kinetic modeling is performed in Chapter 4. Because of the experimental differences in NO_x for the aliphatic and aromatic fuels, the chemical kinetic modeling is focused on model compounds of iso-alkane, normal-alkane, and aromatic type. The alternative jet fuels are mainly composed of iso-alkanes, with lesser amounts of normal-alkanes, and for use in aircraft engines, will need to be blended with aromatics. Thus, understanding lean-premixed NO_x formation for model compounds of these three types is quite important. Figure 2.11 summarizes these fuels and their corresponding NO_x (actual O_2, not corrected to 15% O_2).

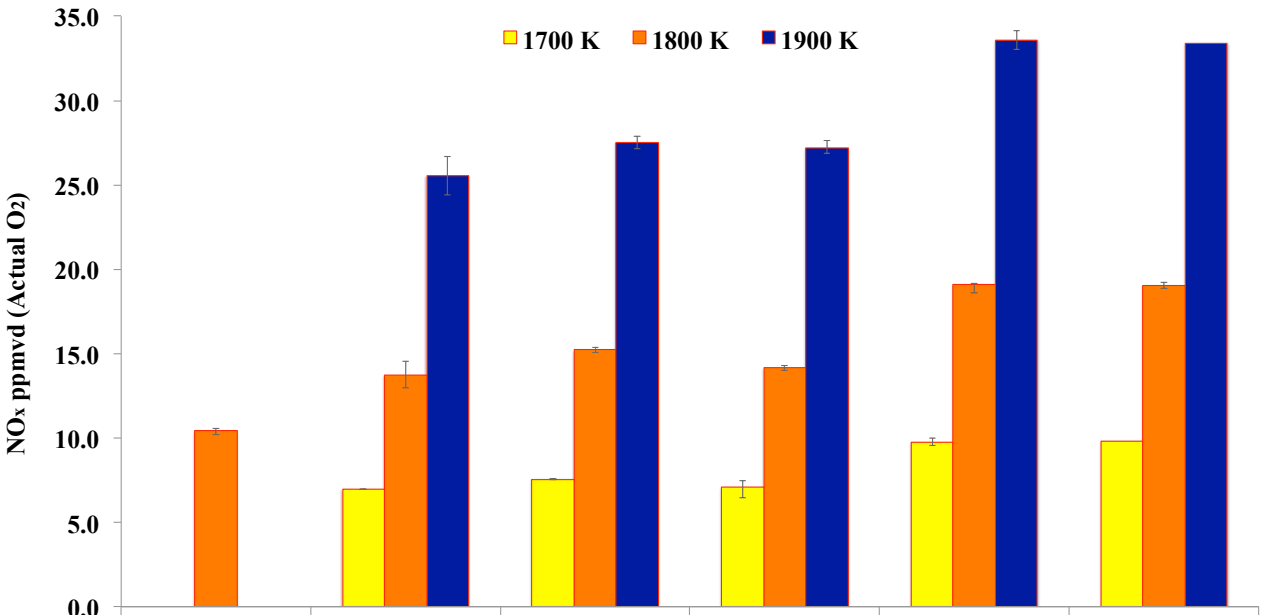

	Methane	iso-Octane	n-Octane	n-Dodecane	135-TMB	Toluene
1700 K		7.0	7.6	7.1	9.8	9.8
1800 K	10.4	13.8	15.2	14.2	19.1	19.1
1900 K		25.5	27.5	27.2	33.6	33.4

Figure 2.11: Pure fuels and their corresponding NO_x measurements that are used in chemical kinetic modeling in Chapter 4.

2.6 Summary of findings

This chapter reports on the testing of a wide range of fuels in the JSR. The purpose is to study the combustion of alternative jet fuels in comparison to a petroleum-based jet fuel and pure aliphatic and single-ring aromatic fuels. Four alternative jet fuels and one traditional commercial jet fuel are burned. The focus of this study is on lean-flame NO_x formation. Lean blowout (LBO) results are shown in Appendix B.2. The major findings are the following:

1. The combustion of alternative and traditional commercial jet fuels show relatively minor differences in NO_x. The trend observed at three different temperatures of the recirculation zone shows: HRJ-tallow $<$ FT-natural gas $<$ alcohol-based jet$<$ HRJ-camelina.

2. The largest difference in NO_x is between aliphatic and aromatic fuels. Aromatics produce about 30% more NO_x than aliphatic fuels. Further investigation for this difference is going to be conducted by chemical kinetic modeling of model compounds in Chapter 4.

Chapter 3

COMPUTATIONAL FLUID DYNAMICS

In this chapter, CFD is used to model the fluid structure and chemistry inside the JSR. The results found using CFD simulations of simple fuels aid in generating a Chemical Reactor Network (CRN) model that can be used for prediction of NO_x emissions from combustion of liquid fuels. Another goal of the CFD work is to explore the temperature and species fluctuations in the recirculation zone of the JSR as well as determining how NO_x species are formed/destroyed inside the reactor. Three major cases are studied here as shown below. All cases are fuel lean for a mean temperature of 1800 K in the recirculation zone.

1. Combustion of H_2
2. Combustion of H_2 with NO_x chemistry included
3. Combustion of CH_4

RANS turbulence modeling is initially used for each case to develop a solution that is later utilized to initialize the Large Eddy Simulation (LES) modeling of the flow. Modeling chemistry correctly is essential for this study, therefore, the Complex Chemistry model with the Laminar Flame Concept (LFC) is utilized [77]. This model solves transport equations for species and calculates reaction rates by modified Arrhenius kinetic expressions.

3.1 CFD Model Development

Three dimensional CFD simulations for combustion of gaseous fuels, hydrogen and methane, are carried out with the Simcenter STARCCM+ 12.02 software package [77]. In order to save computational time, only the fluid portion of the reactor is modeled (and not the solid

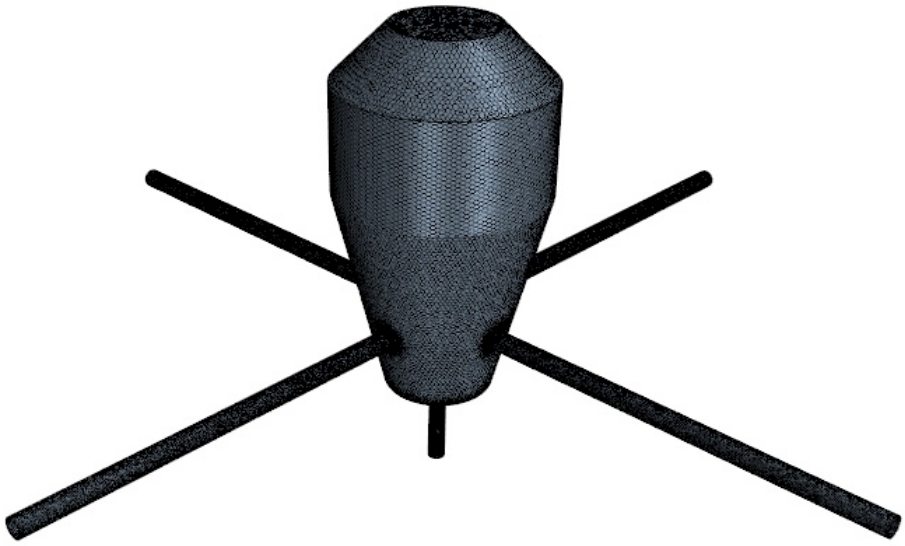

Figure 3.1: Geometry of computational domain.

portion). A diagram of the computational domain is provided in Figure 3.1. This domain contains approximately 9 million cells. The polyhedral Mesher is used for generating an automated mesh in STAR-CCM+. The base size for the fine mesh is 0.1 mm and 2 prism layers are applied with the near wall total thickness of 0.15 mm.

3.1.1 Solver Settings and Boundary Conditions

Pre-mixed, pre-heated fuel and air enter the reactor at a choked condition. The computational domain is discretized using the 2^{nd} order segregated scheme for flow, species, and energy. In LES, flow is discretized using Bounded Central Differencing (BCD) with an upwind blending factor of 0.05. A value of 0 for upwind blending factor implies pure central differencing. A value of 1 implies pure upwind differencing. The value of 0.05 for the blending factor is chosen to balance accuracy and stability.

Time is discretized using a 2^{nd} order implicit scheme for LES simulation. To ensure temporal and spatial resolution for well-resolved LES results, it is important to achieve a Courant-Friedrichs-Lewy (CFL) condition close to 1. Therefore, the time step is found by setting Equation 3.1 to 1 [82]. Based on the mesh size and velocity of the jet, the time step used for the LES solver is set to $1E-7\ s$ to ensure this condition is met.

$$CFL = \frac{u \triangle t}{\triangle x} \tag{3.1}$$

The species inside the reactor are modeled as compressible ideal gases. Material properties for the domain are calculated using the methods listed in Table 3.1.

Property	Method
Dynamic Viscosity	Mathur-Saxena Averaging [55]
Thermal Conductivity	Mathur-Saxena Averaging [55]
Specific Heat	Mass-Weighted Averaging
Molecular Diffusivity	Kinetic Theory [67]
Turbulent Prandtl Number	Constant at 0.7
Turbulent Schmidt Number	Constant at 0.7

Table 3.1: Methods used to calculate material properties of species

Flow entering the reactor is choked at the nozzle. The inlet stagnation pressure and temperature are 21 $PSIG$ and 550 K, respectively. The outlet static pressure and temperature are set to 0 $PSIG$ and 1800 K. Mass fractions of species at the inlet correspond to the fuel-air equivalence ratio of 0.6 and 0.7 for hydrogen and methane, respectively. Turbulent intensity (I) and turbulence length scales (l) are estimated for the inlet boundary condition using the following equations [2]. In this equation, D is the nozzle diameter and Re_D is the

Reynolds number based on the diameter of the nozzle. In the case of the JSR, Re_D is about 5E5, the turbulent intensity is 5%, and the turbulence length scale is 0.14 mm.

$$I = \frac{u'}{u_{avg}} = 0.16(Re_D)^{-1/8} \tag{3.2}$$

$$l = 0.07D \tag{3.3}$$

Since the CFD simulations in this work represent the experiments ran by Fackler and Karalus, heat transfer at the walls is modeled as a heat flux boundary condition, with values obtained using previous CFD simulations of the JSR by Fackler [24] and Karalus [34]. Fackler and Karalus modeled the JSR including the fluid and solid zones to simulate heat transfer. Their modeling accounted for convection on both the inner and outer surfaces of the JSR, conduction throughout the solid domain, and radiation on both the inner and outer surface of the JSR. Heat flux values at the walls from [24] and [34] are mapped on the walls of JSR in this study.

Heat flux is greatest where the jet impinges at the top of the JSR and reduces linearly to the bottom of the JSR. If the values of heat flux are mapped directly on the walls, the discontinuity at the corners creates cold spots on the walls of the JSR and causes instabilities. In order to address this issue, the heat flux profile from the Fackler and Karalus CFD simulations is mapped on the walls as a continuous field function which depends on the vertical position. These functions are given in Table 3.2 for hydrogen and methane where z is the vertical dimension in meters and q'' is in W/m^2. The resulting amount of heat transfer rate from the walls of the JSR is about 750 W for hydrogen and 600 W for methane. The difference between the heat loss values is due to the difference between lower heating value and molecular weight of the two fuels.

Fuel	Derived Heat Flux Equation for Wall Boundary Condition
Hydrogen	$q'' = -60000 - 5100000z$
Methane	$q'' = -60000 - 3500000z$

Table 3.2: Heat Flux equations used as wall boundary conditions for hydrogen and methane.

3.1.2 Chemistry Modeling

Reactor chemistry inside the reactor is modeled by solving the conservation equations describing convection, diffusion, and reaction sources for each species. This is referred to as the Complex Chemistry model in STAR-CCM+. This model is suitable for simulations that require detailed chemistry. Since the goal of this work is to accurately solve for concentrations of species inside the JSR, this model is chosen over flamelet models. The flamelet models lack accuracy when modeling emissions, particularly NO_x. In the Complex Chemistry model, a species transport equation is solved for each species as shown in Equation 3.4.

$$\frac{\partial}{\partial t}(\rho Y_i) + \frac{\partial}{\partial x_j}(\rho u_j Y_i + F_{k,j}) = \omega_i \tag{3.4}$$

In this equation, Y_i is the mass fraction of species i, ρ is the density, $F_{k,j}$ is the diffusion flux component, and ω_i is the rate of production of specie i. To account for the turbulence effects on combustion, the Laminar Flame Concept (LFC) is included (also known as finite-rate kinetics model) [77]. In this model, finite-rate kinetics are incorporated by computing the chemical source terms using the modified Arrhenius expressions, without attempting to account explicitly for the effects of turbulent fluctuations on the source-term calculations. However, However, turbulent chemistry interactions are included implicitly through the increased diffusion provided by the turbulence model. This increased diffusivity results in a flame thickness that is larger than the laminar flame thickness, and a turbulent flame propagation speed that is faster than the laminar flame speed [77].

The source term in the species transport equation is calculated for the i^{th} species using Equation 3.5. In this equation, Y_i^* is the mass fraction at the end of time integration, and τ is the time step in case of an unsteady flow or the residence time of the cell, if flow is steady.

$$\omega_i = \rho(\frac{Y_i^* - Y_i}{\tau}) \tag{3.5}$$

Y_i^* is calculated from Equation 3.6. In this equation, r_k is the reaction rate obtained from the modified Arrhenius expressions and $\boldsymbol{Y}$ is the mass fraction vector. The CVODE solver developed by Pope [75] is used to integrate the chemical source terms in the species transport equations.

$$Y_i^* = Y_i + \int_0^\tau r_k(\boldsymbol{Y}, T, p)dt \tag{3.6}$$

The modified Arrhenius rate constants are provided in chemical kinetic mechanisms for the fuel of interest. In this work, the hydrogen mechanism of Li [49] with 9 species and 19 reactions is utilized. Methane is modeled using a skeletal mechanism by Karalus [35] without NO_x chemistry. This mechanism is based on GRI 3.0 and includes 22 species and 122 reactions. A reduced set of NO_x reactions are derived from the Klippenstein et al. [38] H-N-O NO_x mechanism and are added to Li et al.'s hydrogen mechanism. The reduction procedure and reactions are provided in Section 3.3.2. This reduced NO_x mechanism adds 5 species and 14 reactions to Li et al.'s mechanism.

3.1.3 Turbulence Modeling

Turbulence is initially modeled with steady-state Reynolds-Averaged Navier Stokes (RANS) equations and realizable $k - \epsilon$ equations as the turbulent closure model [76]. The converged solution of steady state RANS is used as an initial solution for the Large Eddy Simulation

(LES) model. A summary of turbulence models is provided in Table 3.3.

Turbulence Models	Closure Models
RANS	Realizable $k-\epsilon$
LES	WALE subgrid scale

Table 3.3: Turbulence models used in this work with their corresponding closure models.

In LES, the larger three dimensional unsteady turbulent motions are directly solved, whereas the effects of smaller scale motions are modeled. In computational expense, LES lies between RANS and Direct Numerical Simulation (DNS). The equations that are solved for LES are obtained by filtering rather than averaging the governing equations of the RANS method. Velocity and density are decomposed to a filtered (or resolved) component and a residual (or subgrid-scale, SGS). After using the Navier-Stokes equations to derive the equations for the evolution of the filtered velocity and density, the residual stress tensor or SGS stress tensor arises, which requires modeling to obtain closure [69]. In these simulations, Wall-Adapting Local-Eddy Viscosity, WALE, is used to algebraically model the subgrid scale, SGS [65]. This is preferred over the Smagorinsky SGS model because of its lower computational cost and equivalent accuracy. Similar to Smagorinsky subsgrid scale model, WALE model suffers from the limitation that the model coefficient, C_w in Equation 1.8, is not universal. Validation studies by Simcenter STAR-CCM+ has shown that the WALE model is less sensitive to this coefficient compared to Smagorinsky model. Another advantage of the WALE model is that it does not require any form of near-wall damping as it automatically gives accurate scaling at walls [77].

3.2 CFD Mesh Resolution

Due to the importance of mesh resolution on LES results, mesh dependency of the simulation domain is studied using a cold flow solution. This effort uses RANS modeling due to its low

computational cost. This is done by creating a uniform mesh of different base sizes using the polyhedral and prism layer mesher in STAR-CCM+ 12.02. There are three prism layers in the nozzle and two inside the JSR and drainholes. Mesh base size is varied from 3 mm down to 0.5 mm to find a base size that produces results that are independent of the mesh size. Figure 3.2 shows the jet velocity as a function of axial position of the jet.

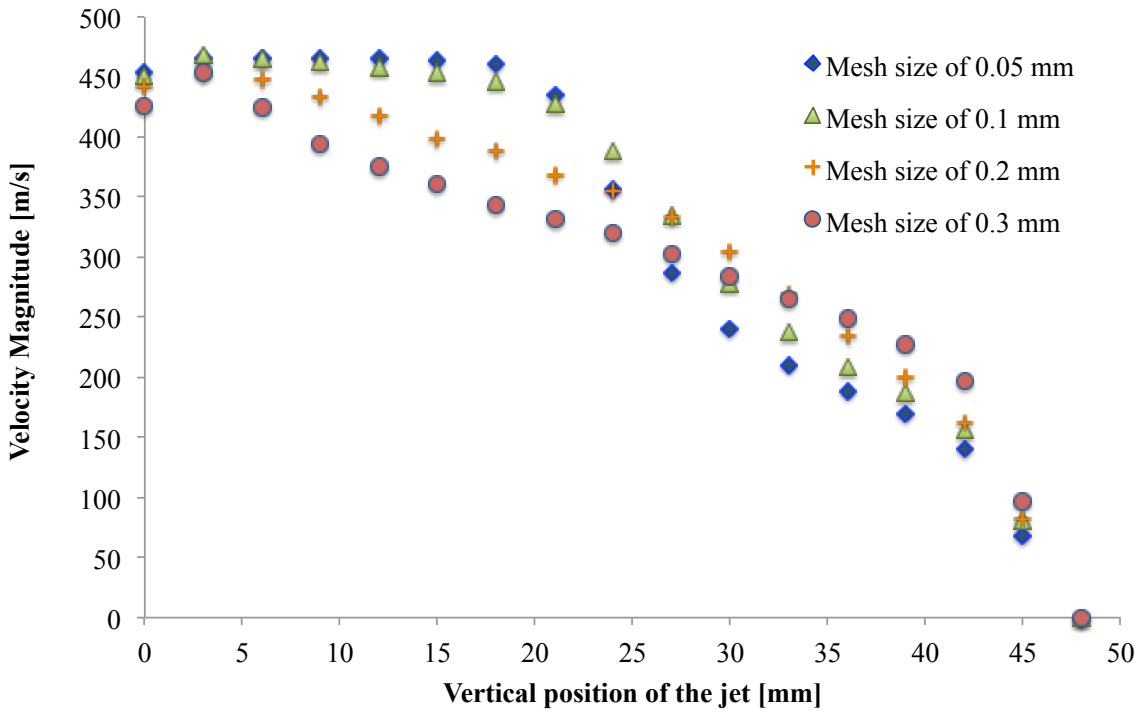

Figure 3.2: Velocity magnitude of the jet as a function of axial position of the jet for several mesh sizes.

Cases with mesh base size of 0.1 and 0.05 mm appear to predict the same jet core lengths. Mesh size of 0.1 mm gives an overall 9 million cells in the JSR whereas the 0.05 mm base size gives over 25 million cells. Since essentially the same results can be obtained with the more realistic number of mesh cells, the base size of 0.1 mm is chosen for this study. This mesh size shows good agreement with the temperature profile measured as shown in the following section.

This mesh size produces a well-resolved LES simulation. The solution history obtained from the LES simulation of H_2 with NO_x chemistry is used to calculate the ratio of the total turbulent kinetic energy to the subgrid scale turbulent kinetic energy. As mentioned in Section 1.2.4, a well resolved LES simulation contains only about 5% energy in the subgrid region. For this reason, the ratio of turbulent kinetic energy to subgrid turbulent kinetic energy, $\frac{k}{k_{sgs}}$ is aimed to be above 20 to ensure a well-resolved solution. In locations where $\frac{k}{k_{sys}}$ is less than 20, mesh should be refined to increase this ratio. For the current case, the majority of the cross-sectional area of the JSR has a value of $\frac{k}{k_{sgs}}$ greater than 20 as seen in a snap shot at 9.5 ms in Figure 3.3. This figure shows that LES simulations are well-resolved and sufficient to perform LES simulation of premixed combustion of hydrogen and methane.

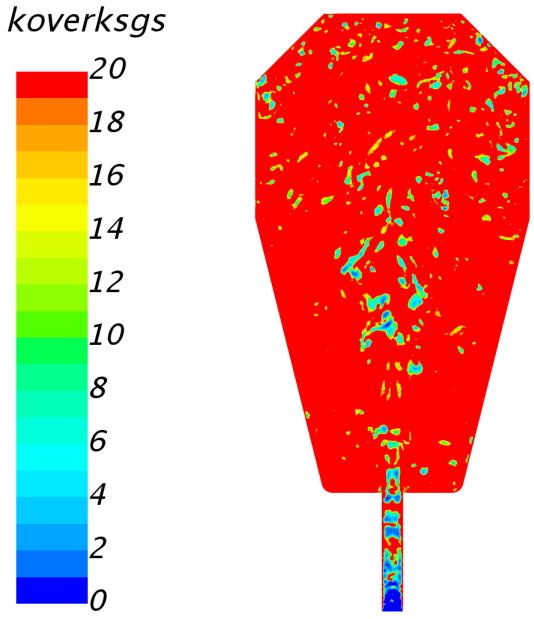

Figure 3.3: Snapshot of $\frac{k}{k_{sgs}}$ (koverksgs) for the LES solution of H_2 combustion with nitrogen chemistry.

3.3 CFD results

In this section, CFD results for three cases of H_2, H_2 with NO_x chemistry, and methane combustion are considered . All these simulations are run on the University of Washington super computing cluster, MOX-Hyak. This cluster utilizes 100Gbs Intel Omni-Path interconnects for low communication latency, and a high throughput. Each node consists of 28 cores and has a memory of 100 GB. For each of the simulations discussed in this chapter, 8 nodes are used.

3.3.1 H_2

The steady-state RANS solution for combustion of hydrogen is given in Figure 3.4. This figure shows the contour plots of temperature and species concentrations on a cross section of the JSR. Pre-mixed fuel and air enter the reactor at a fuel-air equivalence ratio of 0.6. This jet of premixed reactants entrains hot recirculation gases and ignites. The top half of the reactor attains a temperature of about 1800K, while the bottom half has a somewhat lower temperature due to lower momentum of the hot fluid into this region. The radical concentrations are mainly formed around the jet and their concentrations are highest around the jet. These radicals quickly react with other species and their concentrations drop as they reach the recirculation zone. O-atom and H-atom mole fractions are on the order of $\sim 10^{-4}$ in the recirculation zone.

A well converged solution of RANS is used to initialize the LES simulation. Figure 3.5 shows the snapshots of the temperature and important species concentrations on the cross section of the JSR. These snapshots are taken at a physical time of 9.5 ms. These figures show that pockets of low temperature fluid with high concentration of radicals shed from the top of the jet and are entrained by the hot recirculation gases.

The LES simulation is run for the physical time of 6 ms, about 2 times the residence time of fluid inside the reactor to allow the solution to develop. Then statistics are collected for 2.8 ms (the mean residence time of the reactor) for variables such as temperature. These

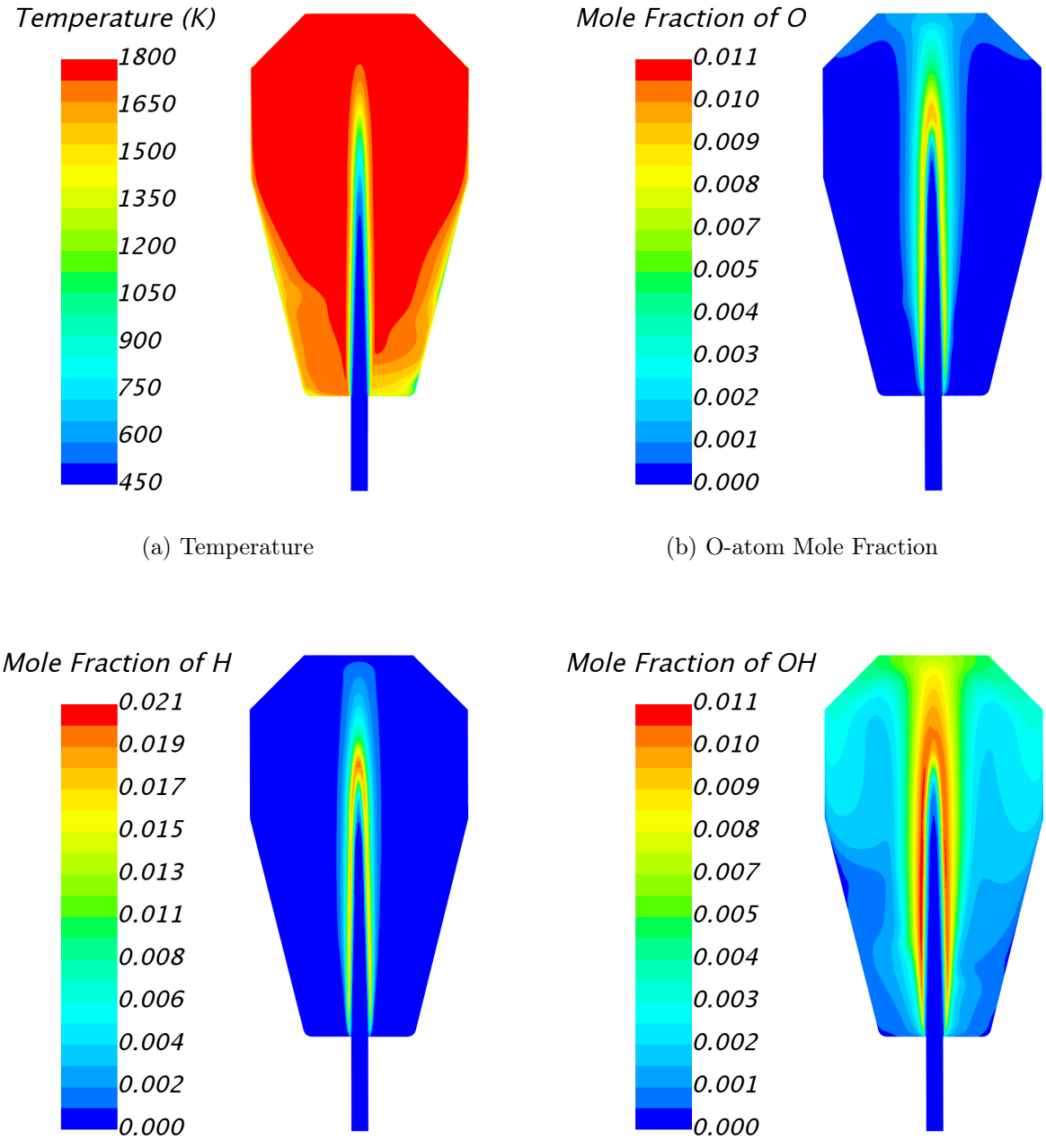

(a) Temperature

(b) O-atom Mole Fraction

(c) H-atom Mole Fraction

(d) OH-atom Mole Fraction

Figure 3.4: RANS solutions for combustion of hydrogen.

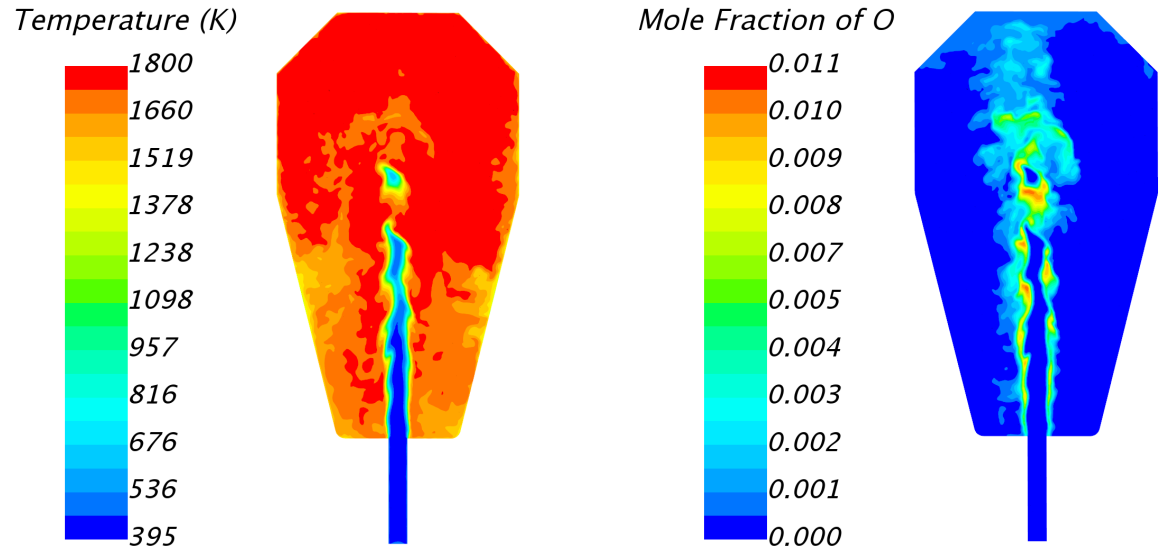

(a) Temperature

(b) O-atom Mole Fraction

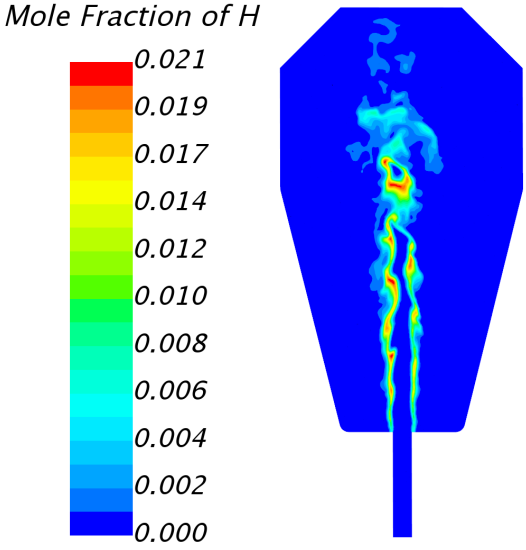

(c) H-atom Mole Fraction

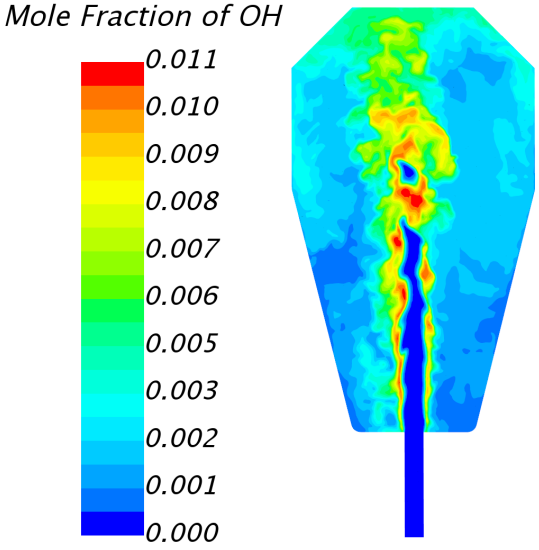

(d) OH-atom Mole Fraction

Figure 3.5: LES snapshots for combustion of hydrogen.

statistics are used to create mean profiles of temperature inside the reactor.

Among these variables, temperature is the only one that is experimentally measured. Figure 3.6 shows the mean temperature values plotted on a line from the center line to the wall at 2/3 height of the reactor. These values are compared to temperature measured at the same locations by Fackler [24] and the present RANS results. The temperature profile obtained experimentally suggests a flat profile for temperature. However, the RANS simulation shows lower temperatures near the centerline which suggests a longer jet than it is experimentally measured. LES displays a closer profile to experiments compared to RANS. LES simulations show that the mean temperature in the recirculation zone is about 1770 K, which is 30 degrees lower than the measured value.

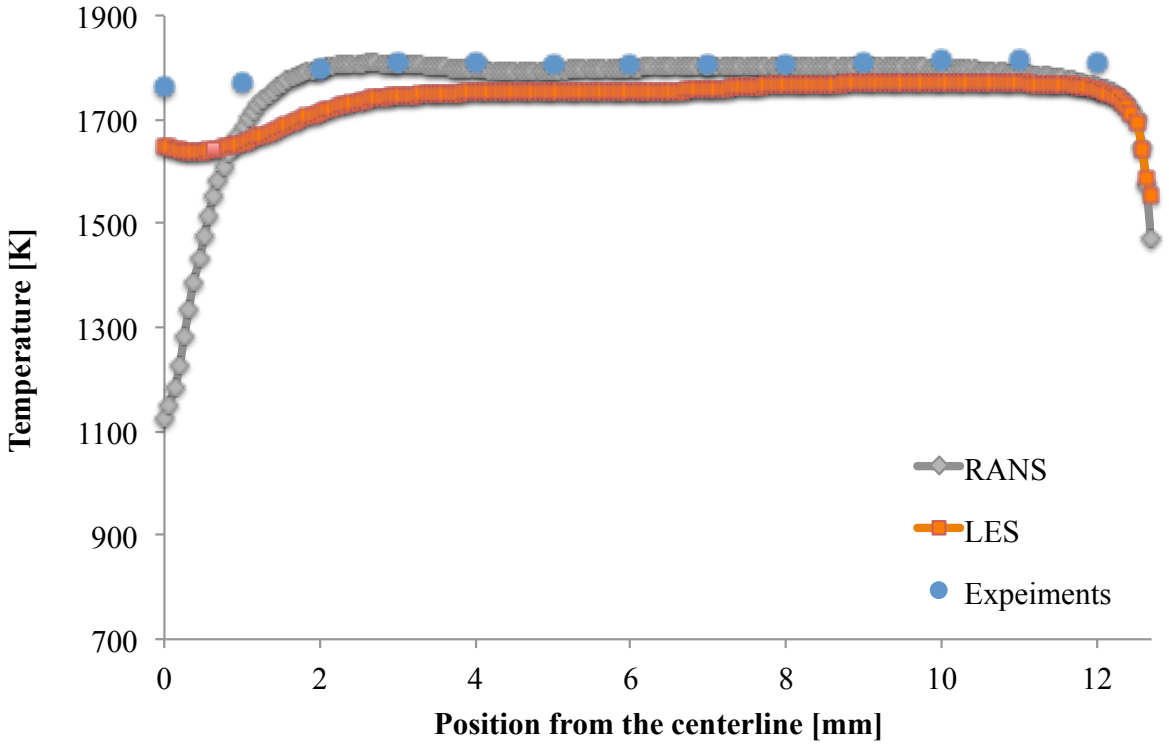

Figure 3.6: Comparison of temperature between RANS and LES simulations with experiments. These values correspond to temperature sampled at $2/3^{rd}$ height of the reactor going from centerline of the JSR to the wall.

3.3.2 H_2 with NO_x chemistry

The previous section discussed results for CFD simulation of H_2 combustion with no NO_x chemistry. In this section, NO_x chemistry is added to the Li et al. [49] hydrogen mechanism to model the emissions and the CFD simulations are repeated.

In order to save computational time, a reduced NO_x mechanism is derived from Klippenstein et al. [38]. The CRN model developed in Chapter 4 is used to eliminate reactions that are not important in NO_x production with the given boundary conditions.

CRN modeling shows that reactions involving NH_3, NH_2, and H_2NO (1-19 and 46-52 in Table 4.4) are not involved in NO_x formation/destruction for the lean H_2 combustion at 1800K – the case modeled. Reactions involving NO_2 are omitted, since their net effect on NO concentration in the JSR is negligible. Other reactions are eliminated one by one to find important reactions that are significant in NO_x formation/destruction. Table 3.4 shows the 14 reactions that are essential to NO_x formation for the CFD simulation of lean pre-mixed H_2 combustion.

Eq #	Reaction	A	n	$E_A[cal/mol]$
21	$NH + O \iff NO + H$	9.2E+13	0	0
26	$NH + NO \iff N_2O + H$	1.8E+14	-0.351	-244
30	$N + OH \iff NO + H$	3.8E+13	0.00	0
31	$N + O_2 \iff NO + O$	6.4E+9	1.00	6280
32	$N + NO \iff N_2 + O$	2.1E+13	0.00	0
33	$NNH \iff N_2 + H$	1.0E+9	0.00	0
34	$NNH + H \iff N_2 + H_2$	1.0E+14	0.00	0
35	$NNH + O \iff N_2O + H$	1.9E+14	-0.274	-22
37	$NNH + O \iff NH + NO$	5.2E+11	0.388	-409
39	$NNH + O_2 \iff N_2 + HO_2$	5.6E+14	-0.385	-13
59	$N_2O + (M) \iff N_2 + O + (M)$	1.3E+12	0.00	62,570
60	$N_2O + H \iff N_2 + OH$	6.4E+7	1.835	13,492

61	$N_2O + O \iff NO + NO$	9.2E+13	0.00	27,679
62	$N_2O + O \iff N_2 + O_2$	3.7E+12	0.00	15,936

Table 3.4: Reduced NO_x mechanism using Klippenstein [38] O-H-N species NO_x mechanism. Units in this table are cgs.

The original NO_x mechanism included 17 species and 64 reactions, however, after the reduction, only four extra species (NO, NNH, NH, N_2O) and 14 reactions are added to Li's H_2 mechanism. The NO_x values predicted by CRN using the original and reduced mechanisms are within 1% of each other. Thermochemical data for the additional species are added to the thermo-chemical data files of Li et al [38].

RANS solutions with NO_x chemistry are shown in Figures 3.7 and 3.8. The contour plots in Figure 3.7 are similar to Figure 3.4 in the previous section. Figure 3.8 shows the contour plots of NO_x species concentrations on the cross-section of the JSR. Peak concentrations of N_2O, NNH, and NH are found in the flame brush at the tip of the jet. Their concentrations decay rapidly as they mix with in the recirculation zone contents. NO concentration is highest in recirculation zone. The predicted species concentrations are given on a wet basis.

The snapshots for the LES solutions are shown in Figures 3.9 and 3.10. Figure 3.9 shows pockets of O-atom, H-atom, and OH radicals with high concentrations in the flame brush that shed along the jet. The temperature of the reactor is highest in the top section of the recirculation zone. Recycling fluid loses heat to the walls of the reactor. Plots of O-atom and H-atom with higher resolution in the recirculation zone is provided in Appendix C.

O-atom, H-atom, and OH radicals react with nitrogen molecules and form important NO_x species such as N_2O, NNH, and NH. Figure 3.10 shows the snapshot of NO_x species on a cross-section of the JSR. This figure shows that N_2O and NNH have the highest concentrations in the regions where the concentrations of O-atom and H-atom are abundant. Both N_2O and NNH form NH through $NH + NO \iff N_2O + H$ and $NNH \iff N_2 + H$ reactions. O-atom, N_2O, and NH concentrations in the recirculation zone play an important

role in producing NO_x through reaction 21, 26, 31, 32, and 61 in Table 3.4. NNH an NH radicals decay quickly as they enter the recirculation zone. However, the concentration N_2O remains relatively high in the this zone. Similar to the RANS solution, NO concentration is highest in the recirculation zone due to the high residence time this zone provides.

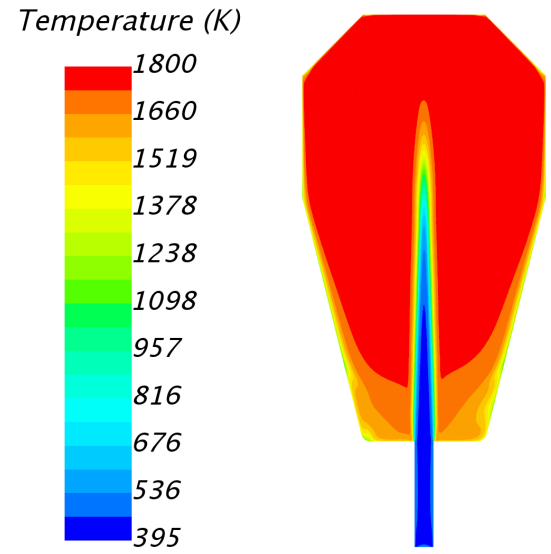

(a) Temperature

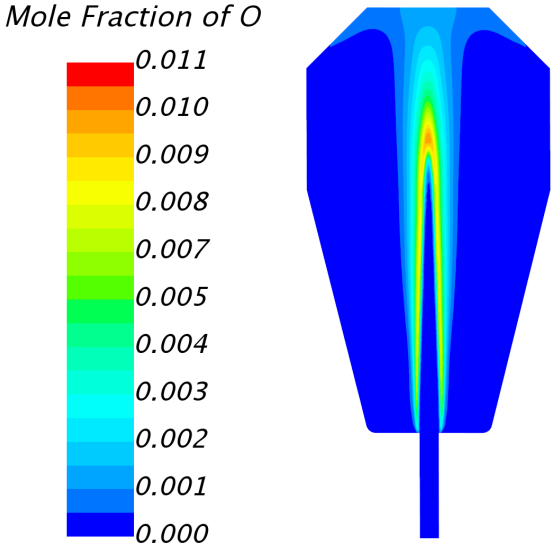

(b) O-atom Mole Fraction

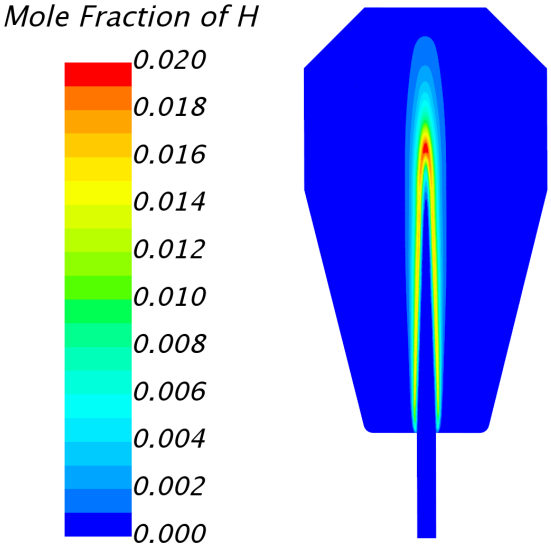

(c) H-atom Mole Fraction

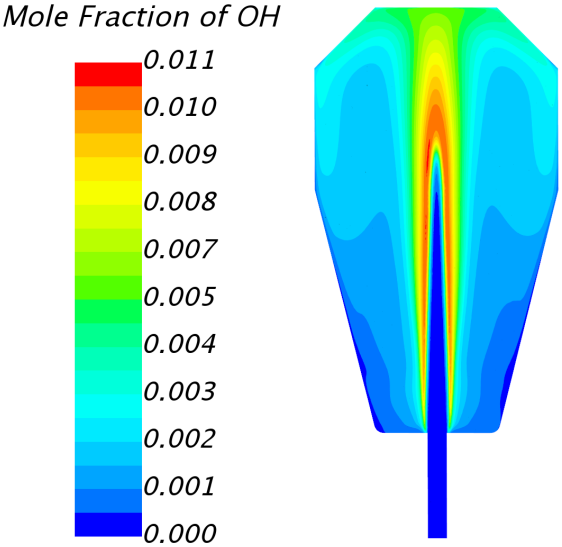

(d) OH-atom Mole Fraction

Figure 3.7: RANS solutions for combustion of hydrogen with NO_x chemistry.

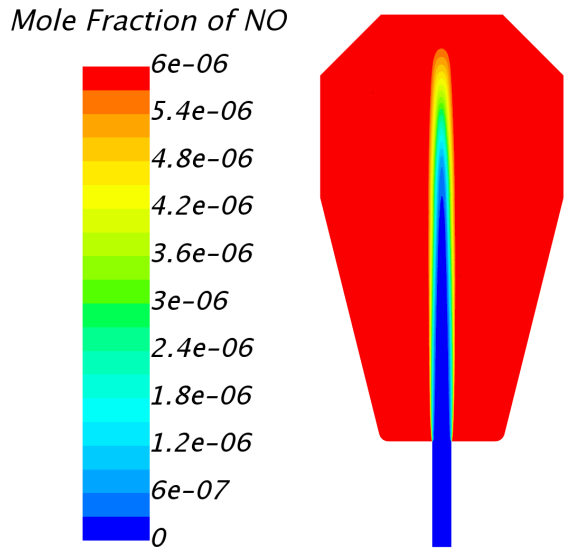

(a) NO Mole Fraction

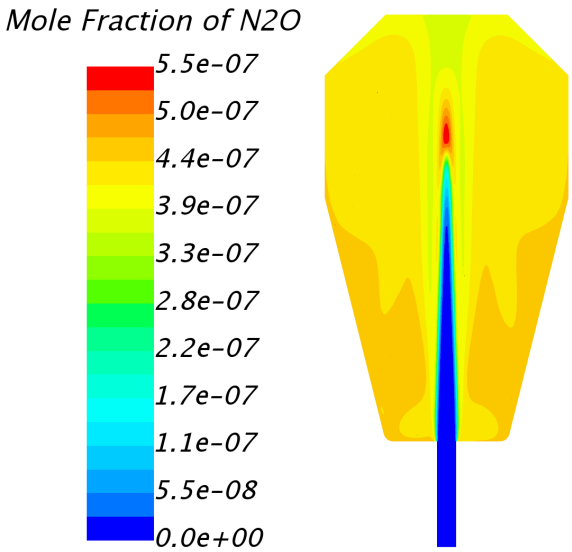

(b) N_2O Mole Fraction

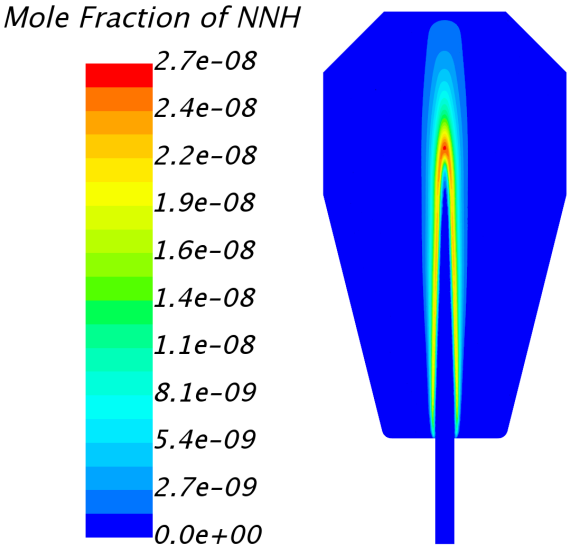

(c) NNH Mole Fraction

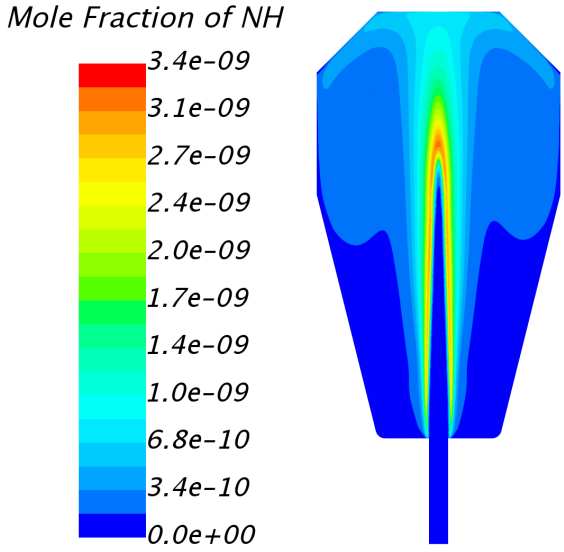

(d) NH Mole Fraction

Figure 3.8: RANS solutions for combustion of hydrogen with NO_x chemistry.

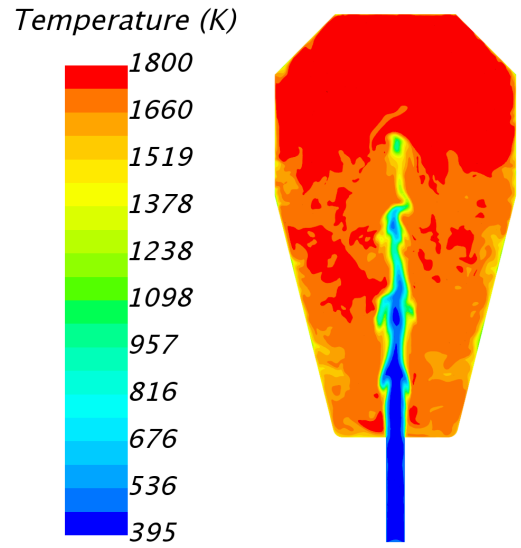

(a) Temperature

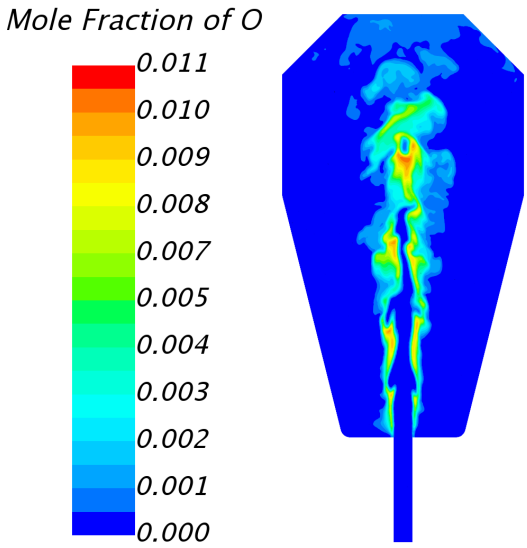

(b) O-atom Mole Fraction

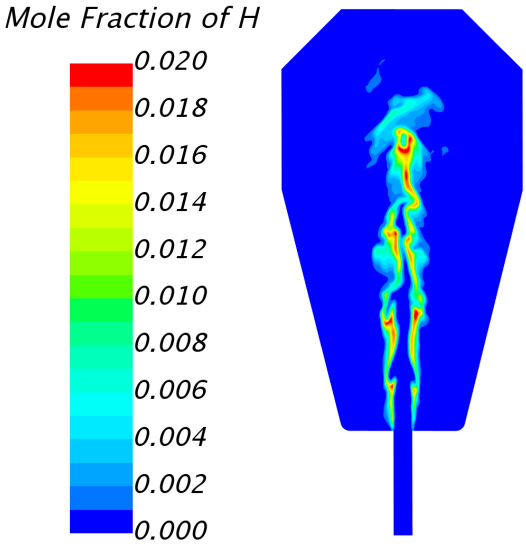

(c) H-atom Mole Fraction

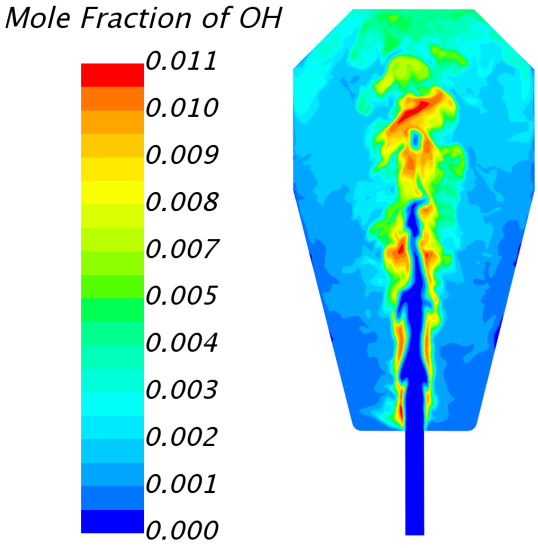

(d) OH-atom Mole Fraction

Figure 3.9: LES snapshots for combustion of hydrogen with NO_x chemistry.

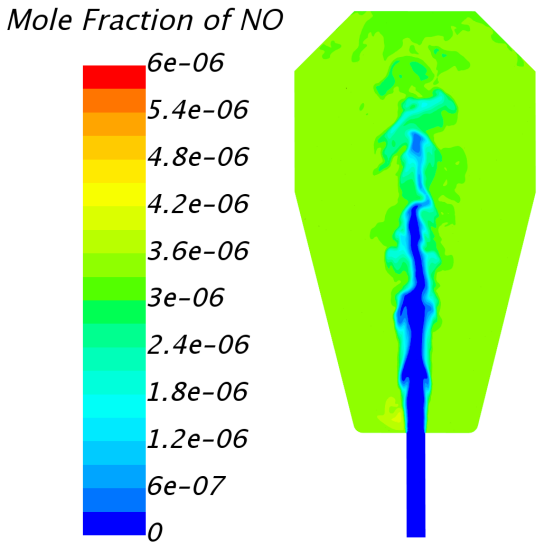

(a) NO Mole Fraction

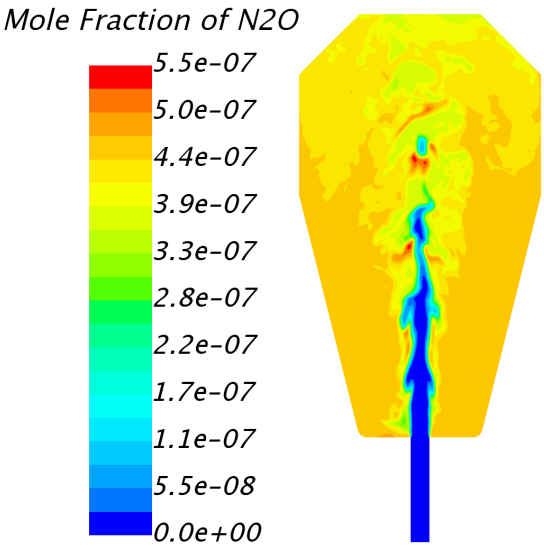

(b) N_2O Mole Fraction

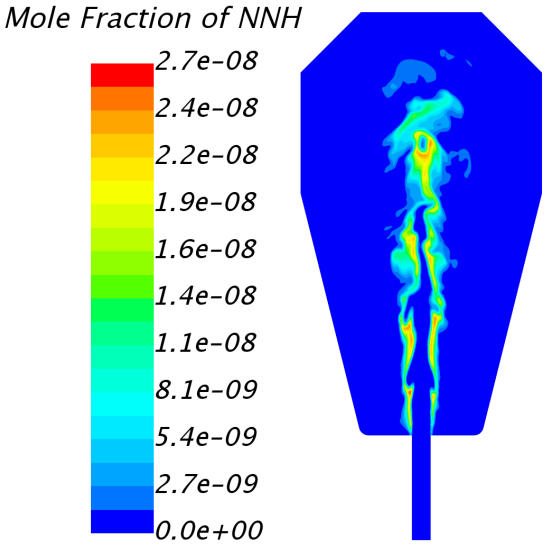

(c) NNH Mole Fraction

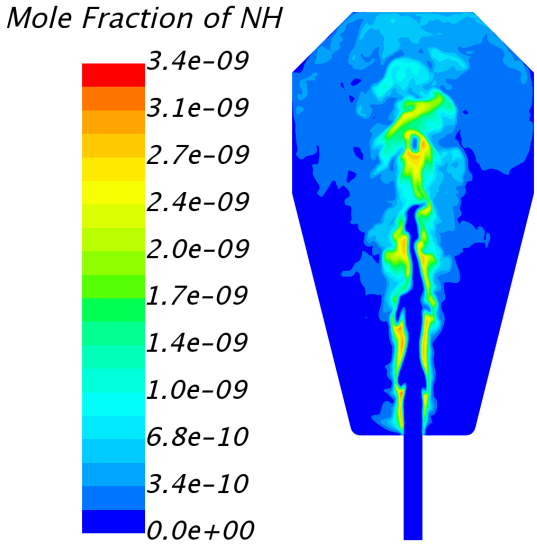

(d) NH Mole Fraction

Figure 3.10: LES snapshots for combustion of hydrogen with NO_x chemistry.

Since the concentration of O-atom and H-atom are highest in the flame brush, the ROP of NO_x species are highest in the flame brush as well. Figures 3.11 shows the ROP of NO, N_2O, NNH, and NH. The positive values mean the rate at which species are produced while the negative values describe the rate of destruction. These contour plots show that rates of production and destruction of N_2O, NNH, and NH are highest in the flame brush and in the strained flame along the sides of the jet. This is due to high concentrations of radicals present in this region that attack N_2 molecules in the jet. Figure C.1 shows a higher resolution in the recirculation zone for the ROP of NO.

In this figure, NO also has the highest ROP around the jet where concentration of O-atom and H-atom as well as N_2O and NH are high. However, NO concentration is highest in the recirculation zone where plenty of time is available to form NO through Zeldovich and N_2O routes. A plot of ROP for NO with higher resolution in the recirculation zone is provided in Appendix C.

For this LES simulation, solution is allowed to develop for 2 times the residence time and then statistics of the flow are monitored for a time equal to 2 times the mean residence time of the JSR. These statistics are used to find the mean values of temperature and species obtained. Mean temperature and NO profiles from the LES simulation are compared to experiments and the RANS solution. These profiles are plotted on a line from the centerline to the wall at $2/3^{rd}$ height of the reactor in Figure 3.12.

This plot shows that the measured temperature is around 1810 K in the recirculation zone and gradually lowers to about 1760 K on the centerline. The temperature predicted in the recirculation zone is in agreement for the RANS simulation compared to measurements. The mean temperature found in the recirculation zone is 1770 K for the LES simulation which is about 40 degrees lower than the measured value. However, the mean temperature at the center of the JSR is lower for the RANS simulation compared to experiments, which indicates a longer jet in the case of RANS. The LES simulation follows the temperature profile of experiments better compared to RANS. The jet length is slightly over-predicted in the LES simulation.

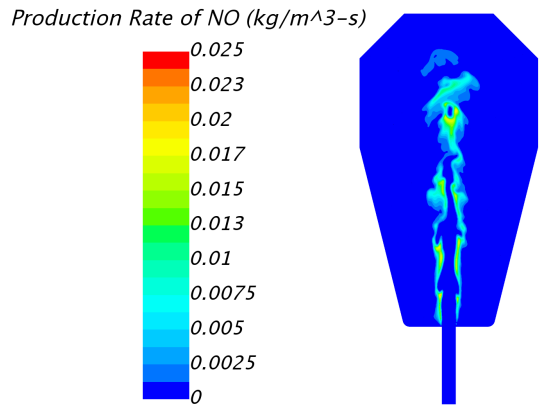

(a) NO Rate of Production

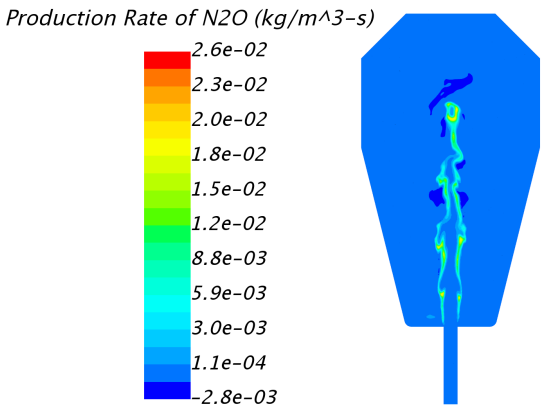

(b) N2O Rate of Production

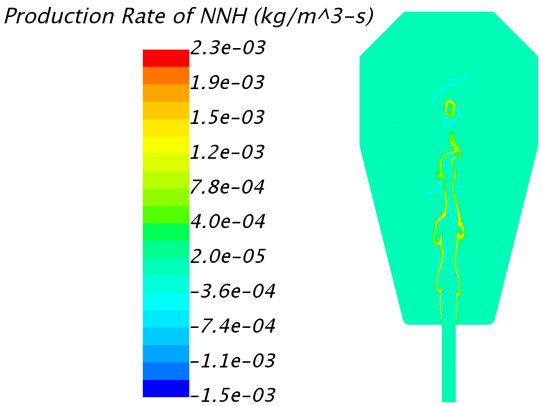

(c) NNH Rate of Production

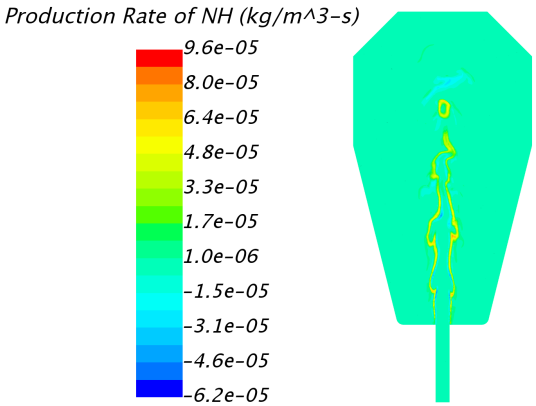

(d) NH Rate of Production

Figure 3.11: LES snapshots for combustion of hydrogen with NO_x chemistry.

Figure 3.13 shows the comparison between NO_x profiles obtained with CFD and experiments. NO_x is over predicted using RANS compared to the experiment. NO_x measured in the recirculation zone is around 7 ppm on a dry basis. RANS results predict NO_x to be around 9 ppm (on a dry basis) in the recirculation zone. LES slightly under-predicts NO_x. At the sampling location, predicted NO_x is about 5 ppm on a dry basis in the JSR. This under-preditcion is mainly due to under-prediction of recirculation zone temperature

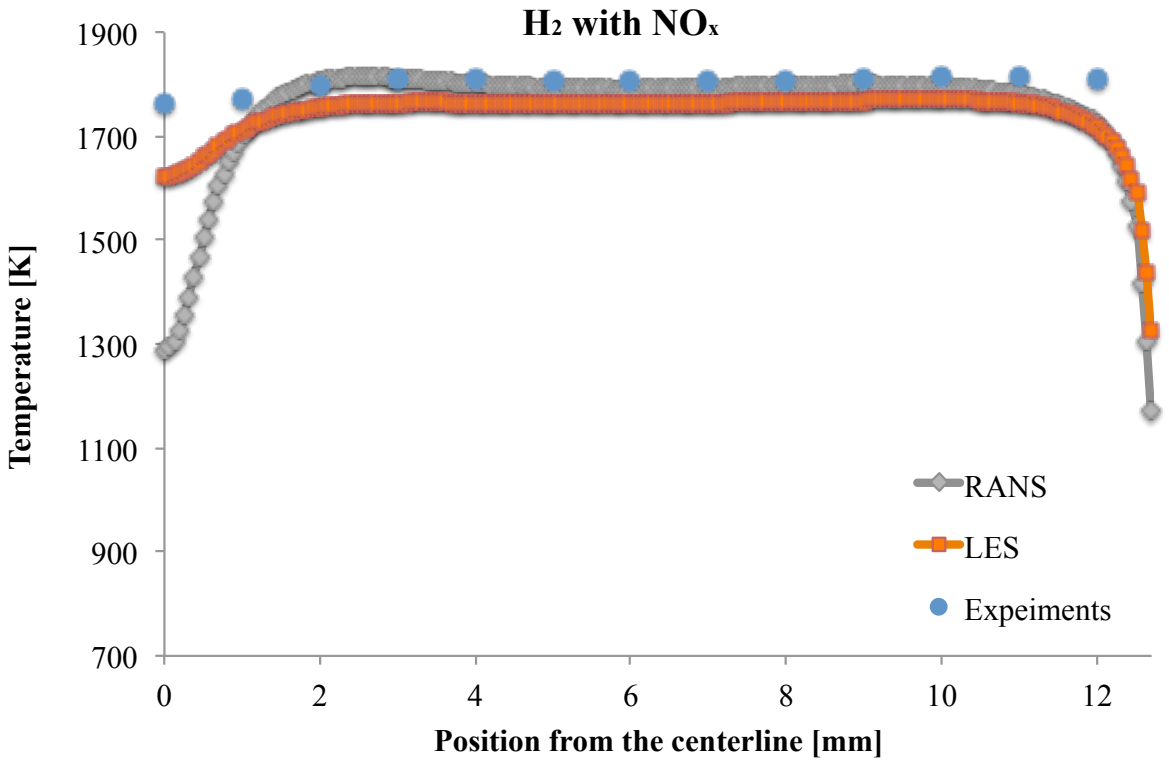

Figure 3.12: Comparison of temperature between RANS and LES simulations with experiments. These values correspond to temperature sampled at $2/3^{rd}$ height of the reactor going from centerline of the JSR to the wall.

by 40°C.

The solution history obtained from the LES simulation is used to determine the temperature and radical fluctuations over a residence time at the location where temperature and gas sampling are performed during experiments ($2/3^{rd}$ height and 10 mm from the centerline of the JSR). Figure 3.14 shows the fluctuations of temperature, O-atom, H-atom, and NO at this sampling location.

Large fluctuations in temperature and species concentrations are observed in this figure. This is possibly due to pockets of low temperature and high concentration radicals that have flown along the wall of the reactor from the impingement point of the jet to the sampling

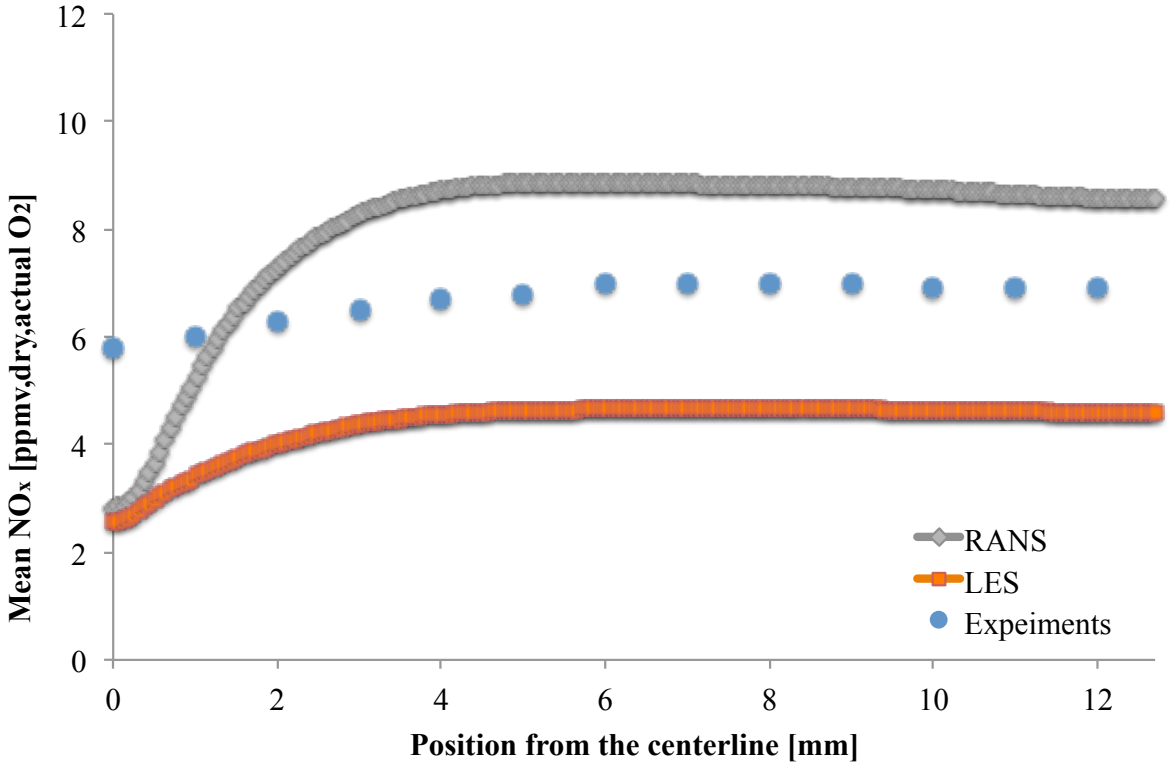

Figure 3.13: Comparison of NO_x found using RANS and LES simulations with experiments. These values correspond to NO_x values sampled at $2/3^{rd}$ height of the reactor going from centerline of the JSR to the wall.

location. They are not as fully reacted as the mean gas in the recirculation zone. Figure 3.14 also shows that NO_x concentration fluctuates slightly at the sampling location. The highest peak-to-peak amplitude of NO_x fluctuation is only about 0.2 ppm. This occurs because NO_x is formed through out the reactor and hence the predicted concentration in essence represents an average over many events in the reactor.

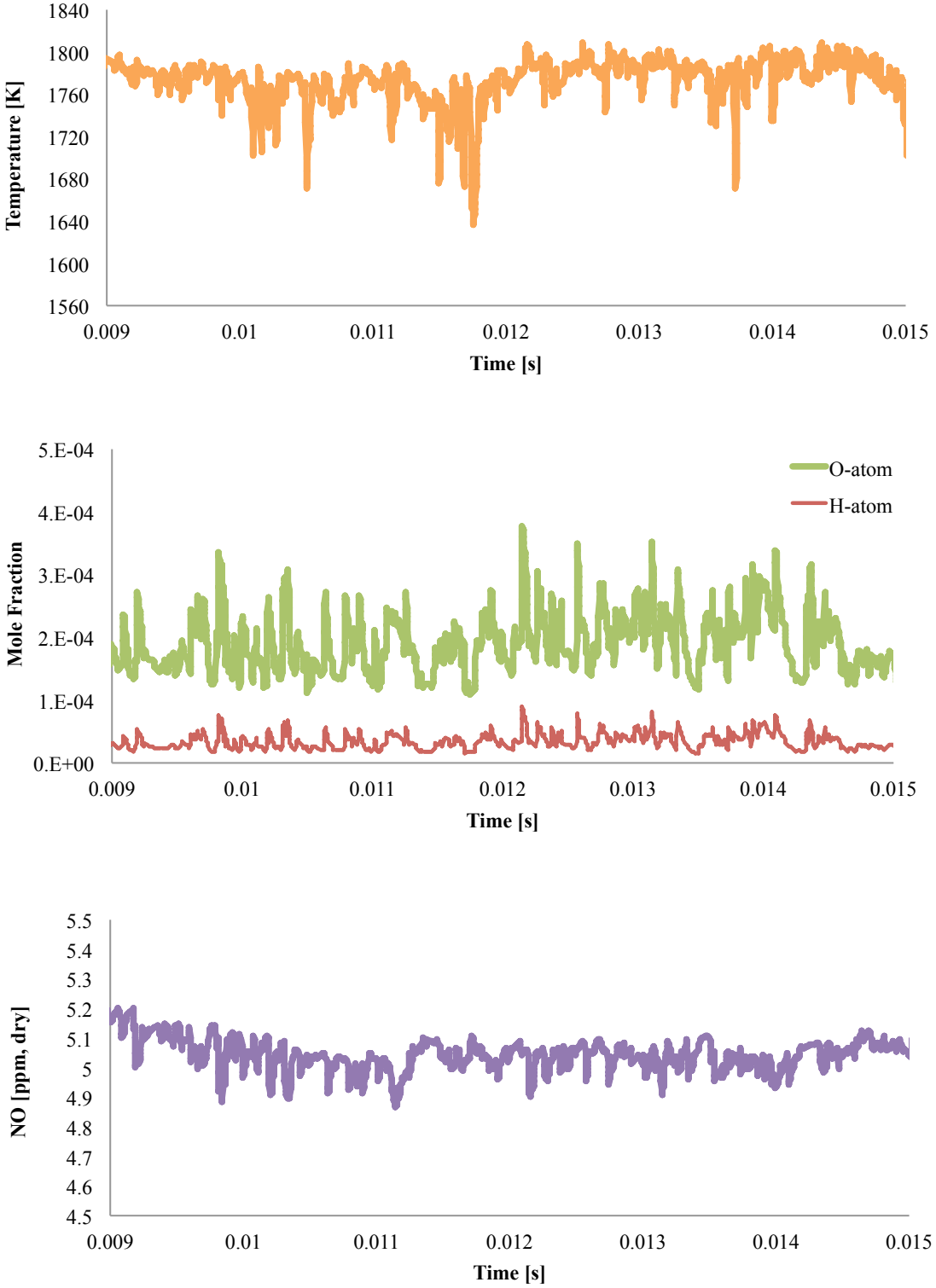

Figure 3.14: Fluctuations of temperature, NO, O-atom, and H-atom with respect to time at the sampling location for combustion of H_2 with nitrogen chemistry.

The summary of the mean, RMS, and the ratio of the two is given in Table 3.5. The average value of temperature at the sampling location is 1770 K. This value is about 40 degrees lower than the measured value. Similarly, attaining the average value of sampled data points show the average NO_x value is about 5 ppmv on a dry basis. This is about 2 ppm less than the experimental measurement by Fackler. The reason for this under-prediction is the lower temperature predicted in the recirculation zone of the reactor.

	Temperature [K]	O-atom	H-atom	NO [ppm, dry]
Mean	1770	1.88E-4	3.35E-5	5
RMS	1770	1.94E-4	3.56E-5	5
RMS/Mean	1	1	1.1	1

Table 3.5: Summary of mean, rms, and their ratios for temperature, o-atom, h-atom and NO at the sampling location.

3.3.3 CH_4

In this section, methane combustion is simulated using RANS and LES models. Combustion of methane is more consistent with the chemistry of higher hydrocarbon in liquid fuels compared to hydrogen. Due to lack of computational resources and high computational demand of running LES simulations with the Complex Chemistry, NO_x is not modeled here. The main goal of this study is to determine the fluid structure and chemistry inside the JSR and examine the radical fluctuations in the JSR. This simulation is the basis for the development of the CRN model in Chapter 4.

Figure 3.15 shows the contour plots of temperature and important species on a cross-section of the JSR using the RANS model. These plots show that the jet of premixed methane and air is longer than the hydrogen and air jet, almost reaching the impingement

point at the top of the reactor. This is due to slower breakdown of CH_4 as hot recirculation gases are entrained into the jet, compared to H_2. In these plots, O-atom and H-atom peak near the top wall of the reactor. CH radical is formed in a thin sheet around the jet as CH_4 breaks down to CH_3, CH_2, and finally to CH.

Figure 3.16 and Figure 3.17 show snapshots of the LES solution for temperature and important species. All snapshots correspond to the same physical time of 8.5 ms. Figure 3.16 shows that the flame brush occupies a larger volume in the JSR compared to the flame brush observed in the combustion of hydrogen. The jet is also longer in this case compared to hydrogen. This is due to slower burning rate of methane compared to hydrogen. The snapshots also show that the high pockets of radicals such as O-atom, H-atom, OH are shed mainly from the top of the jet as it reaches the impingement point.

Figure 3.17 shows that methane does not fully burn before the jet hits the top wall. CH radical is formed in thin flame sheets along the sides of the jet as H-atom is abstracted from CH_4 and converted to other species. This figure shows that CH only exists in the flame brush and in the thin flame along the sides of the jet. The CH concentration drops quickly after this region. This region also corresponds to the location with highest chemical heat release rate as shown in Figure 3.17. CH radical plays a significant role in prompt NO_x as it will be discussed in the next chapter.

Similar to the previous sections, statistics of the flow are recorded for just over a residence time of the JSR. As shown in Figure 3.18, a good agreement between the temperature profiles measured and predicted by LES is found at $2/3^{rd}$ height of the reactor. The mean temperature in the recirculation zone predicted by LES is only 10 degrees lower than the experiments. However, RANS modeling shows a much longer jet than expected. Different low-fidelity turbulence models such as Reynolds Stress Model can be used to obtain a better solution for methane as shown by Fackler [24] and Karalus [34].

The time history solution obtained for temperature, O-atom and H-atom at the sampling point is presented in Figure 3.19. Although CH radical plays an important role in the amount of NO_x produced in the combustion of methane through the prompt pathway, it is

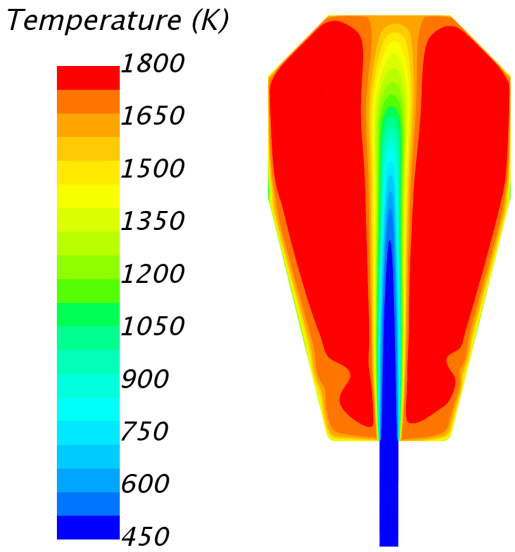

(a) Temperature

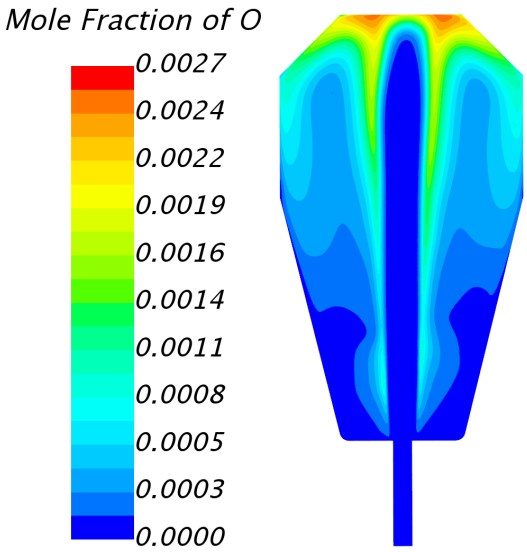

(b) O-atom Mole Fraction

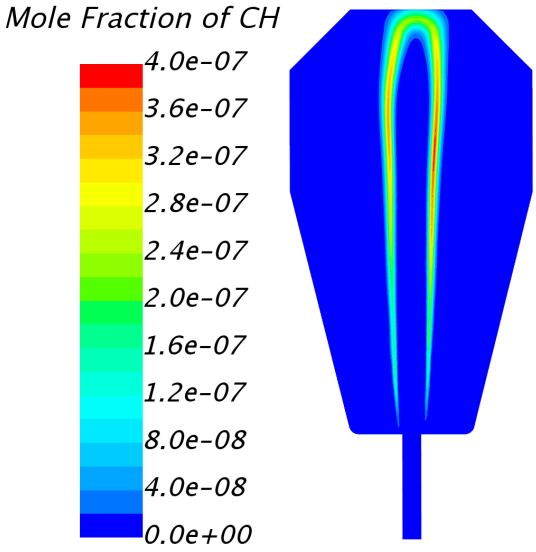

(c) CH Mole Fraction

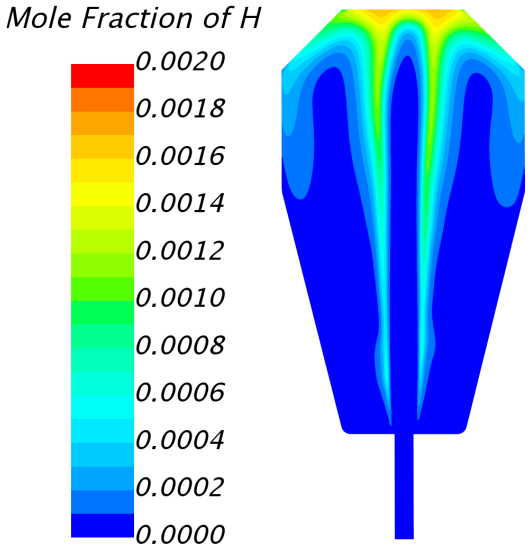

(d) H-atom Mole Fraction

Figure 3.15: RANS solution for combustion of methane.

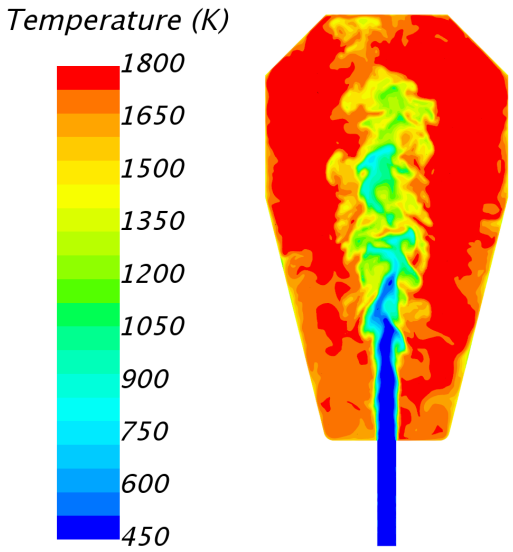

(a) Temperature

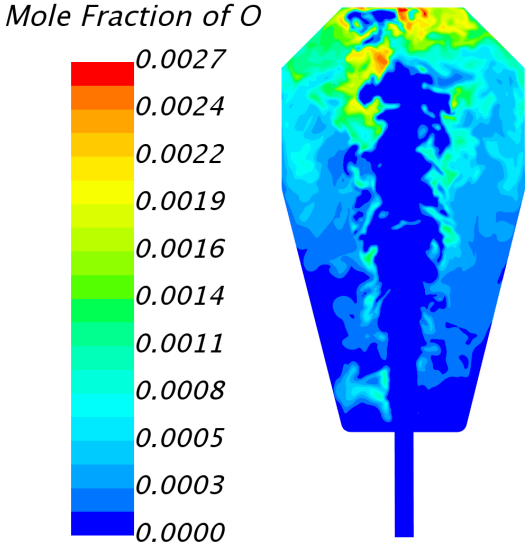

(b) O-atom Mole Fraction

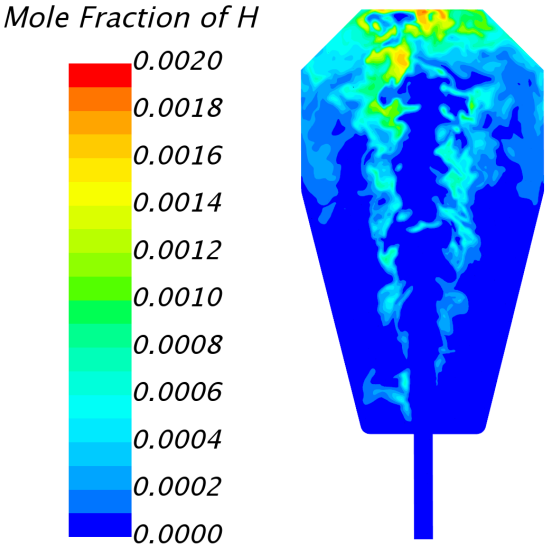

(c) H Mole Fraction

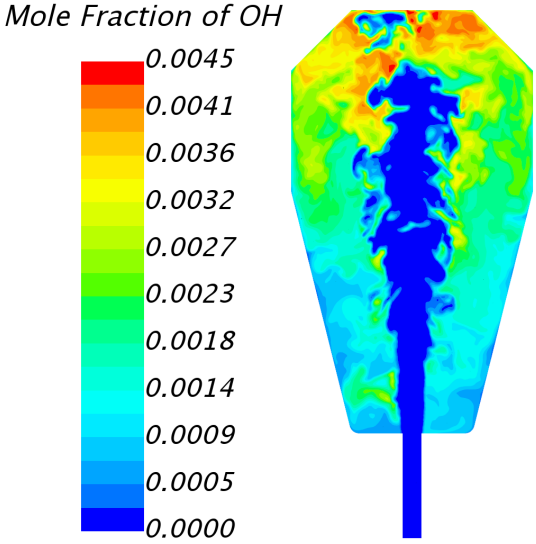

(d) OH Mole Fraction

Figure 3.16: LES solution for combustion of methane.

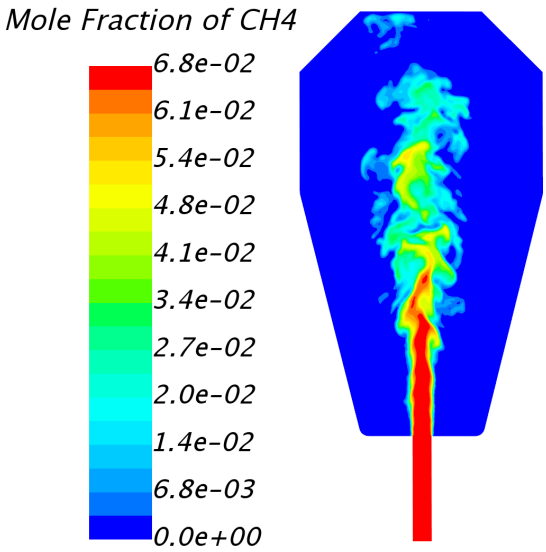

(a) CH_4 Mole Fraction

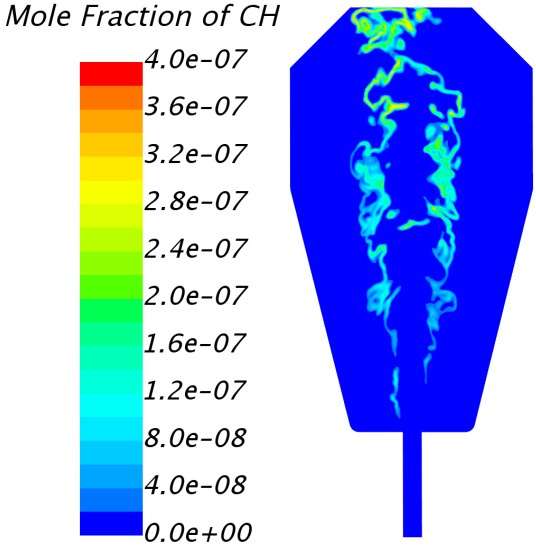

(b) CH Mole Fraction

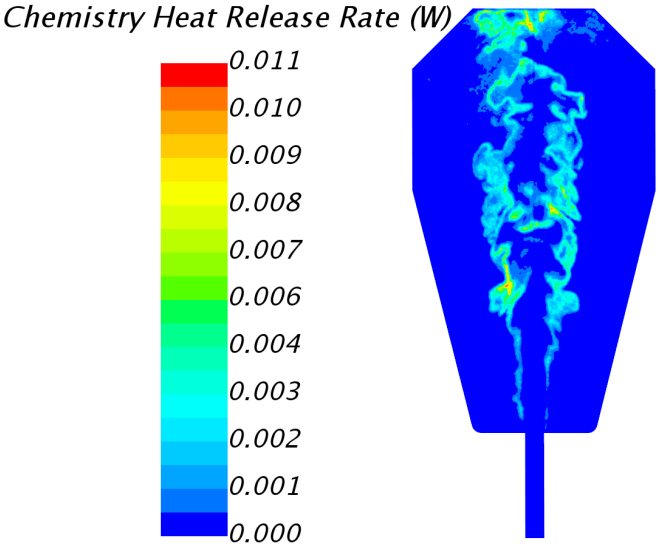

(c) Chemistry heat Release Rate

Figure 3.17: LES solution for combustion of methane.

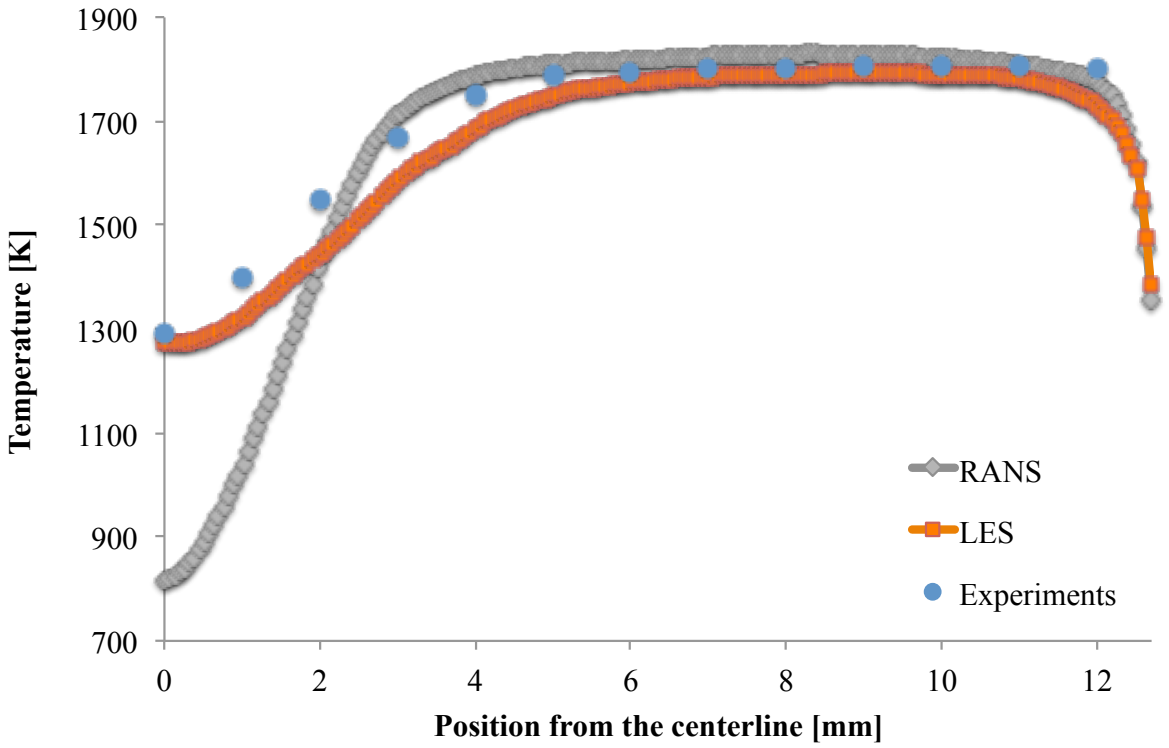

Figure 3.18: Comparison between RANS and LES simulations with experiments for temperature profile at $2/3^{rd}$ height in reactor, from centerline to wall.

not considered for sampling. As Figure 3.17 shows, the CH radical is formed in thin sheets in the flame zone and its mole fraction is near zero at the sampling location.

The mean values are provided in Table 3.6. Mean temperature obtained using this solution history shows the mean temperature is around 1790 K, which is about 15 degrees lower than the measured value. Average O-atom and H-atom mole fractions are 5.44E-4 and 1.64E-4, respectively.

Temperature fluctuations at the sampling location in Figure 3.19 show that the maximum peak-to-peak amplitude of fluctuations is about 100 K. The O-atom mole fraction fluctuations are also significant with a peak-to-peak value of 7.7E-4. These fluctuations are significant, however, they will not affect NO_x as much. This is because it requires higher residence time

	Temperature [K]	O-atom	H-atom
Mean	1790	5.44E-4	1.64E-4
RMS	1790	5.64E-4	1.76E-4
RMS/Mean	1	1.04	1.08

Table 3.6: Summary of mean, rms, and their ratios for temperature, o-atom, and h-atom at the sampling location.

to form NO_x (through Zeldovich, N_2O, and NNH paths) compared to the period of these fluctuations.

3.3.4 Summary of findings

In this chapter, CFD is used to model the fluid structure and chemistry inside the JSR. The results found using CFD simulations of simple fuels aid in generating a CRN model that can be used for the prediction of NO_x emissions from the combustion of pre-vaporized, premixed liquid fuels. The main goal of the CFD work is to explore the temperature and species fluctuations in the recirculation zone of the JSR as well as determining how NO_x species are formed/destroyed inside the reactor.

The RANS turbulence model is used to initialize the Large Eddy Simulation modeling of the flow. Modeling chemistry correctly is essential for this study, therefore, the Complex Chemistry model with the Laminar Flame Concept (LFC) is utilized. This model solves transport equations for species and calculates reaction rates by the modified Arrhenius kinetic expressions.

The findings of this chapter are summarized below:

1. LES modeling of H_2 combustion with NO_x chemistry shows that most of the radicals are mainly formed in the flame brush. O-atom, H-atom, and OH radical have the

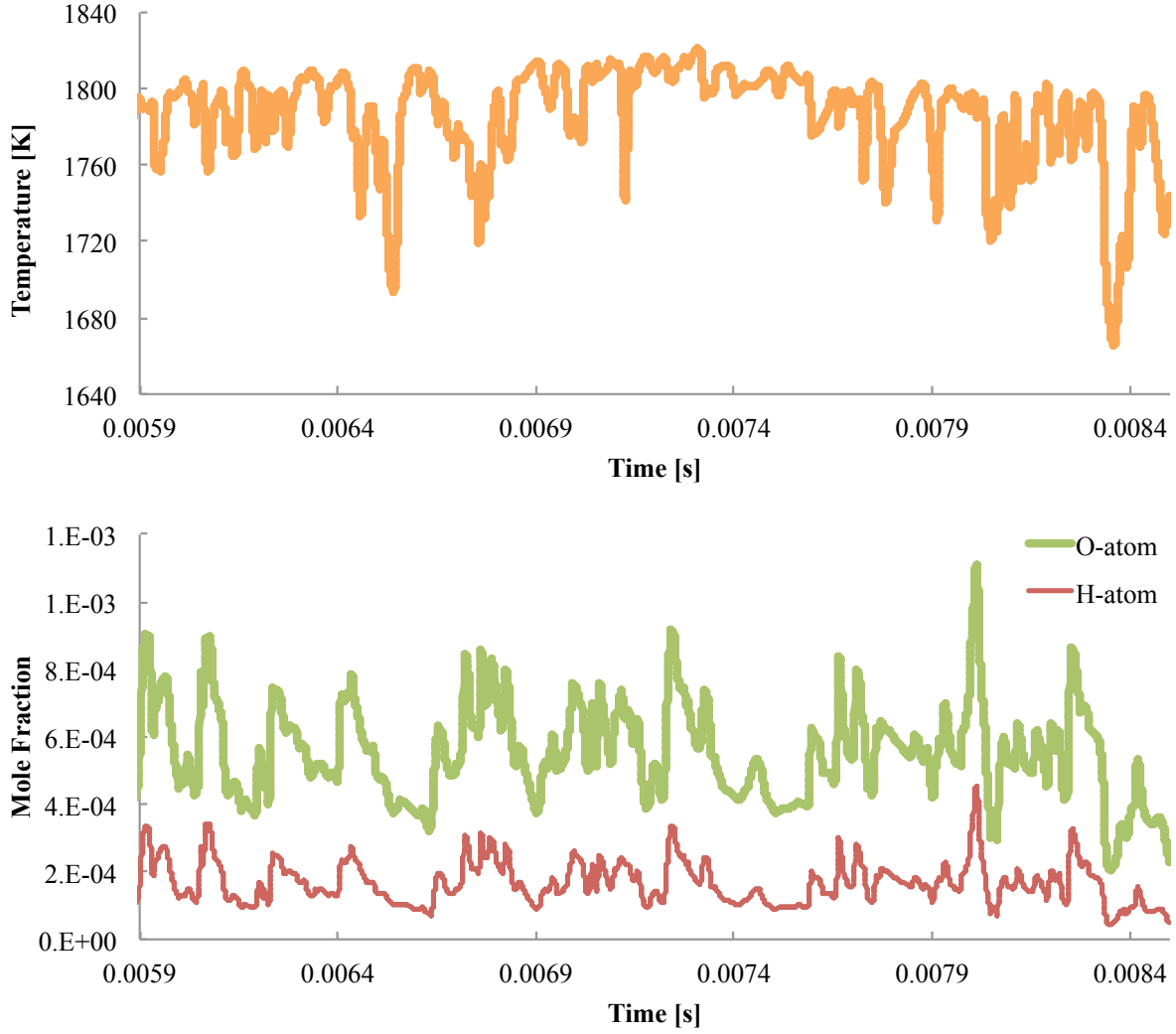

Figure 3.19: Fluctuations of temperature, O-atom, and H-atom with respect to time at the sampling location for combustion of CH_4.

highest concentrations in this region. These radicals react with nitrogen molecules and form important NO_x species such as N_2O, NNH, and NH. Since the concentration of O-atom and H-atom are highest in the flame brush, the ROP of NO_x species are highest in the flame brush as well. NO_x has the highest concentration in the recirculation zone due to the high residence time this zone provides.

2. The data history obtained for a time equal to 2-3 times the mean residence time of the JSR. The temperature, O-atom, and H-atom fluctuations in the sampling location of the reactor is not negligible. However, the case of H_2 with NO_x chemistry shows that NO_x mole fraction fluctuates only about 0.1 *ppm* from the mean value of 5 ppm on a dry basis. This predicted mean value is only 2 ppm lower than the measured value. This under-prediction is due to the mean temperature being predicted 40 degrees lower than it is measured.

3. LES modeling of CH_4 combustion shows that the jet occupies a larger volume in the JSR compared to the jet observed in the combustion of hydrogen. This is perhaps due to the slower chemistry of CH_4. The mean temperature at the recirculation zone is predicted to be at 1790 K, which is in good agreement with the measured value of 1805 K. The time history of the solution at the sampling location shows that temperature and species fluctuations are significant.

Chapter 4

CHEMICAL KINETIC MODELING

In the previous chapter, CFD is used to analyze the fluid structure inside the JSR. These CFD simulations use simple fuels such as H_2 and CH_4 with a relatively small set of species and reactions. However, modeling the flow using LES for liquid fuels with thousands of species and reactions is not feasible given the computational resources available during this decade. In this chapter, chemical kinetic modeling is used to analyze the pathways towards pollutant formation from the combustion of fuels in the JSR.

As mentioned in Chapter 2, only methane, iso-octane, n-octane, n-dodecane, toluene, and 135-TMB are modeled. The CFD simulations of Chapter 3 are used to develop a Chemical Reactor Network (CRN) model that zonally represents the reactor and solves the chemistry within the reactor. Both individual and surrogate fuel mechanisms are used in the CRN to find the sensitivity of the this work on mechanisms. In addition, different NO_x mechanisms are incorporated in the hydrocarbon mechanisms to study the reaction pathways to NO_x formation. CRN modeling is performed for measured recirculation zone temperatures of 1700, 1800, and 1900 K and compared to measured NO_x and CO concentrations. Finally, the difference between NO_x formation among aliphatic and aromatic fuels is explained.

4.1 Background

Chemical kinetic modeling performed in this chapter utilizes ANSYS CHEMKIN-PRO [1]. Conservation of mass, momentum, and energy are considered using 2 types of volumes. A zero-dimensional perfectly stirred reactor, PSR, or a one-dimensional plug flow reactor, PFR, can be used to analyze the behavior of reaction pathways and predict species concentrations and temperature.

The contents inside a PSR are assumed to be spatially uniform and the rate at which reactants convert to products is controlled by chemical reaction rates. The PSR can either be solved as a constant temperature problem in which temperature is set to a fixed value, or an energy equation problem in which the reactor can have a certain heat loss and the temperature is then solved from conservation of energy.

Table 4.1 shows three kinds of PSR that are used to develop the CRN model in the next section. PSB is defined as an adiabatic PSR that is 1% larger than the smallest volume that will sustain combustion. This reactor represents the regions of primary flame in the reactor, which typically are associated with peak CH radical concentration. The recirculation zone is modeled using a PST, which is a PSR at a fixed temperature (measured recirculation zone temperature). It is the largest zone of the reactor and represents near-post-flame reaction. The other PSRs are adiabatic reactors with a given volume that are used to model intermediate flame regions.

Reactor Type	Definition
PSB	An adiabatic PSR that is 1% larger than the blowout volume
PST	A perfectly stirred reactor at a fixed temperature
PSR	An adiabatic PSR

Table 4.1: Definitions of common reactors in chemical kinetic modeling in the following section.

4.2 Chemical Kinetic Mechanisms

A chemical kinetic mechanism is a combination of species and reactions that represents the combustion of a pure or a mixture of a few pure fuels to represent a complex blended fuel called a surrogate fuel. The reactions provided in each mechanism dictate the rate at which species are formed or destroyed during the combustion process. Typically, a mechanism

contains reactions that represent the breakdown of a certain fuel to lighter fuels and new species.

In this work, six hydrocarbon mechanisms are used to to perform chemical kinetic modeling on the fuels used in this chapter. GRI3.0 mechanism is commonly used to study the combustion of methane. This mechanism was developed under Gas Research Institute support, and was presented in 1999 by Smith at al. [32]. Iso-octane is modeled using Mehl et al. [56] mechanism. This work is the result of a collaboration between Lawrence Livermore National Laboratory (LLNL) and the Combustion Chemistry Center of National University of Ireland.

Normal alkane fuels (n-octane and n-dodecane) are modeled using Sarathy et al. [74] mechanism. This mechanism includes comprehensive chemical kinetics of normal alkanes from C_7 to C_{20}. This mechanism is the collaboration between the LLNL and a few U.S. universities. The two aromatic fuels, toluene and 135-TMB, are modeled using Yuan et al. [87] and Dievart [18] mechanisms respectively. The toluene mechanism is a combined effort of the University of Science and Technology of China and Institut de Combustion de France while the 135-TMB mechanism is from the collaboration between Princeton, Rensselaer Polytechnic Institute, and University of Limerick in Ireland. A summary of all chemical kinetic mechanisms used in this chapter along with their corresponding number of species and reactions are presented in Table 4.2. Each mechanism provides the thermo-chemistry data for species contained in the mechanism.

The mechanisms discussed so far are designated to model combustion of an individual fuel. Comparing the combustion products of these fuels using chemical kinetic modeling is difficult. Each of these mechanisms may use different reaction rates for important elementary reactions that result in NO_x. For example, the reactions rates for $H_2 - O_2$ abstraction which have an important effect on NO_x formation and destruction may be different among the mechanisms used. To avoid this inconsistency, a surrogate jet fuel mechanism that models jet fuel using n-octane, iso-octane, and toluene mechanisms is used for comparison to individual mechanisms. In this case, the Dooley et al. [20] mechanism is used to model methane,

Purpose	# of Species	# of Reactions	Mechanism Ref.
Methane (GRI 3.0)	53	325	Smith at al. [32]
Iso-octane	1550	8000	Mehl et al. [56]
N-alkanes	7200	31400	Sarathy et al. [74]
Toluene	272	1698	Yuan et al. [87]
135-TMB	444	2567	Dievart et al. [18]
Surrogate jet fuel	1599	6633	Dooley et al. [20]
O-H-N NO_x	17	64	Klippenstein et al. [38]
Prompt NO_x	16	11	Glarborg et al. [31]
Prompt NO_x	23	26	Konnov [39]

Table 4.2: Summary of all chemical kinetic mechanisms used for CRN modeling of JSR.

iso-octane, n-octane, and toluene. The thermo-chemical data of Dooley et al. is used for hydrocarbon reactions.

Some of the hydrocarbon fuel mechanisms do not include pathways to create/destroy C_2O. For this reason, the reactions in Table 4.3 are added from the Miller and Melius [58] mechanism (which are included in the Yuan et al. toluene mechanism) to methane, iso-octane, n-alkanes, 135-TMB, and the surrogate jet fuel mechanisms. Additionally, the Dooley et al. mechanism does not include reactions for destruction of C-atom, $C + OH \iff CO + H$ and $C + O_2 \iff CO + O$. These two reactions are added from GRI3.0 to the Dooley et al. mechanism.

NO_x formation is modeled using various mechanisms available in the literature. GRI3.0 mechanism was initially used to model NO_x in the JSR, however, some of the reaction rates for NO_x are believed to be outdated, so this NO_x mechanism is not considered here. A more recent mechanism for modeling NO_x is published for O, H,and N chemistry by Klippenstein et al. [38]. This mechanism is based on Miller and Glarborg's mechanism [57] published in 1999.

Eq #	Reaction	A	n	$E_A[cal/mol]$
1	$HCCO + OH \iff C2O + H2O$	3.0E+13	0	0
2	$C_2O + H \iff CH + CO$	5.0E+13	0	0
3	$C_2O + O \iff CO + CO$	5.0E+13	0	0
4	$C_2O + OH \iff CO + CO + H$	2.0E+13	0	0
5	$C_2O + O_2 \iff CO + CO + O$	2.0E+13	0	0

Table 4.3: Reactions of Miller and Melius [58] mechanism for C_2 from added to Smith et al., Mehl et al., Sarathy et al., Dievart et al., and Dooley et al. mechanisms

Major improvements to the thermo-chemistry and reactions rates of NNH are performed in this mechanism by Klippenstein et al. The thermo-chemical data used for each nitrogen species in this mechanism is taken from Klippenstein et al. thermo-chemical data file (This thermo-chemical data file is obtained from Dr. Klippenstein by personal communications).

The O-H-N NO_x mechanism of Klippenstein et al. is shown in Table 4.4. The first 19 reactions of this mechanism play a negligible role here, but are essential in rich combustion or systems that have ammonia injection. Reactions 30-32 are the Zeldovich mechanism, while reactions 59-64 represent the N_2O mechanism. The NNH mechanism contains reactions 33 to 40. Reactions involving NO_2 have essentially no net impact on NO concentration. The NO_x formed by this chemistry in the JSR is essentially all NO ($NO_2 \ll NO$). Reactions 41 to 58 are related HNO and N_2O reduction/production to NO.

Each reaction is represented by its rate constant, expressed in terms of three constants as shown in Equation 4.1. In this equation, k is the rate constant, A is the pre-exponential factor, n is a constant, and E_A is the activation energy. These coefficients for the forward reactions are provided in Tables 4.4, 4.5, and 4.6 for their corresponding NO_x mechanism.

$$k = A\ T^n exp(-\frac{E_A}{RT}) \tag{4.1}$$

Eq #	Reaction	A	n	$E_A[cal/mol]$
1	$NH_3 + M \iff NH_2 + H + M$	2.2E+16	0.00	93,470
2	$NH_3 + H \iff NH_2 + H_2$	6.4E+5	2.39	10,171
3	$NH_3 + O \iff NH_2 + OH$	2.8E+02	3.29	4471
4	$NH_3 + OH \iff NH_2 + H_2O$	2.0E+6	2.04	566
5	$NH_3 + HO_2 \iff NH_2 + H_2O_2$	3.0E+11	0.00	22,000
6	$NH_2 + H \iff NH + H_2$	7.2E+5	2.32	799
7	$NH_2 + O \iff HNO + H$	6.6E+13	0.00	0
8	$NH_2 + O \iff NH + OH$	7.00E+12	0.00	0
9	$NH_2 + OH \iff NH + H_2O$	3.3E+06	1.949	-217
10	$NH_2 + HO_2 \iff H_2NO + OH$	5.00E+13	0.00	0
11	$NH_2 + HO_2 \iff NH_3 + O_2$	9.2E+05	1.94	-1152
12	$NH_2 + O_2 \iff H_2NO + O$	2.6E+11	0.4872	29,050
13	$NH_2 + O_2 \iff HNO + OH$	2.9E-2	3.764	18,185
14	$NH_2 + NO \iff N_2 + H_2O$	1.3E+16	-1.25	0
15	$NH_2 + NO \iff NNH + OH$	3.1E+13	-0.48	1180
16	$NH_2 + HNO \iff NH_3 + NO$	3.6E+6	1.63	-1250
17	$NH_2 + NO_2 \iff N_2O + H_2O$	3.0E+14	-0.77	242
18	$NH_2 + NO_2 \iff H_2NO + NO$	1.3E+15	-0.77	242
19	$NH_2 + HONO \iff H_2NO + NO$	7.1E+1	3.02	-4940
20	$NH + H \iff N + H_2$	3.0E+13	0	0
21	$NH + O \iff NO + H$	9.2E+13	0	0
22	$NH + OH \iff HNO + H$	3.2E+14	-0.376	-46
23	$NH + OH \iff N + H_2O$	1.6E+7	1.733	-576
24	$NH + O_2 \iff HNO + O$	4.6E+5	2.00	6500
25	$NH + O_2 \iff NO + OH$	1.3E+6	1.50	100
26	$NH + NO \iff N_2O + H$	1.8E+14	-0.351	-244
27	$NH + NO \iff N_2 + OH$	2.7E+12	-0.0721	-512
28	$NH + NO_2 \iff HNO + NO$	5.9E+12	0.00	0
29	$NH + NO_2 \iff N_2O + OH$	4.1E+12	0.00	0
30	$N + OH \iff NO + H$	3.8E+13	0.00	0
31	$N + O_2 \iff NO + O$	6.4E+9	1.00	6280
32	$N + NO \iff N_2 + O$	2.1E+13	0.00	0
33	$NNH \iff N_2 + H$	1.0E+9	0.00	0
34	$NNH + H \iff N_2 + H_2$	1.0E+14	0.00	0
35	$NNH + O \iff N_2O + H$	1.9E+14	-0.274	-22
36	$NNH + O \iff N_2 + OH$	1.2E+13	0.145	-217
37	$NNH + O \iff NH + NO$	5.2E+11	0.388	-409
38	$NNH + OH \iff N_2 + H_2O$	5.0E+13	0.00	0

39	$NNH + O_2 \iff N_2 + HO_2$	5.6E+14	-0.385	-13
40	$NNH + NO \iff N_2 + HNO$	5.0E+13	0.00	0
41	$NO + H + (M) \iff HNO(+M)$	1.5E+15	-0.41	0
42	$HNO + H \iff NO + H_2$	4.4E+11	0.72	650
43	$HNO + O \iff NO + OH$	2.3E+13	0.00	0
44	$HNO + OH \iff NO + H_2O$	3.6E+13	0.00	0
45	$HNO + O_2 \iff NO + HO_2$	2.0E+13	0.00	16,000
46	$H_2NO + M \iff HNO + H + M$	2.8E+24	-2.83	64,915
47	$H_2NO + H \iff HNO + H_2$	3.0E+7	2.00	2000
48	$H_2NO + H \iff NH_2 + OH$	5.0E+13	0.00	0
49	$H_2NO + O \iff HNO + OH$	3.0E+7	2.00	2000
50	$H_2NO + OH \iff HNO + H_2O$	2.0E+7	2.00	1000
51	$H_2NO + HO_2 \iff HNO + H_2O_2$	2.9E+4	2.69	-1600
52	$H_2NO + O_2 \iff HNO + HO_2$	3.0E+12	0.00	25,000
53	$NO + O + (M) \iff NO_2 + (M)$	1.3E+15	-0.75	0
54	$NO + HO_2 \iff NO_2 + OH$	2.1E+12	0.00	-497
55	$NO_2 + H \iff NO + OH$	1.3E+14	0.00	362
56	$NO_2 + O \iff NO + O_2$	1.1E+14	-0.52	0
57	$NO_2 + HO_2 \iff HONO + O_2$	1.9E+00	3.320	3044
58	$NO_2 + HO_2 \iff HNO_2 + O_2$	1.9E+1	3.26	4983
59	$N_2O + (M) \iff N_2 + O + (M)$	1.3E+12	0.00	62,570
60	$N_2O + H \iff N_2 + OH$	6.4E+7	1.835	13,492
61	$N_2O + O \iff NO + NO$	9.2E+13	0.00	27,679
62	$N_2O + O \iff N_2 + O_2$	3.7E+12	0.00	15,936
63	$N_2O + OH \iff N_2 + HO_2$	1.3E-2	4.72	36,560
64	$N_2O + OH \iff HNO + NO$	1.2E-4	4.33	25,080

Table 4.4: The O-H-N NO_x mechanism of Klippenstein et al. [38].

The NO_x mechanism by Klippenstein et al. does not include any prompt pathways which are important when modeling combustion of hydrocarbons. Two different prompt mechanisms are considered here, Konnov [39] and Glarborg et al. [31] mechanisms. A summary of these mechanisms with their corresponding number of species and reactions are presented in Table 4.2.

In 1971, Fenimore [27] proposed the prompt NO_x via the spin-forbidden $CH + N_2 \iff HCN + N$. This reaction is one of the most important findings explaining the conversion of molecular N_2 to N species yielding prompt NO_x. In 1977, Blauwens et al. [5] provided the first direct experimental evidence for the prompt NO_x formation by CH + N_2, based on Fenimore's mechanism.

In 2000, Moskaleva and Lin [61] showed that the reaction between CH radicals and N_2 yields NCN radicals and H, according to a spin-allowed reaction pathway. Since then, many studies have focused on measuring NCN radicals in flames, considering this reaction in prompt NO_x, and determining the rate constants of reactions involving NCN [16, 44, 81, 22, 26].

In 2007, Williams and Fleming [86] reported that a proper prediction of prompt NO_x formation could not be achieved by assuming CH as the only precursor species. They suggested that the $C_2O + N_2 \iff NCN + CO$ reaction might warrant consideration as a route for prompt NO_x formation, particularly in flames of C_2 and higher hydrocarbons. In 2009, Konnov [39] included this reaction in his prompt mechanism, Konnov0.5, in addition to some other reactions. This modified mechanism is the new release, Konnov0.6, and is shown in Table 4.5. The thermo-chemical data used for each nitrogen species in this mechanism are taken from Konnov thermo-chemical data file.

Eq #	Reaction	A	n	$E_A[cal/mol]$
1	$CH + N_2 \iff NCN + H$	3.0E+12	0	22,157
2	$CN + N_2 \iff NCN + H$	6.0E+13	0	15,360
3	$CN + N_2O \iff NCN + NO$	1.8E+10	0.00	1450
4	$CN + NCO \iff NCN + CO$	1.8E+13	0.00	0
5	$C_2O + N_2 \iff NCN + CO$	7.0E+11	0.00	17,000
6	$CH + N_2 \iff HNCN$	1.65E+21	-3.62	14,196
7	$HNCN + M \iff H + NCN + M$	1.79E+28	-3.44	64,502
8	$HNCN + O \iff NO + HCN$	1.22E+14	0.05	73.5
9	$HNCN + O \iff NH + NCO$	5.6E+13	0.05	73.5
10	$HNCN + O \iff CN + HNO$	9.36E+12	0.05	73.5
11	$HNCN + OH \iff NCN + H_2O$	8.28E+3	2.78	3135
12	$HNCN + O_2 \iff HO_2 + NCN$	1.26E+8	2.32	-1135
13	$NCN \iff N + CN$	2.95E+30	-5.29	117,090
14	$NCN \iff C + N_2$	2.66E+28	-5.32	83,110
15	$NCN \iff CNN$	3.69E+29	-5.84	78,410
16	$NCN + H \iff HCN + N$	1.89E+14	0.00	8425
17	$NCN + O \iff CN + NO$	2.54E+13	0.15	-34
18	$NCN + O \iff CO + N_2$	2.42E+2	2.32	1135
19	$NCN + O \iff N + NCO$	2.20E+9	0.41	-157

20	$NCN + N \iff N_2 + CN$	1.0E+13	0.00	0
21	$NCN + C \iff CN + CN$	1.0E+13	0	0
22	$NCN + OH \iff HCN + NO$	4.69E+10	0.44	4000
23	$NCN + O_2 \iff NO + NCO$	3.8E+9	0.51	24,590
24	$NCN + CH \iff HCN + CN$	3.21E+13	0.00	-860
25	$NCN + CN \iff C_2N_2 + N$	1.25E+14	0.00	8020
26	$NCN + CH_2 \iff H_2CN + CN$	7.99E+13	0.00	4630

Table 4.5: Prompt NO_x mechanism of Konnov [39].

In 2010, the Konnov prompt mechanism was criticized by Zhu et al. [89]. They mapped out triplet and singlet potential energy surfaces with the goal of investigating the role of the reaction of C_2O with N_2 in prompt-NO_x. They argued that their predicted reaction rate for $C_2O + N_2 \iff NCN + CO$ is significantly lower than the one used by Williams and Fleming [86] and Konnov [39], suggesting that Konnov's rate would over-predict NO_x concentration compared to experiments. Zhu et al. believe that uncertainties in the prediction of the concentrations of CH and C_2O may be improved with more reliable experimental and/or computational studies on their creation and destruction kinetics with various reactive combustion species.

On the other hand, in 2010, Lamoureux et al. [43] found that best prediction of NO_x can be found using Konnov's prompt mechanism. In their work, they measured the profiles of CH, NO, and NCN in flames of $CH_4 - O_2 - N_2$ and $C_2H_2 - O_2 - N_2$ (fuel-air equivalence ratio of 1 and 1.25). The chemical kinetic modeling was performed using CHEMKIN-II while using the Konnov0.6 [39] and GDFkin3.0 of El Bakali et al. [22] prompt NO_x mechanisms. These detailed mechanisms were the only ones that implemented NCN at the time. While introduction of $C_2O + N_2 \iff NCN + CO$ reaction does not modify the predictions in the methane flame, an improvement is found in the predictions for the acetylene flames due to the significant C_2O concentration in those flames.

In this dissertation, the most recently published prompt NO_x mechanism in the literature is also studied. This mechanism is produced by Glarborg et al. [31]. They argue that

$C_2O + N_2 \iff NCN + CO$ reaction has a prohibitively high barrier (as found by Zhu et al. [89]) and do not include this reaction in their mechanism. Instead, they argue that the reverse rates of the reactions of $CN + N \iff C + N_2$ and $NCN + M \iff C + N_2 + M$ are sufficiently fast enough to compete with the $CH + N_2 \iff NCN + H$ reaction. In this mechanism, the heat of formation of NCN as well as a few other species are updated. Most recent rates for reaction of NCN with H-atom are incorporated in this mechanism. Prompt NO_x reactions and kinetic constants of Glarborg et al. are provided in Table 4.6. The thermo-chemical data used for each nitrogen species in this mechanism are taken from Glarborg et al. thermo-chemical data file.

Eq #	Reaction	A	n	$E_A[cal/mol]$
1	$CH + N_2 \iff NCN + H$	5.3E+9	0.79	16,770
2	$CN + N \iff C + N_2$	5.9E+14	-0.4	0
3	$C_2 + N_2 \iff CN + CN$	1.5E+13	0.00	41,730
4	$NCN + M \iff C + N_2 + M$	8.9E+14	0.00	62,100
5	$NCN + H \iff HCN + N$	2.2E+11	0.71	5321
6	$NCN + H \iff HNC + N$	4.3E+-4	4.69	2434
7	$NCN + O \iff CN + NO$	2.5E+13	0.17	-34
8	$NCN + OH \iff HCN + NO$	2.6E+8	1.22	3593
9	$NCN + OH \iff NCO + NH$	1.7E+18	-1.83	4143
10	$NCN + O_2 \iff NO + NCO$	1.3E+12	0.00	23,167
11	$NCN + NO \iff CN + N_2O$	1.9E+12	0.00	6280
12	$HCN + M \iff HNC + M$	1.6E26	-3.230	54,900
13	$CN + H_2 \iff HCN + H$	1.1E05	2.600	51,908
14	$HCN + O \iff NCO + H$	1.4E04	2.640	4980
15	$HCN + O \iff NH + CO$	3.5E03	2.640	4980
16	$HCN + O \iff CN + OH$	4.2E10	0.400	20,665
17	$HCN + OH \iff CN + H_2O$	3.9E06	1.830	10,300
18	$HCN + OH \iff HOCN + H$	5.9E04	2.430	12,500
19	$HCN + OH \iff HNCO + H$	2.0E-03	4.000	1000
20	$HCN + OH \iff NH_2 + CO$	7.8E-04	4.000	4000
21	$HNC + H \iff HCN + H$	7.8E13	0.0	0
22	$HNC + O \iff NH + CO$	4.6E12	0.0	2200
23	$HNC + OH \iff HNCO + H$	3.6E12	0.0	-479
24	$CN + O_2 \iff NCO + O$	5.8E12	0.0	-417
25	$CN + O_2 \iff NO + CO$	1.4E12	0.0	-417
26	$NCO + H \iff NH + CO$	7.2E13	0.0	1000
26	$NCO + O \iff NO + CO$	2.0E125	-0.5	0

26	$NCO + O_2 \iff NO + CO_2$	2.0E12	0.0	20,000
26	$NCO + NO \iff N_2O + CO$	4.0E19	-2.19	1743
26	$NCO + NO \iff N_2 + CO_2$	1.5E21	-2.740	1824

Table 4.6: Prompt NO_x mechanism of Glarborg et al. [31]

4.3 CRN Model Development

In order to find the CRN model that would best represent the flow and chemistry inside the JSR, different configurations of reactors are investigated. Table 4.7 summarizes some of the possible configurations and the corresponding NO_x values for combustion of methane. At this stage, methane is chosen since the chemical kinetics of this fuel have been studied for over 50 years and many improvements have been made to its mechanism and thermo-chemical data. GRI3.0 is used as the hydrocarbon mechanism while NO_x is modeled using Klippenstein et al. H-N-O (Table 4.4) and Konnov (Table 4.5) prompt mechanisms. For reference, the experimental value of NO_x measured at 1800 K and fuel-air equivalence ratio of 0.7 is 10.4 ppm on a dry basis.

The first configuration in Table 4.7 uses a single PST to model the JSR. In this case, NO_x is over predicted by about 50% due to high levels of free radical concentrations produced throughout the single PST. The single PST model was used previously by Vijlee [83] to predict NO_x and explain the trend seen experimentally for fuels such as iso-octane and toluene. Vijlee also found that a single PST over-predicted the magnitude of NO_x. However, the correct trend of NO_x was observed between iso-octane and toluene.

The second configuration utilizes a PSB followed by a PST. The volume of the PST is the volume of the JSR, with subtraction of the PSB volume. In this scenario, the predictions matches the experimental value of NO_x emission. This simple model can be used to predict NO_x by using the PSB to predict the regions of primary flame and the PST to predict the recirculating near-post-flame zone that dominates most of the JSR volume. However, it does not consider the degree of entrainment of the post-flame gases into the primary flame and

jet of the reactor. This entrainment is called recycle.

The third configuration in Table 4.7 takes into account the recycling of hot gases from the PST to the fresh fuel and air burning in the PSB. The ratio between the gas recycling and the gas exiting the JSR was previously found by Fackler [24]. He used RANS CFD to find that 25% of gases exit the JSR and 75% recycle in the reactor – that is, are entrained into the jet. This ratio can also be found using analytical entrainment relations for a confined jet derived by Field et al [28]. The ratio of recycled mass flow rate ($\dot{m}_r$) over the incoming mass flow rate ($\dot{m}_\circ$) is found using Equation 4.2,

$$\frac{\dot{m}_r}{\dot{m}_\circ} = \frac{0.47}{\theta} - 0.5 \tag{4.2}$$

In this equation, θ is a parameter defined as:

$$\theta = \frac{d_\circ}{2L}(\frac{\rho_\circ}{\rho_a})^{1/2} \tag{4.3}$$

In this equation, $d_\circ$ is the nozzle diameter, $\rho_\circ$ is the density of the fluid at the nozzle, ρ_a is the density of surrounding fluid, and $2L$ is the duct diameter. Using these values for the JSR, $\frac{\dot{m}_r}{\dot{m}_\circ}$ is calculated to be around 3. This means that the recycled mass flow rate is three times higher than incoming mass flow rate. This is consistent with findings of Fackler, which suggests 75% of the fluid is recycled and is entrained into the jet while 25% exits the reactor.

Using these values, the predicted NO_x is about 30% higher than the experimental measurement. The recycled gas to the PSB increases the NO_x in the PSB while decreasing the pool of radicals (to the level of PST). The fluid entering the PST contains high levels of NO_x and because of the large residence time of the PST, NO_x in this reactor increases even more.

The next configurations add a PSR of 0.2 cc volume placed between the PSB and the PST. That is, the primary flame process is continued in the added PSR. The radical concentrations,

particularly O-atom and H-atom, increase in this reactor followed by near-post-flame reaction in the PST. In this case, NO_x goes up compared to case 2 due to higher levels of radicals produced in the PSR and made available to the PST.

Cases 5-8 explore configurations that include recycle into the PSB and the PSR. In Case 5, all of the hot recycled gas is sent to the PSR. The predicted NO_x is close to measurement, but the hot recycled gas does not participate in igniting incoming fuel and air. Cases 6 to 8 study different ratios of recycle to the PSB and the PSR. Recycling 5 or 10% of hot gases to the PSB produces the same level of NO_x. However, the radical concentration in the PSR is different. In case 7, the predicted O-atom in the PSR is closes to LES results for O-atom averaged over a residence time. As the ratio of fluid recycling to the PSB increases, NO_x also increases and the CRN over-predicts the NO_x emissions.

One may wonder if all fluid from the PSB enters the PSR before entering the PST. While this is complex to confirm using CFD, configuration 9 explores different ratios of fluid flowing from PSB to the PSR or the PST. CRN results show that the split does not make a significant difference in the predicted NO_x.

The effect of the PSR volume is shown in configuration 10. The volume of this reactor is increased from 0.5 cc to 2 cc. At 2 cc, the temperature of the PSR reaches the recirculation zone temperature of 1800 K. This variation has a minor effect on the magnitude of NO_x exiting the CRN.

The LES simulation in Section 3.3 shows pockets of gas with high radical concentrations that shed from the flame brush and enter the recirculation zone. This small region can be modeled using an adiabatic PSR with a small volume. LES suggests the volume of this region is about 0.1 cc, which is applied to PSR1. Configurations 11 and 12 explore this 4-zone CRN. NO_x produced using this CRN is very similar to the 3-zone CRN. The 3-zone CRN in configuration 7 is chosen for the CRN modeling in this dissertation. This is due to its well representation of the fluid and chemistry structure in the reactor as well as best prediction of NO_x for combustion of methane and other fuels. This CRN is used for all fuels and recirculation zone temperatures studied.

#	CRN Scheme	NO_x [ppm,dry]
1		15.7
2	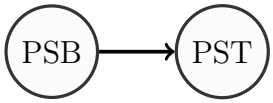	10.3
3	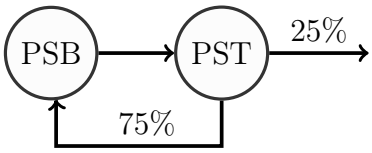	13.2
4	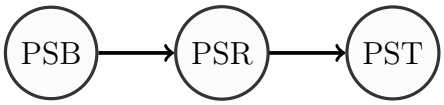	11.4
5	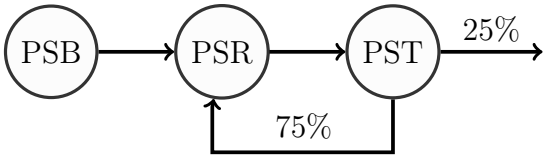	10.24
6	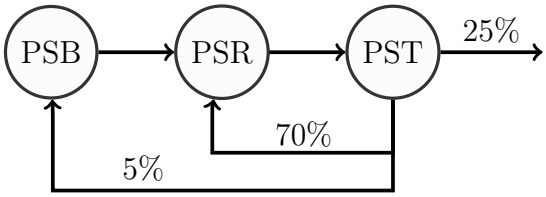	10.86
7	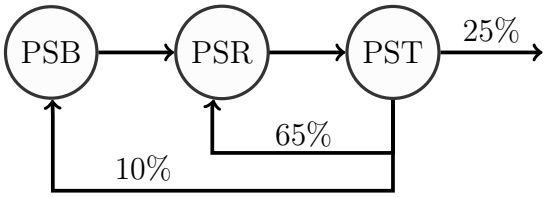	10.86
8	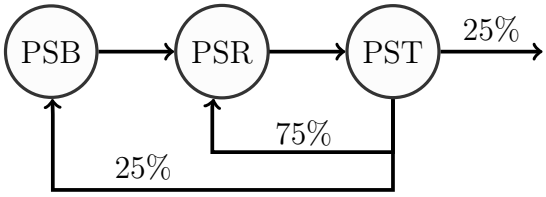	12.1
9	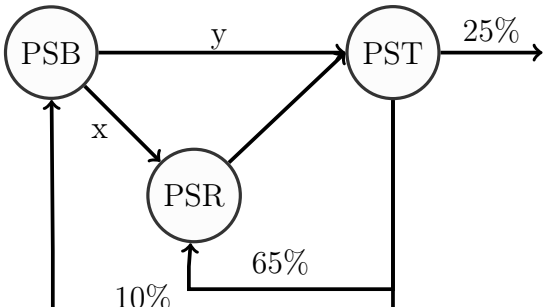	(x:y=20%:80%): 10.86 (x:y=50%:50%): 10.81

(x:y=80%:20%): 10.72

10

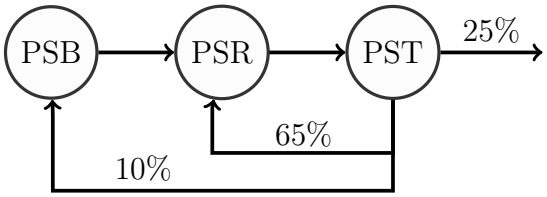

(V_{PSR}=0.5cc): 10.871

(V_{PSR}=1cc): 10.58

(V_{PSR}=2cc): 10.0

11

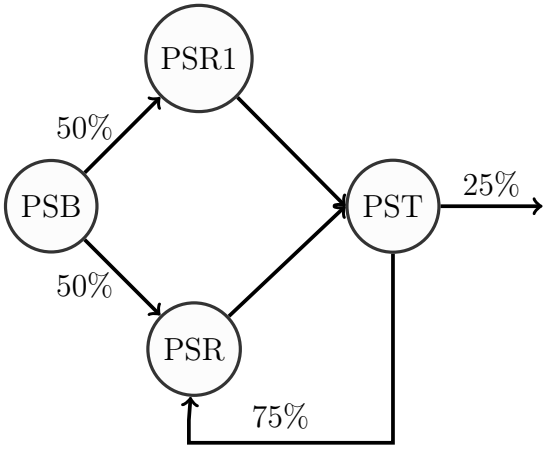

10.1

12

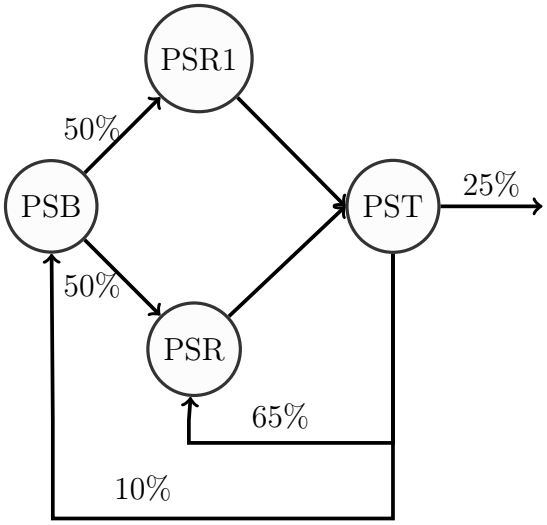

10.2

Table 4.7: Various CRN configurations are analyzed to find the best model that represents the flow and chemistry inside the JSR best. All CRN models treat the combustion of methane at fuel-equivalence ratio of 0.7 and recirculation zone temperature of 1800 K. GRI3.0 hydrocarbon mechanism is used in addition to Klippenstein H-N-O and Konnov prompt NO_x mechanisms. For reference, the experimental value of NO_x measured at 1800K is 10.4 ppm on a dry basis. The PSR volumes are 0.2 cc unless stated. PSR1 and PSR volumes are 0.1 and 0.2 cc, respectively.

4.4 Model Setup

Once the chemical kinetic mechanism and thermo-chemical files are imported in CHEMKIN-Pro, the three-zone CRN is created using configuration 7. A sample diagram of the CRN in CHEMKIN-Pro is shown in Appendix D.1. Note that the splitter is used to recycle the flow from PST to PSB and PSR.

The total mass flow rate of fuel and air is set to 1.1 g/s and unburned pre-mixed gas temperature is 605 K. All reactors are set to a pressure of 1 atm. The fuel-air equivalence ratio of each fuel is set to its corresponding experimentally averaged value. Table 4.8 displays the fuel-air equivalence ratio as well as blowout volume, V_{BO}, for each fuel at three different recirculation zone temperatures. The blowout volumes are found by varying the volume of the PSB to find the smallest volume in which combustion can be sustained. These blowout volumes are reported for individual pure hydrocarbon fuels and surrogate jet fuel mechanisms. Note that addition of the NO_x mechanisms do not affect the V_{BO} since the low amounts of NO_x formed in the JSR do not affect the blowout volumes..

Mechanism	Fuel	ϕ			V_{BO} $[cm^3]$		
		1700 K	1800 K	1900 K	1700 K	1800 K	1900 K
Individual	Methane	N/A	0.692	N/A	N/A	0.42	N/A
	Iso-octane	0.613	0.672	0.744	0.51	0.38	0.28
	N-octane	0.605	0.670	0.741	0.58	0.34	0.27
	N-dodecane	0.59	0.66	0.72	0.52	0.36	0.28
	Toluene	0.598	0.668	0.729	1.00	0.70	0.53
	135-TMB	0.607	0.659	0.729	0.86	0.76	0.42
Dooley et al.	Methane	N/A	0.692	N/A	N/A	0.50	N/A
	Iso-octane	0.613	0.672	0.744	0.59	0.42	0.33
	N-octane	0.605	0.670	0.741	0.65	0.46	0.35
	Toluene	0.598	0.668	0.729	0.98	0.68	0.53

Table 4.8: Summary of fuel-air equivalence ratio and blowout volume (V_{BO}) for each fuel at three recirculation zone temperatures of 1700K, 1800K, and 1900K. The temperatures correspond to the measured temperatures. These values are provided for the individual pure hydrocarbon fuel and the surrogate jet fuel mechanisms.

4.5 Results

In this section, the 3-zone CRN model is used to predict NO_x using the mechanisms listed in Table 4.2. Two different prompt NO_x mechanisms of Konnov [39] or Glarborg et al. [31] are used along with the H-N-O NO_x mechanism of Klippenstein et al. [38]. Additionally, the surrogate jet fuel mechanism of Dooley et al. is used with the NO_x mechanisms stated above and compared with the individual mechanisms.

4.5.1 Individual Mechanisms

Individual hydrocarbon mechanisms are used with the Klippenstein et al. [38] H-N-O and Konnov [39] prompt NO_x mechanisms. Figure 4.1 shows the comparison between experi-

mental values of NO_x and CRN predictions at the recirculation zone temperature of 1800 K.

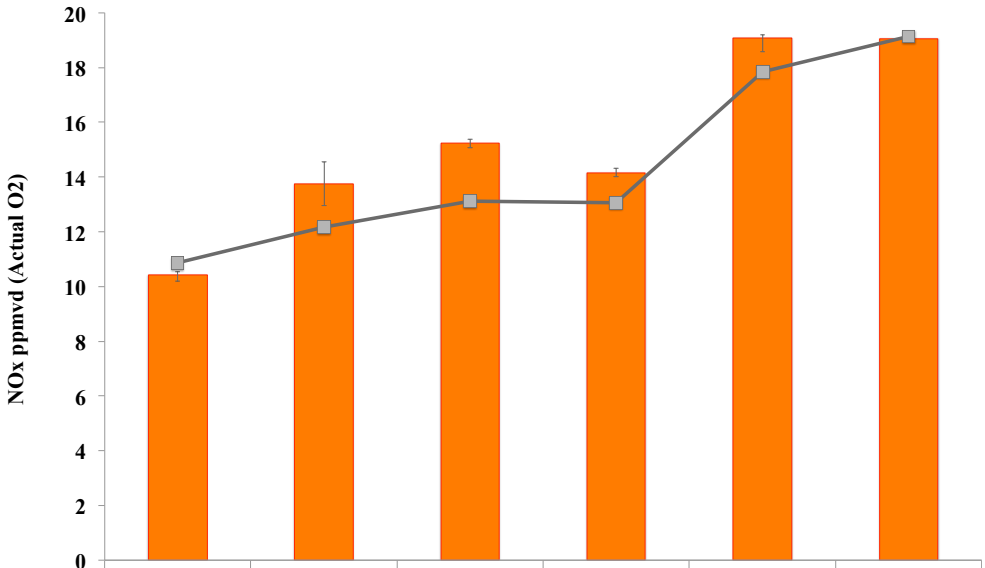

	Methane	iso-Octane	n-Octane	n-Dodecane	135-TMB	Toluene
Experiments	10.4	13.8	15.2	14.2	19.1	19.1
CRN-Individual Hydrocarbon Mechanisms-Klippenstein et al. and Konnov NOx Mechanisms	10.9	12.2	13.1	13.1	17.8	19.1

Figure 4.1: Comparison between NO_x values measured and predicted with the 3-zone CRN using individual hydrocarbon mechanisms, H-N-O NO_x mechanism of Klippenstein et al. [38], and Konnov [39] prompt NO_x mechanism. These values correspond to the recirculation zone temperature of 1800K.

This figure shows a good agreement between the experimental results and the CRN modeling using the three-zone configuration (case 7) in Table 4.7. NO_x is under-predicted by about 13 % for liquid alkanes and 6 % for 135-TMB. NO_x it is well-predicted for methane and toluene and CRN values are within experimental error bars.

The trend observed in the CRN modeling is examined by analyzing the contribution of each CRN zone. Figure 4.2 shows the NO_x rate of production (ROP) in each zone of the CRN for all fuels. These values are reported in CHEMKIN-PRO in units of $mole/cm^3 - s$. However, in this figure, each value is multiplied by the volume of each reactor to show it in units of $mole/s$ for each zone

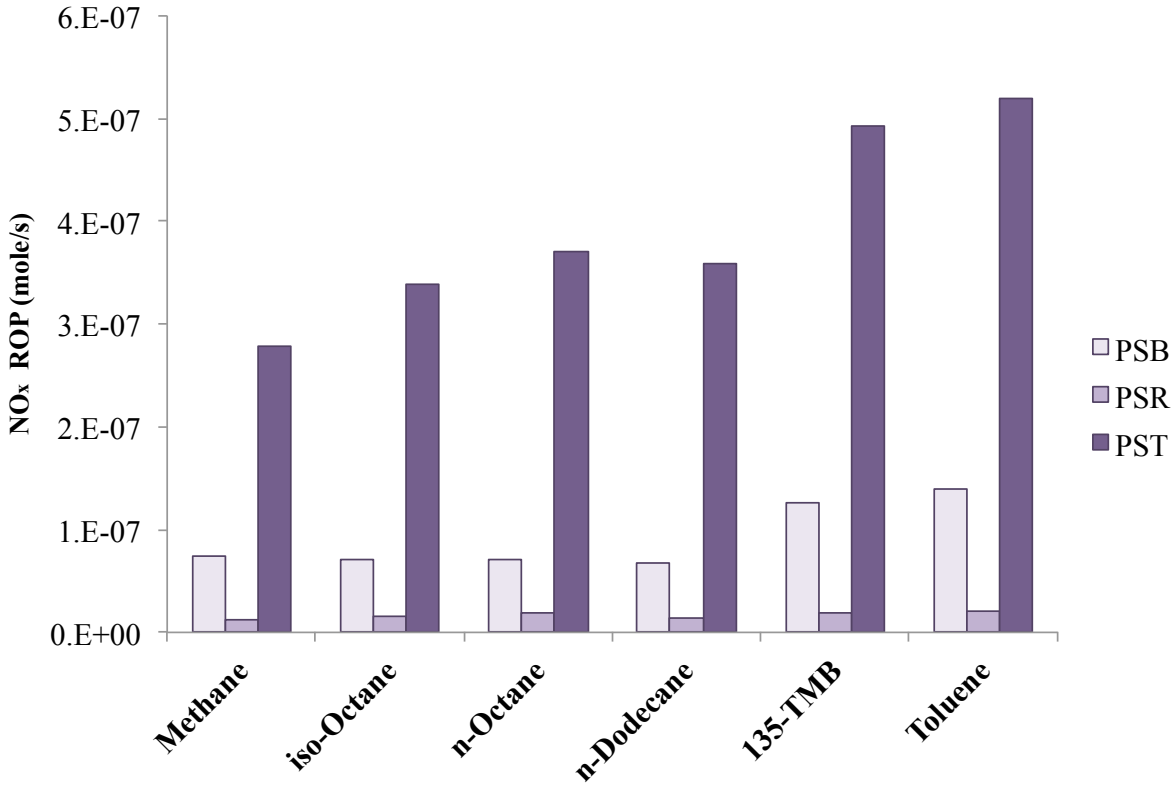

Figure 4.2: NO_x ROP in the PSB, PSR, and PST of the CRN for all fuels modeled at recirculation zone temperature of 1800 K. These results use individual mechanisms for hydrocarbons, H-N-O NO_x mechanism of Klippenstein et al. [38], and Konnov [39] prompt NO_x mechanism.

This figure shows that the rate of production of NO_x is highest in the PST for all fuels. The rest of the NO_x is formed in the PSB and PSR. PSR does not play a significant role in NO_x production. Figure 4.2 also shows that aromatic fuels produce more NO_x in the PSB compared to the aliphatic fuels. This is caused by the larger volume required to sustain combustion of the aromatic fuels in the PSB for these fuels. Differences in the prompt NO_x kinetics for the aromatic fuels may be a second cause.This will be further studied later in this chapter.

Since most of the NO_x is formed in the PST, it is important to study the reactions that produce/destroy NO_x in this reactor. Figure 4.3 shows eleven reactions with the highest

rate of production (ROP) of NO_x for all fuels modeled.

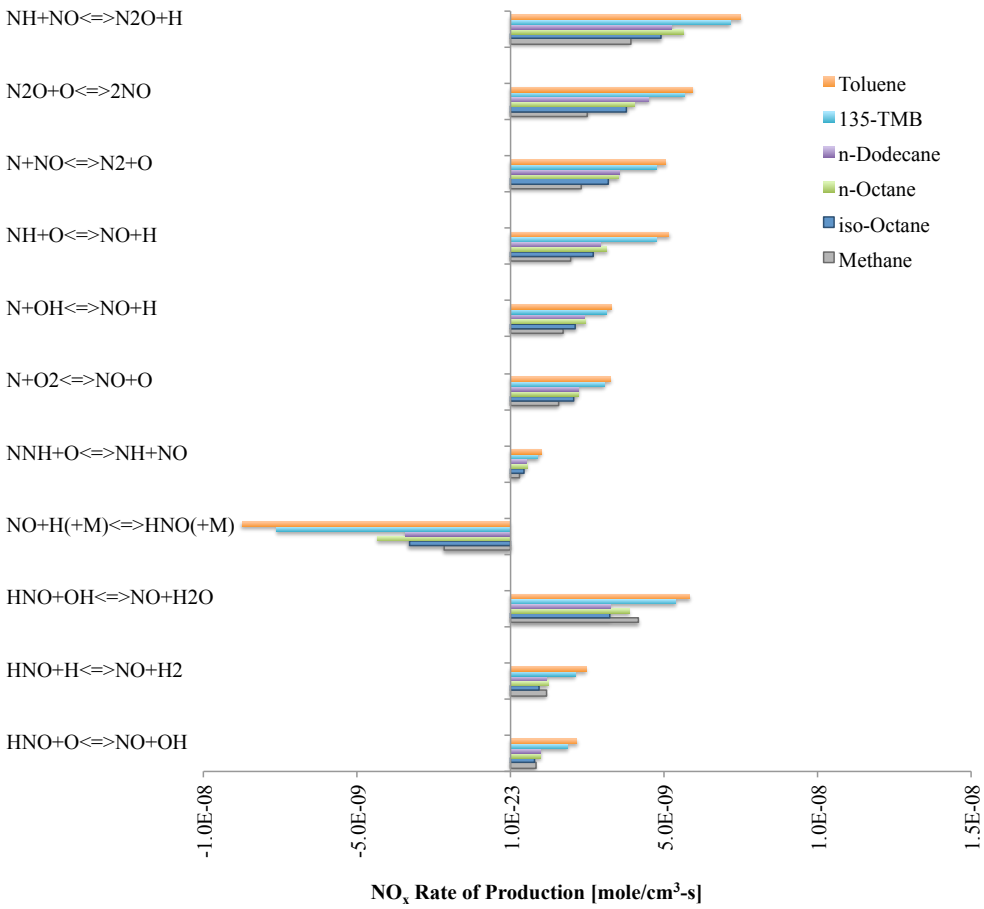

Figure 4.3: Rate of production of NO_x in the PST of the CRN model for all fuels. This analysis uses individual mechanisms for hydrocarbons, H-N-O NO_x mechanism of Klippenstein et al. [38], and Konnov [39] prompt NO_x mechanism.

Reactions involving NO_2 are not shown here since the sum of ROPs for these reactions is essentially zero and does not have a net effect on NO_x values in the PST. That is, NO is not affected and $NO2 \ll NO$. The last four reactions in this figure involve production/destruction of NO_x through HNO.The net effect of these reactions is small. The sum of all HNO ROP rates for methane is about $4E-9\ mol/cm^3-s$, while it is between 1.6 to 1.7 $E-9$ for the rest of the fuels.

The first six reactions in Figure 4.3 are arranged in order of highest ROP to lowest from top to bottom. The order of ROP is consistent among the six fuels modeled here. For each reaction, ROP of NO_x is similar to the trend of NO_x observed in Figure 4.1. These reactions suggest that N_2O and Zeldovich pathways contribute the most to NO_x production in the PST of all fuels.

In order to confirm this, the contribution of each NO_x mechanisms is determined. This is explored by eliminating the elementary reaction that starts the reaction system for producing NO_x in each pathway. As mentioned in Section 1.2, prompt, N_2O, Zeldovich, and NNH pathways are the NO_x mechanisms relevant to this work. Each of these mechanisms start by a radical reacting with N_2 molecules, generating a system of reactions that produce NO_x. By eliminating these starting reactions, the rest of the reactions that contribute to that mechanism are dismantled. This elimination is performed one at a time to gauge the contribution of each mechanism. Table 4.9 shows the starting reactions that are eliminated for this sensitivity analysis.

Mechanism	Reaction
Prompt	$CH + N_2 \iff NCN + H$
	$N_2 + C_2O \iff NCN + CO$
N_2O	$N_2 + O + (M) \iff N_2O + (M)$
Zeldovich	$N + NO \iff N_2 + O$
NNH	$N_2 + H \iff NNH$

Table 4.9: Starting reactions that are eliminated individually to find the contribution of each NO_x mechanism.

The overall contribution of each NO_x mechanism in the PST for each fuel is shown in Figure 4.4. The N_2O mechanism plays the most important role in NO_x formation for all fuels. The contribution of N_2O mechanism is about 40-50% of the overall NO_x produced

among fuels burnt. The Zeldovich and NNH mechanisms are more significant for aromatic fuels compared to aliphatic fuels, mainly because of the higher levels of radicals formed when burning aromatics fuels. The prompt mechanism has the highest effect on methane, contributing to 33% of the total NO_x produced.

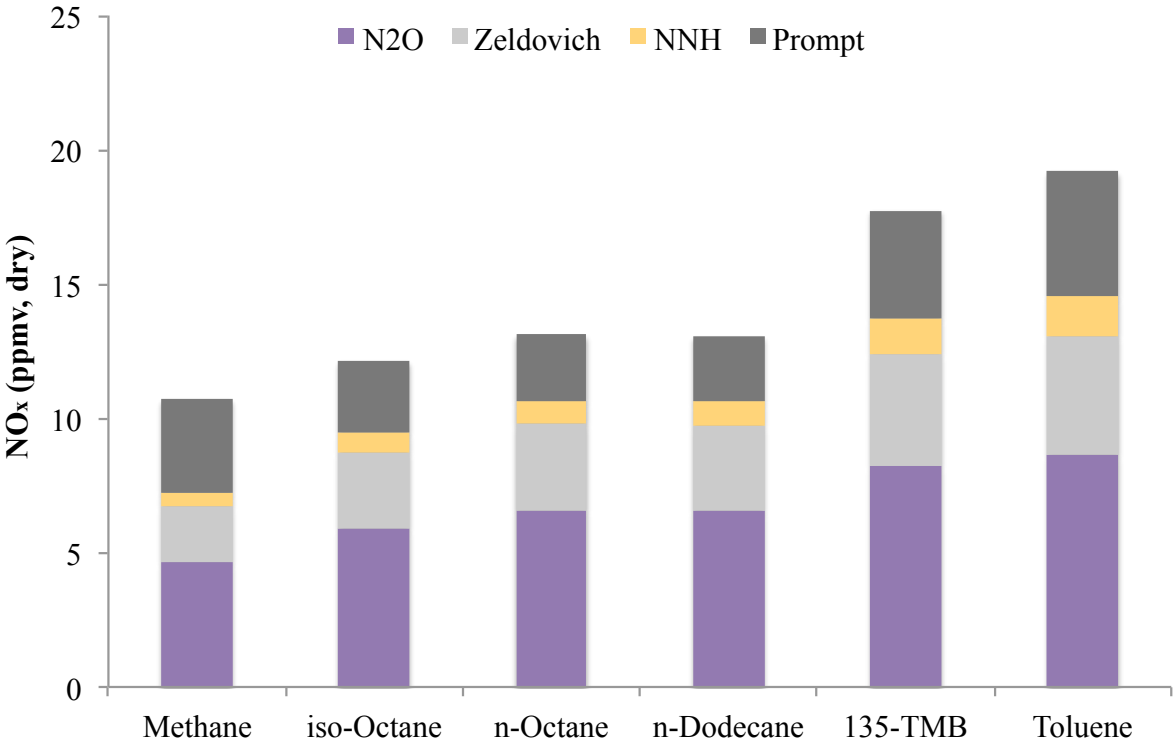

Figure 4.4: Analysis of NO_x emissions of all fuels modeled using the 3-zone CRN at the recirculation zone temperature of 1800K. This analysis shows the contribution of each NO_x mechanism to the overall NO_x emissions. Individual mechanisms for hydrocarbons, H-N-O NO_x mechanism of Klippenstein et al. [38], and Konnov [39] prompt NO_x mechanism are used for this modeling.

Both N_2O and Zeldovich mechanisms highly depend on the pool of radicals present. Concentrations of O-atom and H-atom in the PST for each fuel play an important role in the NO_x trends observed in Figure 4.4. These concentrations are presented in Figure 4.5. The O-atom concentration is lowest for methane and highest for aromatics, while liquid

alkane fuels produce similar concentrations. H-atom mole fraction is similar among all fuels, with being somewhat higher for aromatics.

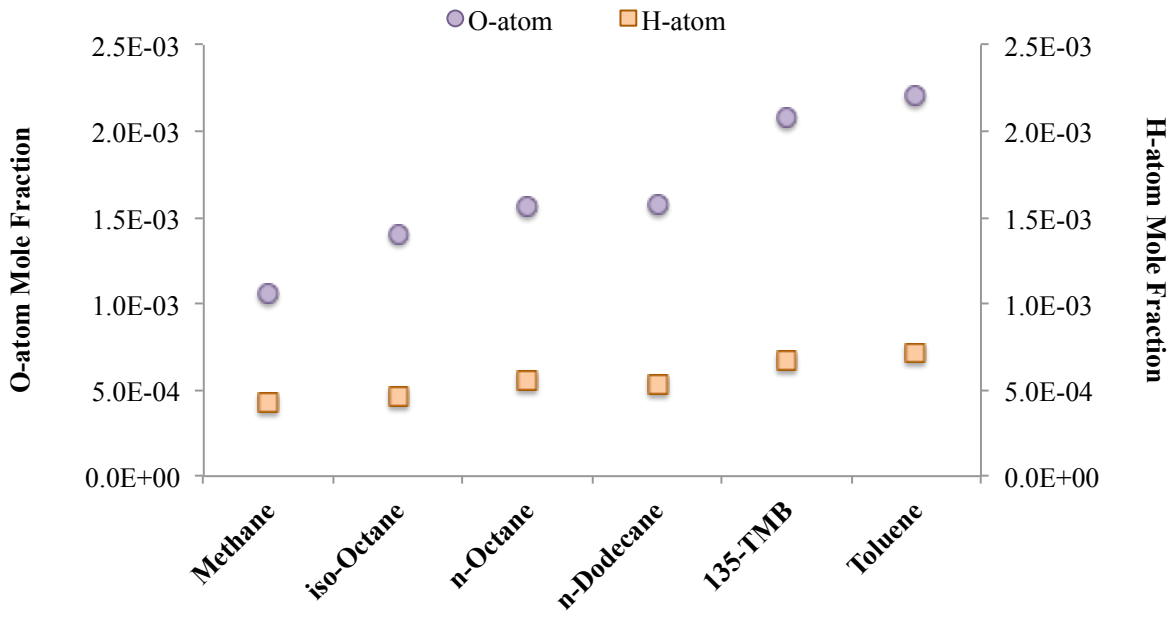

Figure 4.5: Mole fraction of O-atom and H-atom in the PST of the CRN model for all fuels. This analysis uses individual mechanisms for hydrocarbons, H-N-O NO_x mechanism of Klippenstein et al. [38], and Konnov [39] prompt NO_x mechanism.

The same analysis that is discussed in Figure 4.2 is performed for the PSB of the CRN to find the contribution of each NO_x mechanism. This is presented in Figure 4.6. This figure shows that aromatic fuels produce the most amount of NO_x in the PSB compared to aliphatic fuels. Additionally, prompt NO_x plays a significant role in the PSB. In fact, all of NO_x produced from the prompt route is formed in the PSB. The contribution of the rest of the mechanisms is due to the recycling of gases from the PST and PSR to the PSB. Further investigation of prompt NO_x trends is performed later in this chapter.

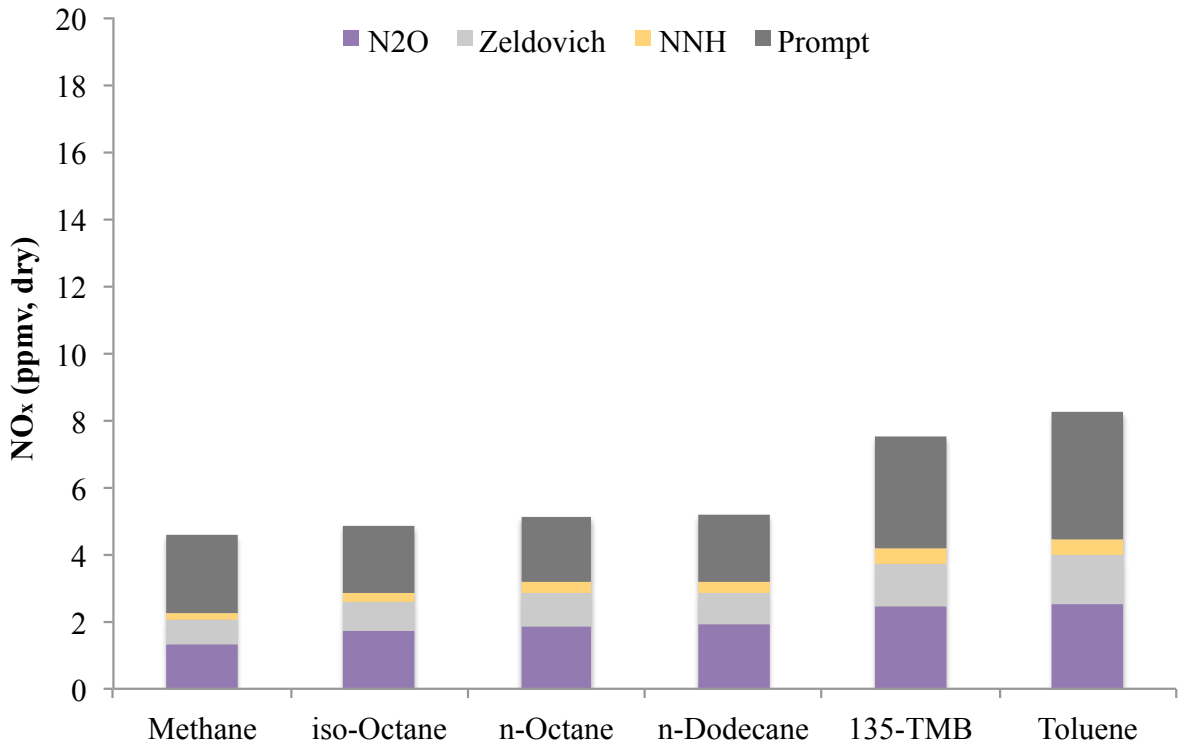

Figure 4.6: Sensitivity analysis for NO_x emissions of all fuels in the PSB of a 3-zone CRN at the recirculation zone temperature of 1800K. This analysis shows the contribution of each NO_x mechanism to the overall NO_x emissions. Individual mechanisms for hydrocarbons, H-N-O NO_x mechanism of Klippenstein et al. [38], and Konnov [39] prompt NO_x mechanism are used for this modeling.

4.5.2 Surrogate Jet Fuel Mechanism

A surrogate jet fuel mechanism by Dooley et al. is used to predict NO_x using the 3-zone CRN model. The main reason behind using a surrogate jet fuel mechanism is that several fuels are combined into one large mechanism, allowing many reactions to be shared by the fuels, including most importantly the chain-branching reactions involving O-atom and H-atom. From the findings of the previous section, we know that the concentrations of O and H-atom have a significant effect on NO_x production. By keeping the reactions that form these radicals the same, the effects of fuel variation can be studied better. The jet fuel

mechanism of Dooely et al. contains kinetics for methane, iso-octane, n-octane, and toluene. Therefore, these fuels are studied in this section. Figure 4.7 compares the NO_x predictions using individual mechanisms and Dooley et al. surrogate jet fuel mechanism to experiments.

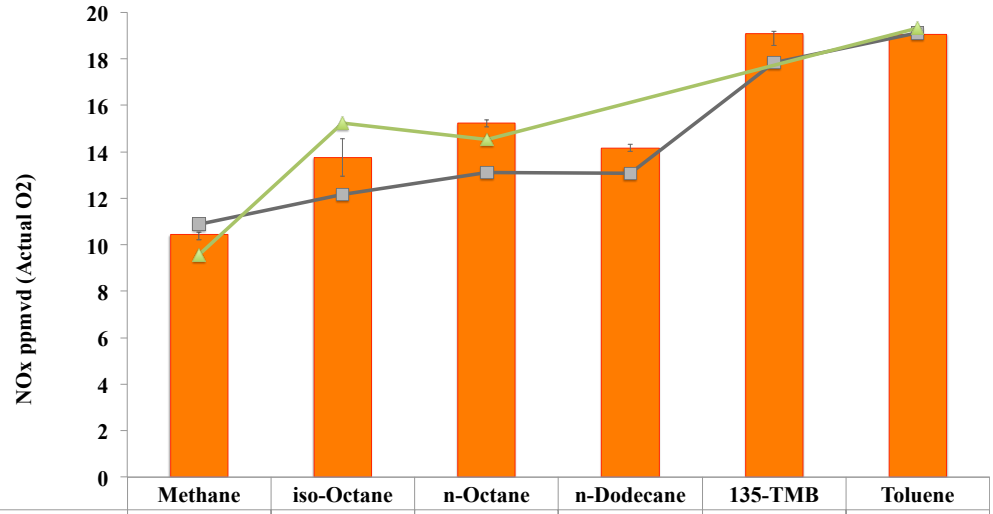

	Methane	iso-Octane	n-Octane	n-Dodecane	135-TMB	Toluene
Experiments	10.4	13.8	15.2	14.2	19.1	19.1
CRN-Individual Hydrocarbon Mechanisms-Klippenstein et al. and Konnov NOx Mechanisms	10.9	12.2	13.1	13.1	17.8	19.1
CRN-Surrogate Jet Fuel Mechanism-Klippenstein et al. and Konnov NOx Mechanisms	9.6	15.2	14.5			19.3

Figure 4.7: Comparison between NO_x values measured and predicted with the 3-zone CRN using Dooley et al. [20] surrogate jet fuel mechanism, H-N-O NO_x mechanism of Klippenstein et al. [38], and Konnov [39] prompt NO_x mechanism. These values correspond to the recirculation zone temperature of 1800K.

At 1800K, a good agreement between NO_x predictions using the Dooley et al. mechanism and experiments is observed. Although NO_x is over-predicted for isooctane and under-predicted for methane, CRN modeling using this mechanism appears to predict NO_x well for n-octane and toluene.

Similar to the results for the CRN modeling using individual mechanisms in the previous section, NO_x is mainly formed in the PST of the CRN when the surrogate jet fuel mechanism is used. The top eleven reactions that have the highest ROP of NO_x are shown in Figure 4.8.

For each reaction, ROP of NO_x is similar to the trend of NO_x observed in Figure 4.7. Additionally, these reactions are identical in this case compared to Figure 4.3 where individual hydrocarbon fuel mechanisms are used. Similarly, N_2O and Zeldovich NO_x mechanisms are the most important mechanisms here.

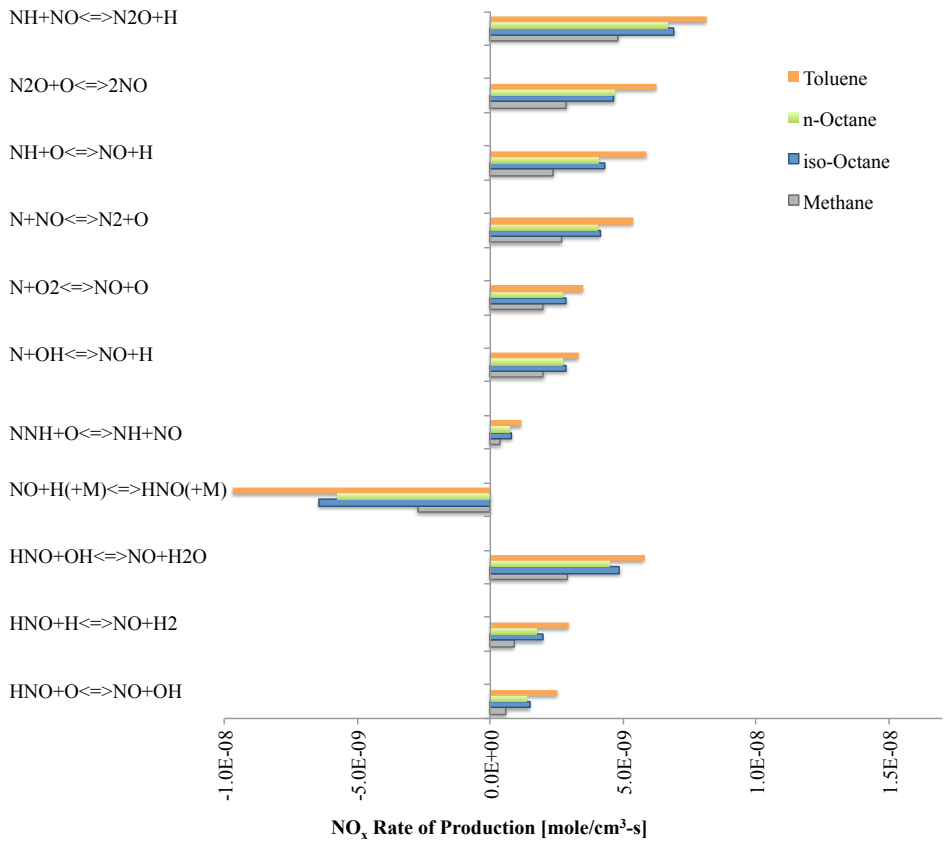

Figure 4.8: Rate of production of NO_x in the PST of the CRN model for all fuels. This analysis uses Dooley et al. [20] surrogate jet fuel mechanism, H-N-O NO_x mechanism of Klippenstein et al. [38], and Konnov [39] prompt NO_x mechanism. These values correspond to the recirculation zone temperature of 1800K.

As stated in the previous section, the N_2O and Zeldovich mechanisms are dependent on O and H-atom concentrations. Figure 4.9 shows that O and H-atom concentrations in the PST are highest for toluene. Iso-octane has a higher concentration of these radicals compared to n-Octane and methane. The trend seen in the concentration of these radicals follows the

trend seen in NO_x emissions among all the fuels.

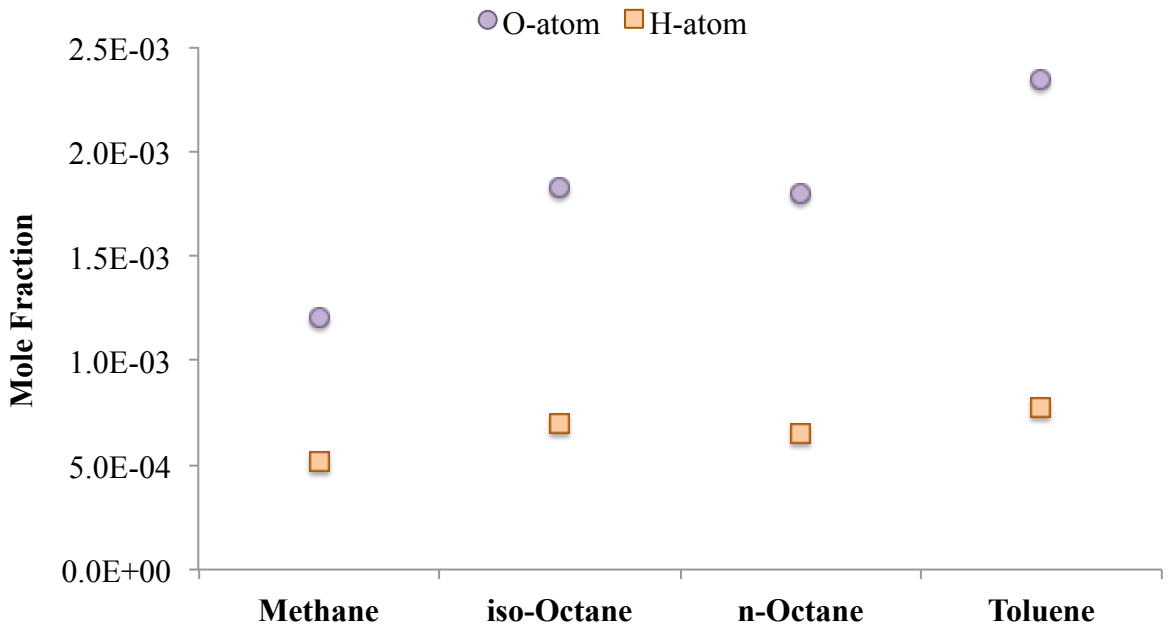

Figure 4.9: Mole fraction of O-atom and H-atom in the PST of the CRN model for all fuels. This analysis uses Dooley et al. [20] surrogate jet fuel mechanism, H-N-O NO_x mechanism of Klippenstein et al. [38], and Konnov [39] prompt NO_x mechanism. These values correspond to the recirculation zone temperature of 1800K.

4.5.3 Effects of Recirculation Zone Temperature

In order to see the agreement between the CRN model and experiments over a range of temperatures, the 3-zone CRN is used at recirculation zone temperatures of 1700 and 1900K as well as 1800K shown above. Figures 4.10 and 4.11 show the comparison among CRN predictions using the individual pure hydrocarbon fuel mechanisms, surrogate jet mechanism, and experiments for recirculation zone temperature of 1700 and 1900 K, respectively. All fuels except methane are studied at 1700 and 1900K.

The modeling with the individual mechanisms shows close agreement to the measured NO_x for 1700K (Figure 4.10), and about a 10% smaller prediction of NO_x than measured at

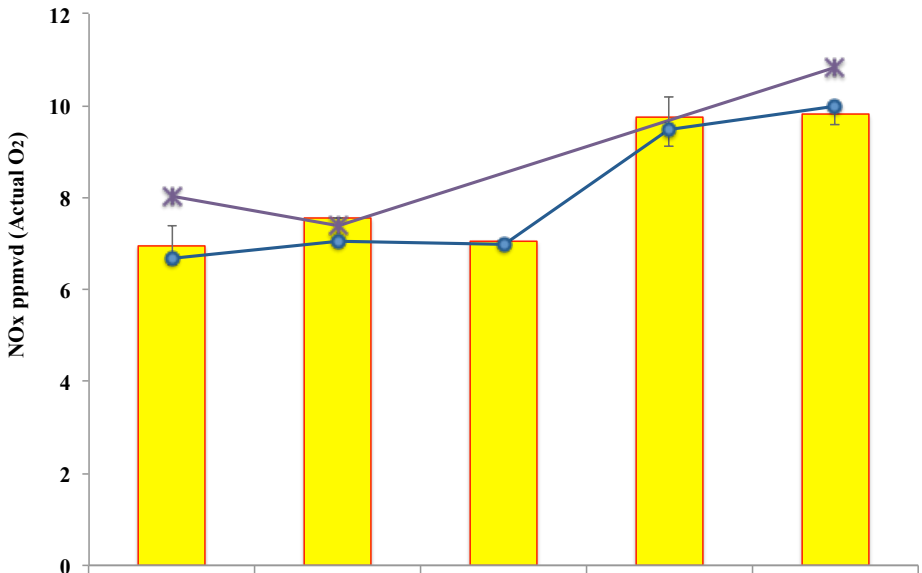

	iso-Octane	n-Octane	n-Dodecane	135-TMB	Toluene
Experiments	7.0	7.6	7.1	9.8	9.8
CRN-Surrogate Jet Fuel Mechanism-Klippenstein et al. and Konnov et al. NOx Mechanisms	8.0	7.4			10.8
CRN-Individual Hydrocarbon Mechanisms-Klippenstein et al. and Konnov NOx Mechanisms	6.7	7.0	7.0	9.5	10.0

Figure 4.10: Comparison between NO_x values measured and predicted with the 3-zone CRN using both Dooley et al. [20] surrogate jet fuel mechanism and individual mechanisms. NO_x is modeled using H-N-O mechanism of Klippenstein et al. [38], and Konnov [39] prompt NO_x mechanism. These values correspond to the recirculation zone temperature of 1700K.

1900K (Figure 4.11), except for a small over-prediction for toluene. For both temperatures, the Dooley et al. mechanism tends to over-predict the measured NO_x, by about 10% on average. In all cases, Dooley et al. mechanism predicts higher levels of O-atom compared to the individual mechanisms. Nevertheless, this surrogate jet fuel mechanism confirms that O and H-atom concentrations are higher for aromatics compared to aliphatic fuels. These results are not plotted here.

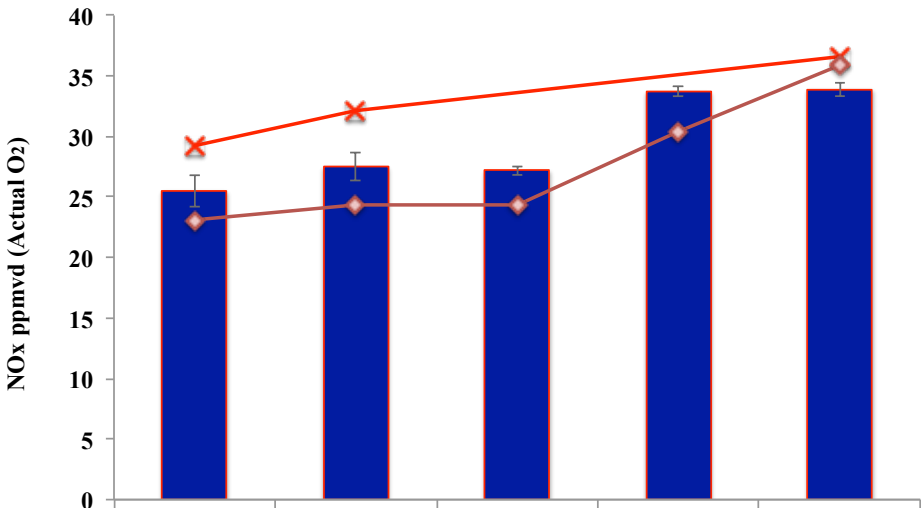

	iso-Octane	n-Octane	n-Dodecane	135-TMB	Toluene
Experiments	25.5	27.5	27.2	33.6	33.9
CRN-Surrogate Jet Fuel Mechanism-Klippenstein et al. and Konnov et al. NOx Mechanisms	29.2	32.1			37
CRN-Individual Hydrocarbon Mechanisms-Klippenstein et al. and Konnov NOx Mechanisms	23.1	24.4	24.4	30.4	35.9

Figure 4.11: Comparison between NO_x values measured and predicted with the 3-zone CRN using both Dooley et al. [20] surrogate jet fuel mechanism and individual mechanisms. NO_x is modeled using H-N-O mechanism of Klippenstein et al. [38], and Konnov [39] prompt NO_x mechanism. These values correspond to the recirculation zone temperature of 1900K.

4.5.4 Glarborg et al. Prompt Investigation

In this section, the Glarborg et al. prompt mechanism is compared to Konnov's prompt mechanism using the 3-zone CRN model. The H-O-N NO_x mechanism of Klippenstein et al. [38] and individual hydrocarbon mechanisms are used here and the only difference is prompt mechanisms. Figure 4.12 shows that NO_x is under-predicted for all fuels except methane using Glarborg et al. prompt chemistry. Methane is over-predicted by about 47%. When compared to the predictions using the Konnov prompt mechanism, there is not a big difference for iso-octane, n-octane, n-dodecane and 135-TMB.

The Glarborg et al. mechanism published in 2018 also includes the H-N-O NO_x chemistry.

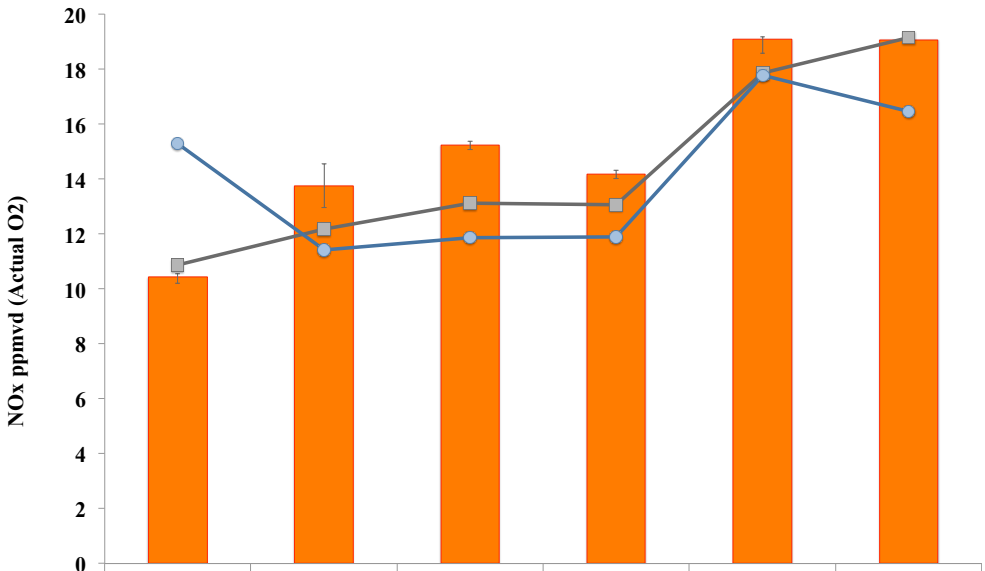

	Methane	iso-Octane	n-Octane	n-Dodecane	135-TMB	Toluene
Experiments	10.4	13.8	15.2	14.2	19.1	19.1
CRN-Individual Hydrocarbon Mechanisms-Klippenstein et al. and Konnov NOx Mechanisms	10.9	12.2	13.1	13.1	17.8	19.1
CRN-Individual Hydrocarbon Mechanisms-Klippenstein et al. and Glarborg et al. NOx Mechanisms	15.27	11.41	11.86	11.89	17.78	16.46

Figure 4.12: Comparison between NO_x values measured and predicted with the 3-zone CRN using individual hydrocarbon mechanisms, H-N-O NO_x mechanism of Klippenstein et al. [38], and two prompt mechanism of Konnov [39] and Glarborg et al. [31]. These values correspond to the recirculation zone temperature of 1800K.

This is called the "full NO_x mechanism" by Glarborg et al. It maintains the NNH chemistry of Klippenstein et al., but reduces the rate of NO_x formation from the N_2O mechanism. This full mechanism under-predicts NO_x significantly for liquid fuels. NO_x predictions for methane in this case matches experiments well, with under-prediction of only 3%. But, liquid fuels are under-predicted by about 40%. Figure 4.13 shows these results. This significant under-prediction is the reason the full NO_x mechanism by Glarborg et al. is not considered in this dissertation any further and only the prompt chemistry of Glarborg et al. is used.

As discussed in the previous section, essentially all of the NO_x produced from the prompt route is formed in the PSB zone of the CRN. Figure 4.14 compares the values of NO_x in the

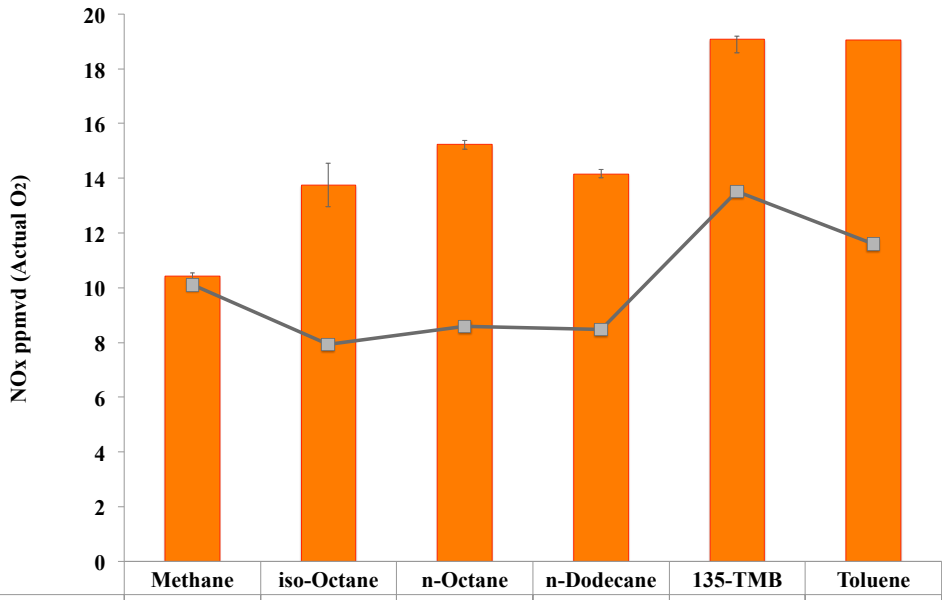

	Methane	iso-Octane	n-Octane	n-Dodecane	135-TMB	Toluene
Experiments	10.4	13.8	15.2	14.2	19.1	19.1
CRN-Individual Hydrocarbon Mechanism-Glarborg H-N-O and Prompt NOx Mechanism	10.1	7.9	8.6	8.5	13.5	11.6

Figure 4.13: Comparison between modeled and measured values of NO_x using individual hydrocarbon mechanisms and Glarborg et al. H-N-O and prompt NO_x mechanism. This plot is for recirculation zone temperature of 1800 K.

PSB of the 3-zone CRN model using the Konnov and Glarborg et al. prompt mechanisms. In this figure, NO_x predictions are lower for the liquid fuels using the Glarborg et al. prompt mechanism compared to Konnov, while the PSB-NOx is over-predicted for methane. The difference between the values of NO_x for each mechanism in Figure 4.14 is responsible for the overall NO difference between the Glarborg et al. and Konnov prompt mechanisms seen in Figure 4.12.

The trends in Figures 4.12 and 4.14 can be explained by investigating the important reactions and species responsible for NO production/destruction in the PSB. Sensitivity analysis for rate of production (ROP) of NO_x inside the PSB is shown in Figures 4.15 and 4.16 for toluene and methane, respectively.

Both of the figures show that $HNCN + O \Longleftrightarrow NO + HCN$ has the highest ROP for

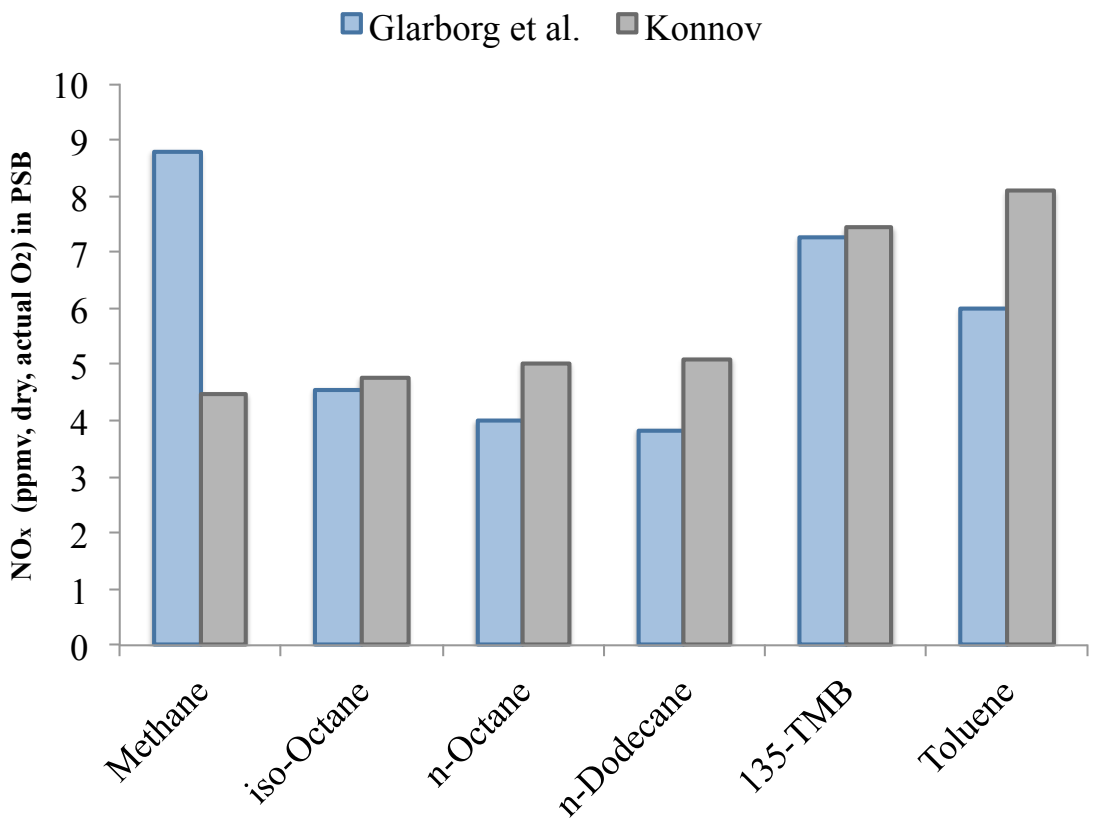

Figure 4.14: Comparison of NO_x values in the PSB component of the CRN between Konnov [39] and Glarborg et al. [31] prompt mechanisms. This analysis uses the individual hydrocarbon mechanisms and H-N-O NO_x mechanism of Klippenstein et al. [38].

Konnov prompt mechanism followed by $NCN + O \Longleftrightarrow CN + NO$. The Glarborg et al. prompt mechanism also forms NO_x through $NCN + O \Longleftrightarrow CN + NO$. But, this reaction is about an order magnitude larger for Glarborg et al. compared to Konnov in the case of methane combustion, and is responsible for the over-prediction of NO_x by the mechanism of Glarborg et al. for methane combustion. However, this reaction has about the same rate for toluene for both prompt mechanisms. Additional prompt pathways to NO_x that only exist in the Glarborg et al. mechanism are $NCO+O \Longleftrightarrow NO+CO$ and $CN+O_2 \Longleftrightarrow NO+CO$.

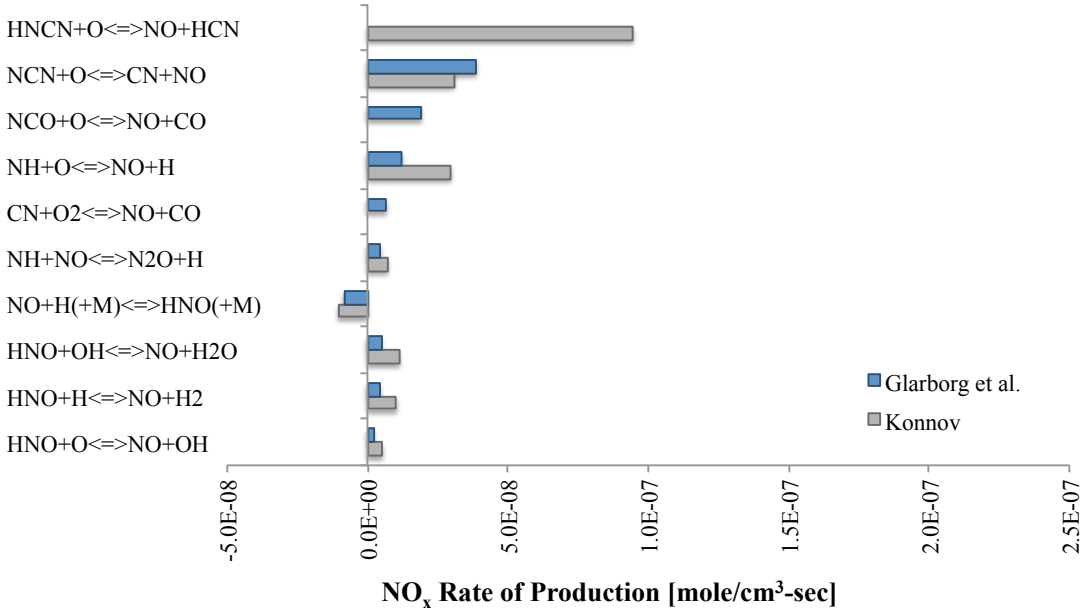

Figure 4.15: NO_x rate of production in the PSB of the 3-zone CRN using Yuan et al. [87] toluene mechanism and Klippenstein et al. H-N-O NO_x mechanism while comparing Konnov and Glarborg et al. prompt NO_x mechanisms.

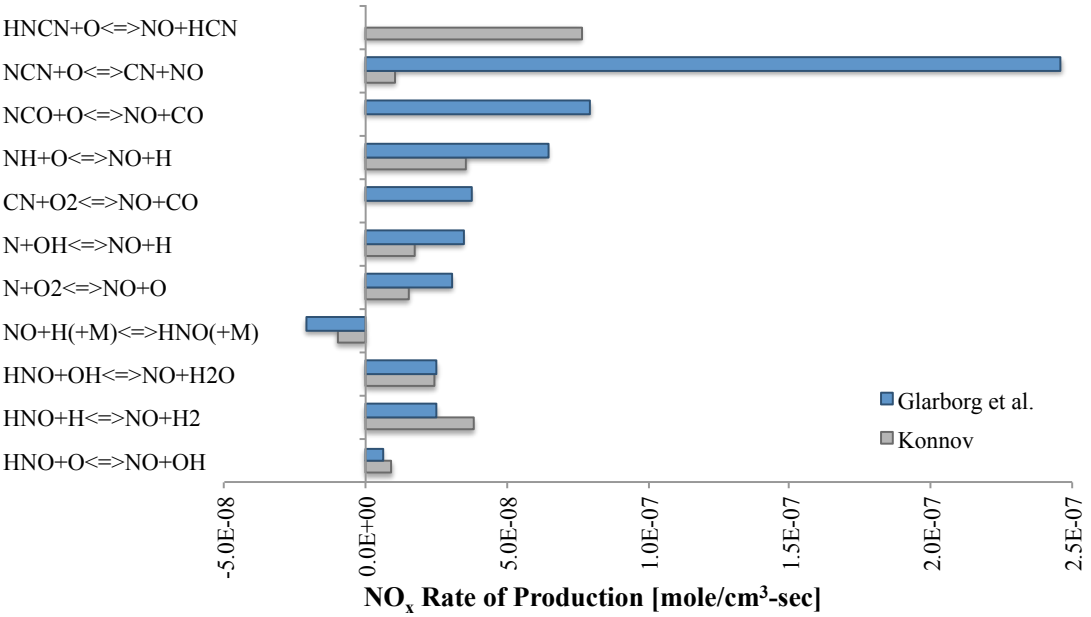

Figure 4.16: NO_x rate of production in the PSB of the 3-zone CRN using GRI3.0 mechanism for methane and Klippenstein et al. H-N-O NO_x mechanism while comparing Konnov and Glarborg et al. prompt NO_x mechanisms.

Reactions involving NO_2 are not shown in these figures since the sum of ROPs for these reactions is essentially zero and does not have a net effect on NO and NO_x values in the PSB. The last four reactions in these figures involve production/destruction of NO_x through HNO.The net effect of these reactions is more significant for CH_4 compared to toluene.

The are some differences between certain ROPs for reactions that belong to the O-H-N NO_x mechanism of Klippensiten et al. One would think that the ROP for these reactions would be the same since the hydrocarbon and O-H-N NO_x mechanisms are the same for a given fuel. However, some reactions in Konnov and Glarborg mechanism change the pool of N, NH, and other species which affect the ROP of reactions seen in Figures 4.15 and 4.16.

By examining the reactions in Figures 4.12 and 4.14 and performing sensitivity analysis for important species, pathways to NO_x formation are found. Figure 4.17 shows important prompt-species along with the pathways to NO_x formation for the two prompt mechanisms.

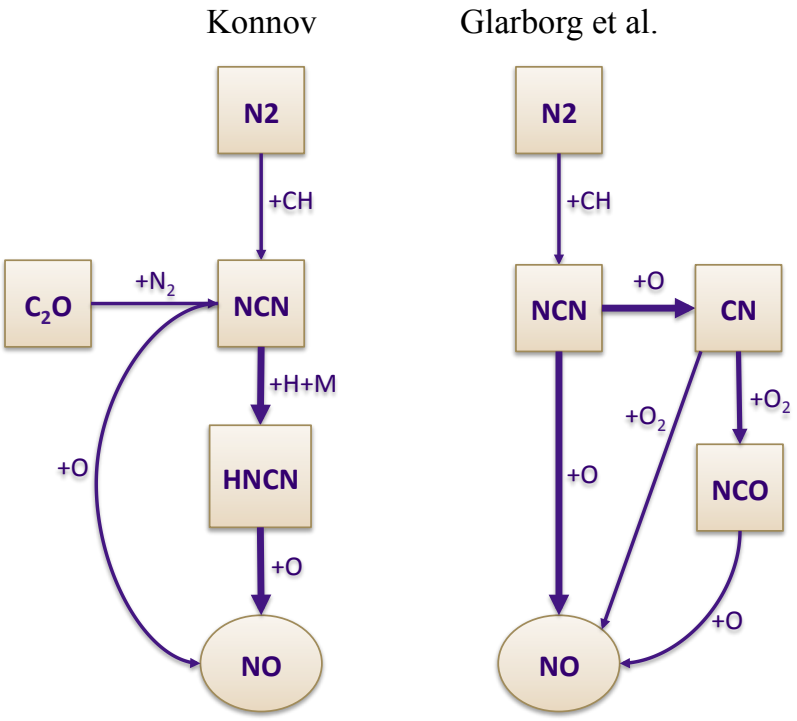

Figure 4.17: Prompt NO_x pathways for Konnov and Glarborg et al. prompt NO_x mechanism. These pathways hold for all fuels tested.

Using the Konnov prompt mechanism, the main reaction that produces NO_x is $HNCN + O \iff NO + HCN$. HNCN is produced through the reaction of NCN with H-atom and third-body species. NCN also directly forms NO_x by reacting with O-atom. In Glarborg et al. mechanism, NO_x is mainly formed through the reactions of $NCN + O \iff CN + NO$ and $NCO + O \iff NO + CO$. The CN radical is the only source of forming NCO while it also reacts with O_2 to form NO_x.

Figure 4.17 further shows that the only reaction that produces NCN is $CH + N_2 \iff NCN + H$ for the Glarborg et. al mechanism. On the other hand, Konnov includes an additional pathway involving the reaction of C_2O and N_2. This pathway plays a significant role in modeling NO_x for the liquid fuels, especially aromatics, whereas it does not show a role in modeling methane. This will be further explained later in this section.

Since NO_x in the PSB is directly or indirectly formed from NCN using both prompt mechanisms, it is important to study this radical further. Figure 4.19 shows the mole fraction of NCN in the PSB of the CRN for all fuels using the Konnov and Glarborg et al. prompt mechanisms. NCN mole fraction is about an order of magnitude higher for methane when the Glarborg et al. mechanism is used compared to Konnov. The overall ROP of NCN using the Glarborg et al. mechanism is $3.08E-9$ versus the $1.46E-10$ $mole/cm^3 - s$ of the Konnov prompt mechanism. For other fuels, NCN predicted by Konnov is slightly higher than Glarborg et al.

As shown in the prompt-NO_x pathway analysis in Figure 4.17, CH radical is the main source that produces NCN for both prompt NO_x mechanisms (in Konnov mechanism, C_2O also forms NCN). This reaction is $CH + N_2 \iff NCN + H$. The CH mole fractions in the PSB of all fuels are presented in Figure 4.19. These values are similar for both prompt mechanisms since CH mole fraction depends only on the hydrocarbon fuel mechanism and thermo-chemistry.

Figure 4.19 shows that the PSB contains about an order of magnitude higher CH radical for methane compared to other fuels. The ROP of NCN is higher in Glarborg et al. compared to Konnov mechanism. Unlike Glarborg et al. mechnaism, Konnov mechnism includes an

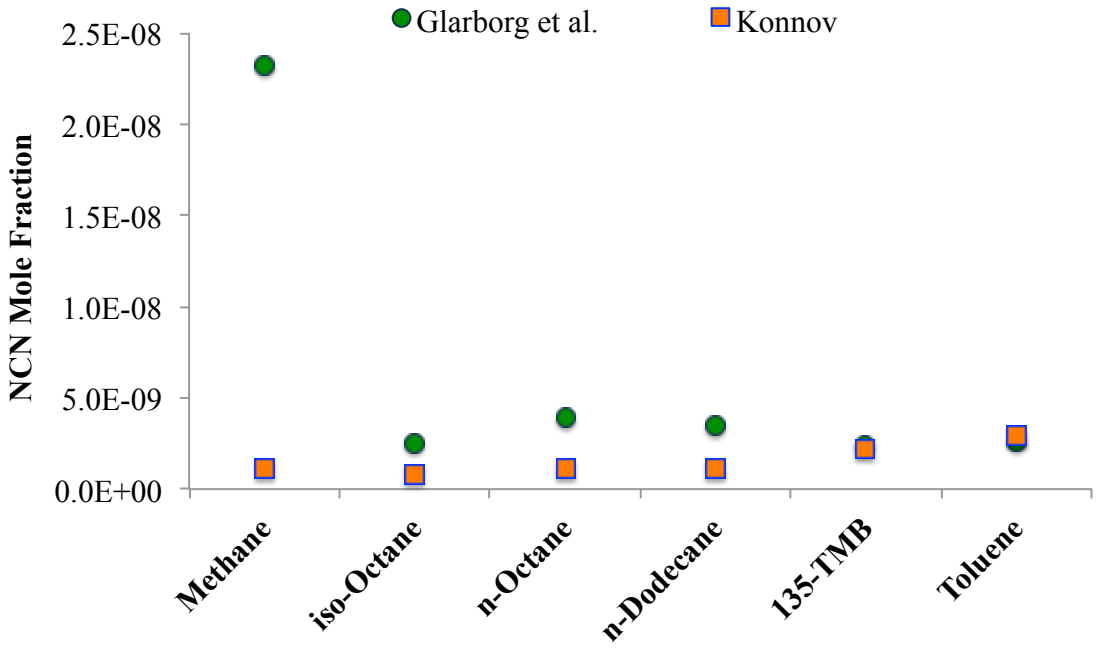

Figure 4.18: NCN mole fraction in the PSB of CRN, using individual hydrocarbon mechanisms, H-N-O NO_x mechanism of Klippenstein, and Konnov and Glarborg et al. prompt NO_x mechanisms.

additional pathway to NO as mentioned above. This is through the third body reaction of NCN with H to form HNCN which further reacts to NO. This reaction dominates NO formation using the Konnov prompt mechanism. With NCN mole fraction being about an order of magnitude higher using the Glarborg mechanism, this leads to over-prediction of NO_x for methane using this mechanism. It appears that the Glarborg et al. need to reduce their rate of $CH + N_2 \iff NCN + H$. Their rate for this reaction appears to be about a factor 3 larger than the Konnov rate for this reaction.

For all fuels except methane, $C_2O + N_2 \iff NCN + CO$ is an additional pathway to NCN formation when Konnov prompt mechanism is used. This is because methane produces smaller amounts of HCCO than the other fuels. The additional pathway to NCN for liquid fuels increases the concentration of this specie in the PSB. Lack of NCN for Glarborg et al.

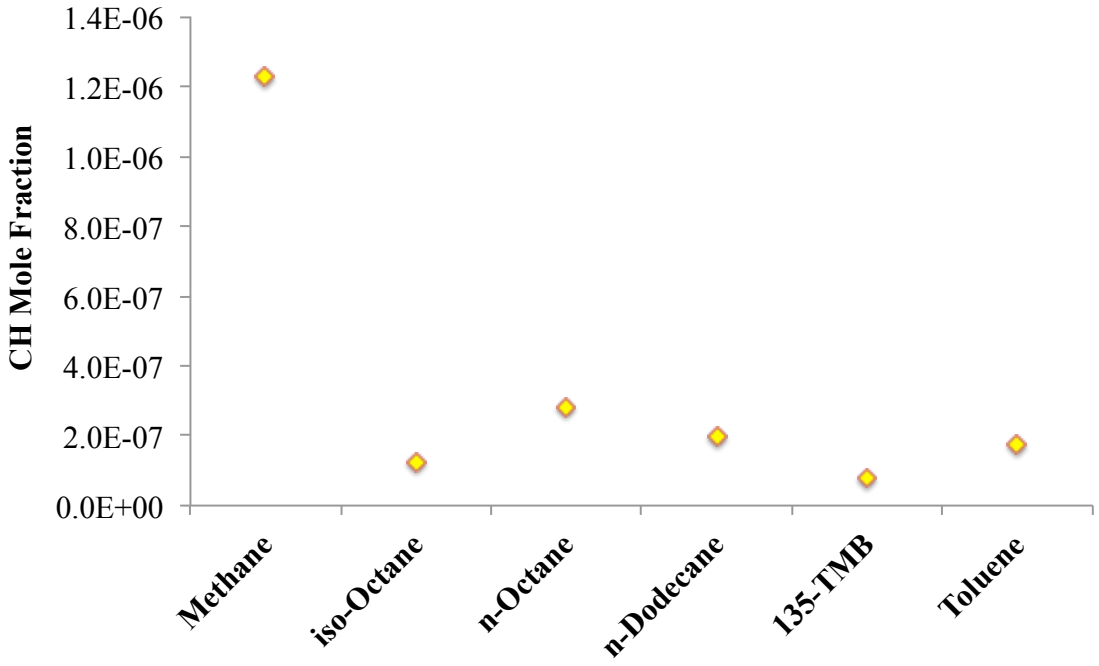

Figure 4.19: CH mole fraction in the PSB of CRN for methane, using Konnov and Glarborg et al. prompt NO_x mechanisms.

mechanism appears to be the reason for lower NO_x prediction in the PSB for combustion of liquid fuels compared to Konnov.

In order to further understand the routes that form CH in the PSB, an analysis on fuel breakdown is performed. Appendix D.2 shows the pathway to CH formation for all fuels. Figure D.2 shows the breakdown of methane to CH by losing an H-atom in a few stages. Other fuels show a different pattern with respect to CH formation as shown in Figure D.3 to D.7. Significant CH formed in the PSB originates from C_2H_2 for the fuels other than methane.

The main difference between aromatics and liquid aliphatic fuels is in the formation of C_2H_2. For n-alkanes and iso-octane, C_2H_2 is formed through breakdown of C_2H_4. However, C_2H_2 is formed directly from heavier molecules for aromatics.

Figure 4.20 shows the mole fractions of C_2H_2 and C_2H_4 in the PSB of the 3-zone CRN

using individual hydrocarbon mechanisms. The concentration C_2H_4 is significantly lower for aromatic fuels and methane compared to iso-octane and n-alkanes.

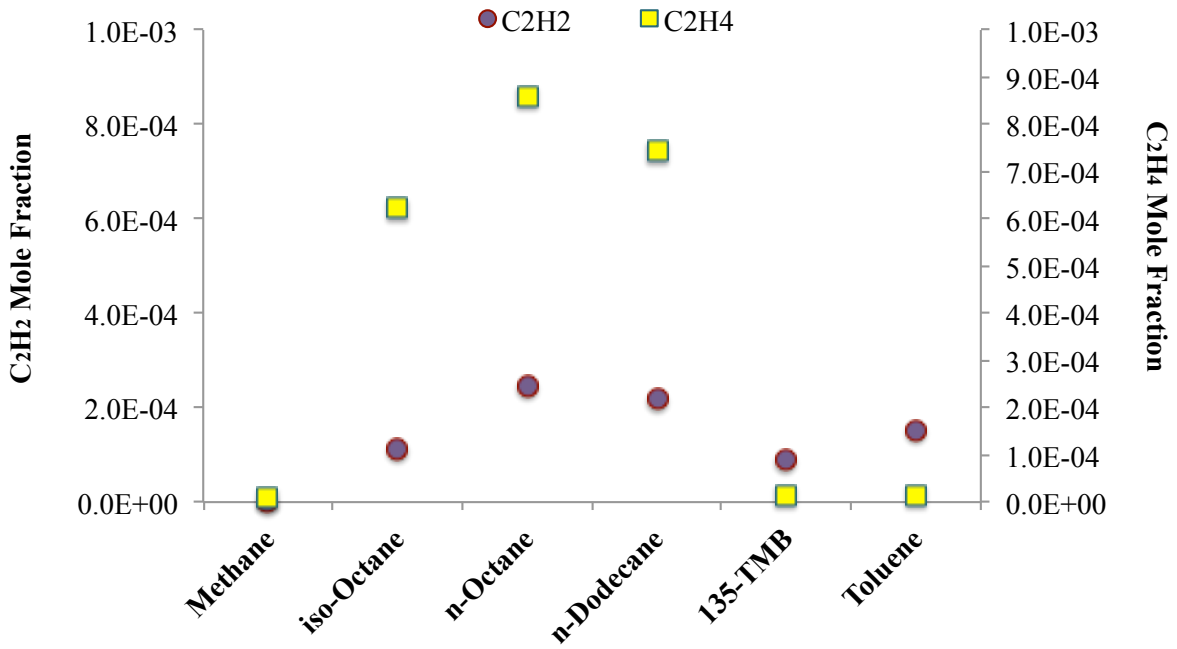

Figure 4.20: Mole fractions of C_2H_2 and C_2H_4 in the PSB of the 3-zone CRN using individual hydrocarbon mechanisms, H-N-O NO_x mechanism of Klippenstein et al. [38], and Konnov [39] prompt NO_x mechanism. These values correspond to the recirculation zone temperature of 1800K.

Figure D.2 to D.7 also provide an insight on CO formation pathways. For all liquid fuels, the main pathway for C_2H_2 breakdown is through reacting with O-atom to form HCCO. HCCO is the main pathway to CO formation in the PSB, where the highest mole fraction of CO exists in the CRN. The rest of the CO is formed from the CH route through reaction of O_2 with CH radical.

4.5.5 CO formation and its relation to NO_x

Figure 4.21 shows the comparison between CO measured and predicted using the 3-zone CRN. The CRN uses the individual hydrocarbon fuel mechanisms as well as the H-N-O

NO_x mechanism of Klipenstein et al. and Konnov prompt mechanism.

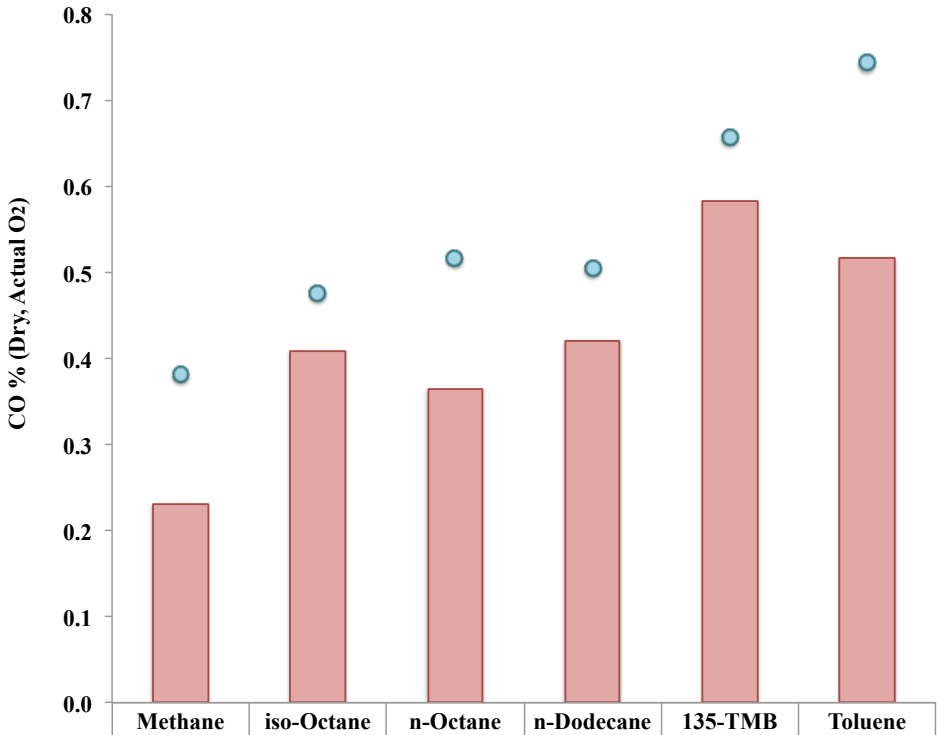

	Methane	iso-Octane	n-Octane	n-Dodecane	135-TMB	Toluene
Experiments	0.23	0.41	0.36	0.42	0.58	0.52
CRN-Individual Hydrocarbon Mechanisms-Klippenstein et al. and Konnov NOx Mechanisms	0.38	0.48	0.52	0.51	0.66	0.74

Figure 4.21: Comparison between CO measured and predicted using the 3-zone CRN. The CRN uses the individual hydrocarbon fuel mechanisms as well as H-N-O NO_x mechanism of Klipenstein et al. and Konnov prompt mechanism. These values correspond to the recirculation zone temperature of 1800 K.

Experimental and modeling values of CO show that aromatic fuels create more CO than aliphatic fuels. Methane produces the lowest concentration of CO. Measurements show lower values for CO mole fraction compared to experiments. This is due to oxidation of CO to CO_2 inside the sampling probe.

Figure 4.22 shows the mole fractions of CO and NO in the PST of the 3-zone CRN model for all fuels tested at recirculation zone temperature of 1800K. In this figure, CO and NO_x concentrations follow the same trend. These concentrations are highest for aromatics and

lowest for methane.

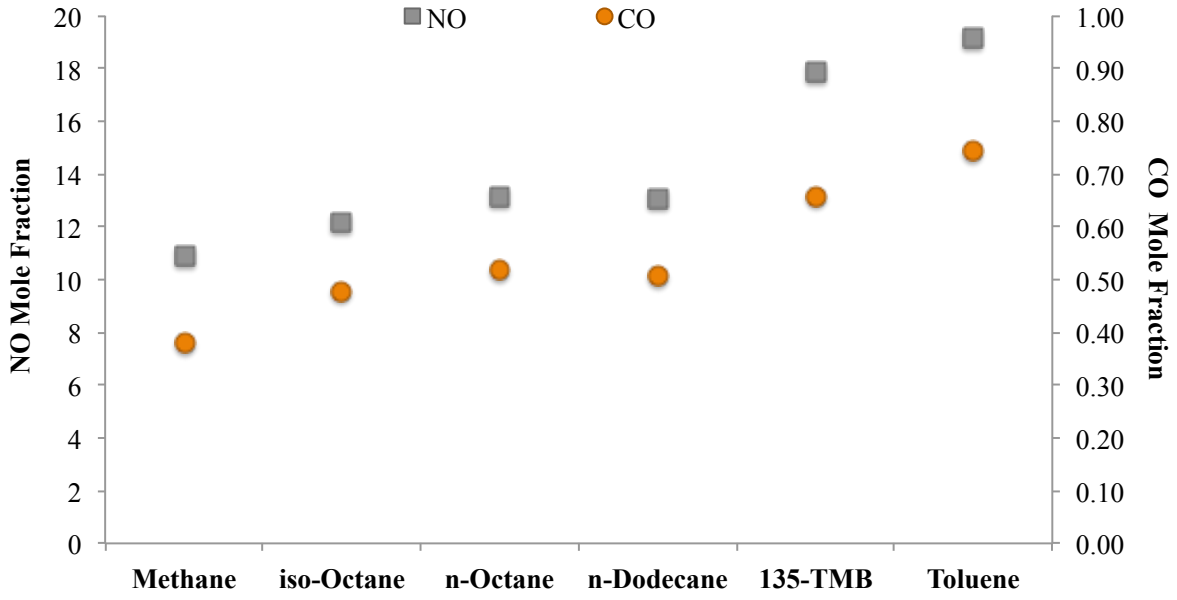

Figure 4.22: Mole fractions of NO and CO in the PST of the 3-zone CRN using individual hydrocarbon mechanisms, H-N-O NO_x mechanism of Klippenstein et al. [38], and Konnov [39] prompt NO_x mechanism. These values correspond to the recirculation zone temperature of 1800 K.

4.6 Summary of findings

In this chapter, a 3-zone CRN model is developed and implemented to model the flame zones inside the JSR. The goal of this work is to predict emissions and explain the experimental trends observed for combustion of fuels such as methane, iso-octane, n-octane, n-dodecane, 135-TMB, and toluene. Two sets of hydrocarbon mechanisms are utilized in the CRN model, the individual fuel hydrocarbon mechanisms and a surrogate jet fuel mechanism. NO_x is modeled using the 2011 Klippenstein et al. H-N-O mechanism as well as two different prompt mechanisms of Konnov and Glarborg et al. published in 2000 and 2018, respectively. The following findings are observed by analyzing the results of the CRN modeling.

1. NO_x is predicted well when the individual fuel hydrocarbon mechanisms or the surrogate jet fuel mechanism are used with Klippenstein et al. H-N-O and Konnov prompt NO_x mechanisms. These emissions are slightly under-predicted for n-alkanes and iso-octane. These results are consistent among three different recirculation zone temperatures of 1700, 1800, and 1900 K.

2. Sensitivity analysis on NO_x pathways shows that N_2O is the major pathway to NO_x formation in the JSR at the recirculation zone temperature of 1800K. Zeldovich route is the second most important route followed by the prompt mechanism. NNH route has a small contribution to overall NO_x for these fuels burned lean-premixed.

3. Compared to the Konnov mechanism, the Glarborg et al. prompt mechanism under-predicts NO_x emission of liquid fuels while it over-predicts NO_x for methane significantly. Methane produces about an order magnitude higher CH mole fraction compared to liquid fuels. Higher levels of CH mole fraction result in higher concentrations of NCN in the PSB. Glarborg et al. pathways from NCN to NO_x generates about 50% higher concentrations of NO_x than measured.

4. Aromatic fuels emit more CO and NO_x compared to aliphatic fuels as shown experimentally and numerically. CRN results show that this is due to higher concentrations of O-atom and H-atom. More available concentration of CO available produces more H-atom from oxidation of CO by the OH radical. Higher pool of H radical means higher O-atom production from oxidation of H-atom with oxygen. A larger pool of H-atom and O-atom concentrations lead to higher NO_x production for aromatics compared to aliphatics.

Chapter 5

SUMMARY AND CONCLUSION

This dissertation examines lean premixed combustion of pure and alternative liquid fuels with the goal of supporting flexibility in aviation fuels. A single Jet Stirred Reactor (JSR), laboratory-scale idealization of the primary zone of a gas turbine engine, is used for the experimental and modeling efforts. By using the JSR, temperature and fuel chemistry are isolated and studied independently. Experimental data on NO_x emissions are collected and numerical models are used to understand the formation of emissions.

5.1 Summary of Experimental Work

Alternative aviation fuels are evaluated for lean-flame NO_x formation and lean-flame blowout (LFBO). LFBO results are shown in Appendix B.2. The alternative aviation fuels evaluated are: hydro-processed renewable jet (HRJ) made from camelina and tallow, Fischer-Tropsch (FT) jet made from natural gas, and alcohol-based jet. Chromatographic analysis (from another lab) shows that these fuels are composed mainly of iso-alkanes. For comparison, a petroleum-based Jet-A is burned. Additionally, several pure fuels are burnt: n-hexane, cyclo-hexane, n-octane, iso-octane, n-dodecane, 1-3-5 tri-methyl benzene (TMB), and toluene. NO_x is measured by probe sampling and chemiluminescent analysis at a fixed temperature for each fuel. The major findings are the following:

1. The combustion of alternative and traditional commercial jet fuels show relatively minor differences in NO_x. The trend observed at three different temperatures of the recirculation zone shows: HRJ-tallow $<$ FT-natural gas $<$ alcohol-based jet$<$ HRJ-camelina.

2. The largest difference in NO_x is between aliphatic and aromatic fuels. Aromatics produce about 30% more NO_x than aliphatic fuels. Further investigation for this difference is going to be conducted by chemical kinetic modeling of model compounds in Chapter 4.

5.2 Summary of CFD Modeling

Computational Fluid Dynamics (CFD) is used to model the fluid structure and chemistry inside the JSR. Combustion of simple gaseous fuels such as hydrogen and methane are simulated instead of liquid fuels due to the high computational demands of these detailed fluid dynamics models. The main goal of the CFD analysis is to aid in generating a CRN model that is used for prediction of NO_x emissions from combustion of liquid fuels. Additionally, CFD is used to explore the temperature and species fluctuations in the recirculation zone of the JSR as analyzing the nitrogen species are formation/destruction inside the reactor.

RANS turbulence model is initially used for each case to develop a solution that is later utilized to initialize the Large Eddy Simulation (LES) modeling of the flow. Modeling chemistry correctly is essential for this study, therefore, the Complex Chemistry model with Laminar Flame Concept (LFC) is utilized. This model solves transport equations for species and calculates reaction rates by Arrhenius kinetic expressions.

The findings of this chapter are summarized below:

1. LES modeling of H_2 combustion with NO_x chemistry shows that most of the radicals are mainly formed in the flame brush. O-atom, H-atom, and OH radical have the highest concentrations in this region. These radicals react with nitrogen molecules and form important NO_x species such as N_2O, NNH, and NH. Since the concentration of O-atom and H-atom are highest in the flame brush, the ROP of NO_x species are highest in the flame brush as well. NO_x has the highest concentration in the recirculation zone due to the high residence time this zone provides.

2. The data history obtained for a time equal to 2 times the mean residence time of the

JSR. The temperature, O-atom, and H-atom fluctuations in the sampling location of the reactor is not negligible. However, the case of H2 with NO_x chemistry showed that NO_x mole fraction fluctuates only about 0.1 *ppm* from the mean value of 5 ppm on a dry basis. This predicted mean value is only 2 ppm lower than the measured value. This under-prediction is due to the mean temperature being predicted 40 degrees lower than it is measured.

3. LES modeling of CH_4 combustion shows that the jet occupies a larger volume in the JSR compared to the jet observed in the combustion of hydrogen. The mean temperature at the recirculation zone is predicted to be at 1790 K, which is in good agreement with the measured value of 1805 K. The time history of the solution at the sampling location shows that temperature and species fluctuations are significant.

5.3 Summary of CRN Modeling

A 3-zone chemical reactor network (CRN) model is developed and implemented to model the flame zones inside the JSR. The goal of this work is to predict emissions and explain the experimental trends observed for combustion of fuels such as methane, iso-octane, n-octane, n-dodecane, 135-TMB, and toluene. Two sets of hydrocarbon mechanisms are utilized in the CRN model, the individual fuel hydrocarbon mechanisms and a surrogate jet fuel mechanism. NO_x is modeled using 2011 Klippenstein et al. H-N-O mechanism as well as two different prompt mechanisms of Konnov and Glarborg et al. The following findings are observed by analyzing the results of the CRN modeling.

1. NO_x is predicted well when the individual fuel hydrocarbon mechanisms or the surrogate jet fuel mechanism are used with Klippenstein et al. H-N-O and Konnov prompt NO_x mechanisms. These emissions are slightly under-predicted for n-alkanes and iso-octane. These results are consistent among three different recirculation zone temperatures of 1700, 1800, and 1900 K.

2. Sensitivity analysis on NO_x pathways shows that N_2O is the major pathway to NO_x formation in the JSR at the recirculation zone temperature of 1800K. Zeldovich route is the second most important route followed by the prompt mechanism. NNH route has a small contribution to overall NO_x for these fuels burned lean-premixed.

3. Compared to the Konnov mechanism, the Glarborg et al. prompt mechanism under-predicts NO_x emission of liquid fuels while it over-predicts NO_x for methane significantly. Methane produces about an order magnitude higher CH mole fraction compared to liquid fuels. Higher levels of CH mole fraction result in higher concentrations of NCN in the PSB. Glarborg et al. pathways from NCN to NO_x generates about 50% higher concentrations of NO_x than measured.

4. Aromatic fuels emit more CO and NO_x compared to aliphatic fuels as shown experimentally and numerically. CRN results show that this is due to higher concentration of O-atom and H-atom present. Having higher concentration of CO available produces more H-atom from oxidation of CO by the OH radical. Higher pool of H radical means higher O-atom production from oxidation of H-atom with oxygen. Higher H-atom and O-atom concentrations lead to higher NO_x production for aromatics compared to aliphatics.

BIBLIOGRAPHY

[1] CHEMKIN-PRO, ANSYS Reaction Design, Version 15113.

[2] ANSYS Fluent. ANSYS Fluent Theory Guide, Release 15.0, 2013.

[3] ASTM. Standard Test Method for Estimation of Net Heat of Combustion of Aviation Fuels (D3338). Technical report, 2009.

[4] Nour Atef, Goutham Kukkadapu, Samah Y Mohamed, Mariam Al, Colin Banyon, Marco Mehl, Karl Alexander, Ehson F Nasir, A Alfazazi, Apurba K Das, Charles K Westbrook, William J Pitz, Tianfeng Lu, Aamir Farooq, Chih-jen Sung, Henry J Curran, and S Mani Sarathy. A comprehensive iso-octane combustion model with improved thermochemistry and chemical kinetics. *Combustion and Flame*, 178:111–134, 2017.

[5] Joanna Blauwens, Bruno Smets, and Jozef Peeters. Mechanism of "prompt" no formation in hydrocarbon flames. *Symposium (International) on Combustion*, 16(1):1055–1064, 1977.

[6] J. Blust, D. Ballal, G. Sturgess, J. Blust, D. Ballal, and G. Sturgess. Emissions characteristics of liquid hydrocarbons in a well stirred reactor. *33rd Joint Propulsion Conference and Exhibit*, 1997.

[7] J. W. Blust, D R Ballal, and G J Sturgess. Fuel Effects on Lean Blowout and Emissions from a Well-Stirred Reactor. *Journal of Propulsion and Power*, 15(2):216–223, 1999.

[8] James W. Blust. *Effects of fuel structure on emissions and stability in the well stirred reactor*. Phd, 2001.

[9] K. Boyd Fackler, Megan Karalus, Igor Novosselov, John Kramlich, Philip Malte, and Shazib Vijlee. NO x Behavior for Lean-Premixed Combustion of Alternative Gaseous Fuels. *Journal of Engineering for Gas Turbines and Power*, 138(4):041504, 2015.

[10] Joseph W. Bozzelli and Anthony M. Dean. O + NNH: A possible new route for NOX formation in flames, 1995.

[11] G Bulat, W P Jones, and A J Marquis. NO and CO formation in an industrial gas-turbine combustion chamber using LES with the Eulerian sub-grid PDF method. *Combustion and Flame*, 161(7):1804–1825, 2014.

[12] Jeremy Cain, Matthew J. Dewitt, David Blunck, Edwin Corporan, Richard Striebich, David Anneken, Christopher Klingshirn, W. M. Roquemore, and Randy Vander Wal. Characterization of gaseous and particulate emissions from a turboshaft engine burning conventional, alternative, and surrogate fuels. *Energy and Fuels*, 27(4):2290–2302, 2013.

[13] Edwin Corporan, Matthew J. DeWitt, Vincent Belovich, Robert Pawlik, Amy C. Lynch, James R. Gord, and Terence R. Meyer. Emissions characteristics of a turbine engine and research combustor burning a Fischer-Tropsch jet fuel. *Energy and Fuels*, 21(5):2615–2626, 2007.

[14] Edwin Corporan, Tim Edwards, Linda Shafer, Matthew J. Dewitt, Christopher Klingshirn, Steven Zabarnick, Zachary West, Richard Striebich, John Graham, and Jim Klein. Chemical, thermal stability, seal swell, and emissions studies of alternative jet fuels. *Energy and Fuels*, 25(3):955–966, 2011.

[15] Edwin Corporan, Time Edwards, Scott Stouffer, Tyler Hendershott, Matt Dewitt, Chris Klingshirn, Zackary West, Chris Bruening, and Richard Striebich. Impacts of Fuel Properties on Combustor Performance , Operability , and Emissions Characteristics. *55th AIAA Aerospace Sciences Meeting*, pages 1–19, 2017.

[16] N J Dam and J J Meulen. Laser-induced fluorescence of NCN in low. 33(22):2620–2622, 2008.

[17] Matthew J. DeWitt, Edwin Corporan, John Graham, and Donald Minus. Effects of aromatic type and concentration in Fischer-Tropsch fuel on emissions production and material compatibility. *Energy and Fuels*, 22(4):2411–2418, 2008.

[18] Pascal Diévart, Hwan Ho Kim, Sang Hee Won, Yiguang Ju, Frederick L. Dryer, Stephen Dooley, Weijing Wang, and Matthew A. Oehlschlaeger. The combustion properties of 1,3,5-trimethylbenzene and a kinetic model. *Fuel*, 109:125–136, 2013.

[19] Pascal Diévart, Hwan Ho Kim, Sang Hee Won, Yiguang Ju, Frederick L. Dryer, Stephen Dooley, Weijing Wang, and Matthew A. Oehlschlaeger. The combustion properties of 1,3,5-trimethylbenzene and a kinetic model. *Fuel*, 109:125–136, 2013.

[20] Stephen Dooley, Sang Hee Won, Marcos Chaos, Joshua Heyne, Yiguang Ju, Frederick L Dryer, Kamal Kumar, Chih-jen Sung, Haowei Wang, Matthew A Oehlschlaeger, Robert J Santoro, and Thomas A Litzinger. A jet fuel surrogate formulated by real fuel properties. *Combustion and Flame*, 157(12):2333–2339, 2010.

[21] Tim Edwards. Personal Communication, Air Force Research Laboratory, WPAFB, Dayton, Ohio, 2014.

[22] A. El Bakali, L. Pillier, P. Desgroux, B. Lefort, L. Gasnot, J. F. Pauwels, and I. Da Costa. NO prediction in natural gas flames using GDF-Kin®3.0 mechanism NCN and HCN contribution to prompt-NO formation. *Fuel*, 85(7-8):896–909, 2006.

[23] Ivar S. Ertesvåg and Bjørn F. Magnussen. The Eddy Dissipation Turbulence Energy Cascade Model. *Combustion Science and Technology*, 159(1):213–235, 2000.

[24] Boyd Fackler. *A Study of Pollutant Formation from the Lean Premixed Combustion of Gaseous Fuel Alternatives to Natural Gas*. Phd dissertation, University of Washington, 2011.

[25] K Boyd Fackler, Megan F Karalus, Igor V Novosselov, John C Kramlich, and Philip C Malte. Experimental and Numerical Study of NOx Formation From the Lean Premixed Combustion of CH4 Mixed With CO2 and N2. *Journal of Engineering for Gas Turbines and Power*, 133(12):121502, 2011.

[26] Nancy Faßheber, Johannes Dammeier, and Gernot Friedrichs. Direct measurements of the total rate constant of the reaction NCN + H and implications for the product branching ratio and the enthalpy of formation of NCN. *Phys. Chem. Chem. Phys.*, 16(23):11647–11657, 2014.

[27] C.P. Fenimore. Formation of nitric oxide in premixed hydrocarbon flames. *Symposium (International) on Combustion*, 13(1):373–380, jan 1971.

[28] M.A. Field, D.W. Gill, B.B. Morgan, and P.G.W Hawksley. *Combustion of Pulvarised Coal*. 1967.

[29] J Gandara, M Jones, and R. Lockwood. Vitreous Carbon Converter Experiment for Converting NO2 to NO for a Jet Stirred Reactor. Technical report, ME 495 Project, Dept. of Mech. Engr, University of Washington, Seattle, WA, 2016.

[30] M Garcia-Perez and J C Kramlich. "Effect of Residual Oxygenated Functional Groups on the Behavior of Alternative Jet Fuel Properties", Presentation to FAA Aviation Sustainability Center by Washington State University (Pullman, WA) and the University of Washington (Seattle, WA), 2016.

[31] Peter Glarborg, James A Miller, Branko Ruscic, and Stephen J Klippenstein. Modeling nitrogen chemistry in combustion. *Progress in Energy and Combustion Science*, 67:1–38, 2018.

[32] Zhiwei Qin Gregory P. Smith, David M. Golden, Michael Frenklach, Nigel W. Moriarty, Boris Eiteneer, Mikhail Goldenberg, C. Thomas Bowman, Ronald K. Hanson, Soonho Song, William C. Gardiner, Jr., Vitali V. Lissianski. GRI-Mech 3.0.

[33] W. P. Jones and R. P. Lindstedt. Global Reaction Schemes for Hydrocarbon Combustion. *Combustion and Flame*, 73:233–249, 1988.

[34] Megan Karalus. *An Investigation of Lean Blowout of Gaseous Fuel Alternatives to Natural Gas*. Phd dissertation, University of Washington, Seattle, WA, 2013.

[35] Megan F Karalus, K Boyd Fackler, Igor V Novosselov, John C Kramlich, and Philip C Malte. A skeletal mechanism for the reactive flow simulation of mthane combustion. In *Proceedings of ASME Turbo Expo 2013*, 2013.

[36] Bhupendra Khandelwal, Emamode Ubogu, Muhammad Akram, Simon Blakey, and Christopher W Wilson. Experimental Analysis on Emission Production and Performance of Stressed 100% SPK, Stressed fully Formulated Synthetic Jet Fuel and Jet A-1 in a Small Gas Turbine Engine. *11th International Energy Conversion Engineering Conference*, pages 1–10, 2013.

[37] C. D. Klingshirn, M. DeWitt, R. Striebich, D. Anneken, L. Shafer, E. Corporan, M. Wagner, and D. Brigalli. Hydroprocessed Renewable Jet Fuel Evaluation, Performance, and Emissions in a T63 Turbine Engine. *Journal of Engineering for Gas Turbines and Power*, 134(May 2012):051506, 2012.

[38] Stephen J Klippenstein, Lawrence B Harding, Peter Glarborg, and James A Miller. The role of NNH in NO formation and control. *Combustion and Flame*, 158(4):774–789, 2011.

[39] A A Konnov. Implementation of the NCN pathway of prompt-NO formation in the detailed reaction mechanism. *Combustion and Flame*, 156(11):2093–2105, 2009.

[40] A. A. Konnov, G. Colcson, and J. Ruyck. Brief Communication. *Combustion and Flame*, 133(3):548–550, 2000.

[41] J C Kramlich and P C Malte. Modeling and Measurement of Sample Probe Effects on Pollutant Gases Drawn from Flame Zones. *Combustion Science and Technology*, 18(3-4):91–104, 1978.

[42] Kenneth K Kuo. *Fundamentals of Turbulent and Multiphase Combustion*. John Wiley & Sons, 2012.

[43] N. Lamoureux, P. Desgroux, A. El Bakali, and J. F. Pauwels. Experimental and numerical study of the role of NCN in prompt-NO formation in low-pressure CH4-O2-N2and C2H2-O2-N2 flames. *Combustion and Flame*, 157(10):1929–1941, 2010.

[44] N. Lamoureux, X. Mercier, C. Western, J. F. Pauwels, and P. Desgroux. NCN quantitative measurement in a laminar low pressure flame. *Proceedings of the Combustion Institute*, 32 I(1):937–944, 2009.

[45] Andrew Campbell Lee. *Experimental Investigation of Liquid Fuel Vaporization and Mixing in Steam and Air*. PhD thesis, University of Washington, 2003.

[46] John C Y Lee. *Reduction of NO_x Emission for Lean Prevaporized-Premixed Combustors*. PhD thesis, University of Washington, 2000.

[47] John C Y Lee. *Reduction of NOX Emissions for Lean Prevaporized-Premixed Combustors*. Phd dissertation, University of Washington, 2000.

[48] John C. Y. Lee, Phillip C. Malte, and Michael A. Benjamin. Low Nox Combustion for Liquid Fuels: Atmospheric Pressure Experiments Using a Staged Prevaporizer-Premixer. *Asme Turbo Expo*, 125(4):861–871, 2001.

[49] Juan Li, Zhenwei Zhao, Andrei Kazakov, and Frederick L Dryer. An Updated Comprehensive Kinetic Model of Hydrogen Combustion. *International Journal of Chemical Kinetics*, 36(10):566–575, 2004.

[50] Prem Lobo, Lucas Rye, Paul I. Williams, Simon Christie, Ilona Uryga-Bugajska, Christopher W. Wilson, Donald E. Hagen, Philip D. Whitefield, Simon Blakey, Hugh Coe, David Raper, and Mohamed Pourkashanian. Impact of Alternative Fuels on Emissions Characteristics of a Gas Turbine Engine âĂŞ Part 1: Gaseous and Particulate Matter Emissions. *Environmental Science & Technology*, 46(19):10805–10811, 2012.

[51] Bjørn F Magnussen. On the structure of turbulence and a generalized eddy dissipation concept for chemical reaction in turbulent flows. In *19th American Institute of Aeronautics and Astronautics Aerospace Science Meeting*, 1981.

[52] Bjørn F Magnussen. THE EDDY DISSIPATION CONCEPT A BRIDGE BETWEEN SCIENCE AND TECHNOLOGY Invited paper at ECCOMAS Thematic Conference on Computational Combustion , Lisbon , June 21-24 , 2005 THE EDDY DISSIPATION CONCEPT A BRIDGE BETWEEN SCIENCE AND. *Eccomas*, 2005.

[53] George Mallouppas, Graham Goldin, Yongzhe Zhang, Piyush Thakre, Niveditha Krishnamoorthy, Rajesh Rawat, David Gosman, Jim Rogerson, and Ghenadie Bulat. Investigation of an industrial gas turbine combustor and pollutant formation using LES. In *Asme Turbo Expo*, 2017.

[54] P. C. Malte and D. T. Pratt. The role of energy-realeasing kinetics in NOX formation: Fuel-lean, jet-stirred CO-air combustion. *Combustion Science and Technology*, 9:221–231, 1974.

[55] S Mathur and S C Saxena. Relations between thermal conductivity and diffusion coefficients of pure and mixed polyatomic gases. *Proceedings of the Physical Society*, 89(3):753, 1966.

[56] M Mehl, Hj Curran, W J Pitz, and Charles K Westbrook. Chemical kinetic modeling of component mixtures relevant to gasoline. In *European Combustion Meeting*, pages 1–6, 2009.

[57] J A Miller and P Glarborg. Modeling the Thermal De-NO x Process : Closing in on a Final Solution. *Journal of Chemical Kinetics*, 31(11):754–765, 1999.

[58] James A Miller and Carl F Melius. Kinetic and thermodynamic issues in the formation of aromatic compounds in flames of aliphatic fuels. *Combustion and Flame*, 91(1):21–39, 1992.

[59] M. Monroig, O., Corporan, E., DeWitt, M., Mortimer, B., Ostdiek, D., and Wagner. Effect of Jet Fuel Aromatic Concentration on the Emissions of a T63 Engine. *American Chemical Society Division of Fuel Chemistry*, 50(1):335–337, 2015.

[60] Clifford a. Moses and Petrus N. J. Roets. Properties, Characteristics, and Combustion Performance of Sasol Fully Synthetic Jet Fuel. *Journal of Engineering for Gas Turbines and Power*, 131(4):041502, 2009.

[61] L. V. Moskaleva and M. C. Lin. The spin-conserved reaction CH + n2âĘŠ H + NCN: A major pathway to prompt no studied by quantum/statistical theory calculations and kinetic modeling of rate constant. *Proceedings of the Combustion Institute*, 28(2):2393–2401, 2000.

[62] V Moureau, P Domingo, and L Vervisch. From Large-Eddy Simulation to Direct Numerical Simulation of a lean premixed swirl flame : Filtered laminar flame-PDF modeling. *Combustion and Flame*, 158(7):1340–1357, 2011.

[63] Amir Mzé-Ahmed, Philippe Dagaut, Kamal Hadj-Ali, Guillaume Dayma, Thomas Kick, Julia Herbst, Trupti Kathrotia, Marina Braun-Unkhoff, Jürgen Herzler, Clemens Naumann, and Uwe Riedel. Oxidation of a Coal-to-Liquid Synthetic Jet Fuel: Experimental and Chemical Kinetic Modeling Study. *Energy & Fuels*, 26(10):6070–6079, 2012.

[64] D. G. Nicol, P. C. Malte, a. J. Hamer, R. J. Roby, and R. C. Steele. Development of a Five-Step Global Methane Oxidation-NO Formation Mechanism for Lean-Premixed Gas Turbine Combustion. *Journal of Engineering for Gas Turbines and Power*, 121(2):272, 1999.

[65] F. Nicoud and F. Ducros. Subgrid-scale stress modelling based on the square of the velocity gradient tensor. *Flow, Turbulence and Combustion*, 62(3):183–200, 1999.

[66] Igor V Novosselov. *Chemical Reactor Networks for Combustion Systems Modeling*. PhD thesis, University of Washington, 2006.

[67] Bruce E Poling. The properties of gases and liquids, 2001.

[68] Stephen B Pope. Ten questions concerning the large-eddy simulation of turbulent flows. *New Journal of Physics*, 6(35), 2004.

[69] Stphen B. Pope. *Turbulent Flows*. 2000.

[70] Teodara Ruta, David C. Homing, John C. Y. Lee, and Phillip C. Malte. NOx dependency on residence time and inlet temperature for lean premixed combustion in JSR. *ASME*.

[71] T Rutar, J C Y Lee, P Dagaut, P C Malte, and A A Byrne. NOx formation pathways in lean-premixed-prevapourized combustion of fuels with carbon-to-hydrogen ratio between 0.25 and 0.88. *Proceedings of the Institution of Mechanical Engineers, Part A: Journal of Power and Energy*, 221(3):387–398, 2007.

[72] T. Rutar and P. C. Malte. NOx Formation in High-Pressure Jet-Stirred Reactors With Significance to Lean-Premixed Combustion Turbines. *Journal of Engineering for Gas Turbines and Power*, 124(4):776, 2002.

[73] Teodora Rutar, Philip C. Malte, and John C. Kramlich. Investigation of NOx and CO formation in lean-premixed, methane/air, high-intensity, confined flames at elevated pressures. *Proceedings of the Combustion Institute*, 28(2):2435–2441, 2000.

[74] S. M. Sarathy, C. K. Westbrook, M. Mehl, W. J. Pitz, C. Togbe, P. Dagaut, H. Wang, M. A. Oehlschlaeger, U. Niemann, K. Seshadri, P. S. Veloo, C. Ji, F. N. Egolfopoulos, and T. Lu. Comprehensive chemical kinetic modeling of the oxidation of 2-methylalkanes from C7 to C20. *Combustion and Flame*, 158(12):2338–2357, 2011.

[75] Z. Ren S.B. Pope, V. Hiremath, S.R. Lantz and L. Lu. A Fortran 90 library to accelerate the implementation of combustion chemistry, 2012.

[76] Tsan-Hsing Shih, William W Liou, Aamir Shabbir, Zhigang Yang, and Jiang Zhu. A new k-Ït¸ eddy viscosity model for high reynolds number turbulent flows. *Computers & Fluids*, 24(3):227–238, 1995.

[77] Siemens PLM. Simcenter, STAR-CCM+, Academic Research, Release 12.02, 2017.

[78] C. J. Sung, C. K. Law, and J.-Y. Chen. Augmented Reduced Mechanisms for NO Emission in Methane Oxidation. *Combustion and Flame*, 125(1-2):906–919, 2001.

[79] M. T. Timko, Z. Yu, T. B. Onasch, H. W. Wong, R. C. Miake-Lye, A. J. Beyersdorf, B. E. Anderson, K. L. Thornhill, E. L. Winstead, E. Corporan, M. J. Dewitt, C. D. Klingshirn, C. Wey, K. Tacina, D. S. Liscinsky, R. Howard, and A. Bhargava. Particulate emissions of gas turbine engine combustion of a fischer-tropsch synthetic fuel. *Energy and Fuels*, 24(11):5883–5896, 2010.

[80] Edwin Timko, Michael T. ; Herndon, Scott C. ; De La Rosa Blanco, Elena ; Wood, Ezra C. ; Yu, Zhenhong ; Miake-Lye, Richard C. ; Knighton, W. Berk ; Shafer, Linda ; Dewitt, Matthew J. ; Corporan. Combustion Products of Petroleum Jet Fuel, a FischerâĂŞTropsch Synthetic Fuel, and a Biomass Fatty Acid Methyl Ester Fuel for a Gas Turbine Engine. *Combustion Science and Technology*, 183(10):1039–1068, 2011.

[81] Venkatesh Vasudevan, Ronald K. Hanson, Craig T. Bowman, David M. Golden, and David F. Davidson. Shock tube study of the reaction of CH with N2: overall rate and branching ratio. *The Journal of Physical Chemistry A*, 111(46):11818–11830, 2007.

[82] H K Versteeg and W Malalasekera. *An Introduction to Computational Fluid Dynamics*. 2007.

[83] Shazib Z. Vijlee. *Effects of Fuel Composition on Combustion Stability and NOX Emissions for Traditional and Alternative Jet Fuels*. Phd dissertation, University of Washington, Seattle, WA, 2014.

[84] Shazib Z. Vijlee, John C. Kramlich, Ann M. Mescher, Scott D. Stouffer, and Alanna R. O'Neil-Abels. Characterizing Combustion of Synthetic and Conventional Fuels in a Toroidal Well Stirred Reactor. In *Asme Turbo Expo 2013*, 2013.

[85] Charles K. Westbrook and Frederick L. Dryer. Chemical Kinetic Modeling of Hydrocarbon Combustion. *Progress in Energy and Combustion Science*, 10:1–57, 1984.

[86] Bradley A. Williams and James W. Fleming. Experimental and modeling study of NO formation in 10 torr methane and propane flames: Evidence for additional prompt-NO precursors. *Proceedings of the Combustion Institute*, 31 I:1109–1117, 2007.

[87] Wenhao Yuan, Yuyang Li, Philippe Dagaut, Jiuzhong Yang, and Fei Qi. Investigation on the pyrolysis and oxidation of toluene over a wide range conditions. I. Flow reactor pyrolysis and jet stirred reactor oxidation. *Combustion and Flame*, 162(1):3–21, 2015.

[88] Y.B. Zeldovich. The oxidation of nitrogen in combustion and explosions. *Acta Physicochemica USSR*, 21:577–628, 1946.

[89] R. S. Zhu, S. C. Xu, and M. C. Lin. Ab initio chemical kinetics for the reactions of N2with singlet and triplet C2O radicals. *Chemical Physics Letters*, 488(4-6):121–125, 2010.

Appendix A

FUELS REFERENCE AND COMPOSITION

Additional information about the liquid fuels burnt in this work is given in this appendix. Fuels identification numbers as well as fuel compositions are provided.

A.1 Fuels Reference

The alternative fuels and jet-A have been obtained from AFRL. Table A.1 shows the identification number (POSF#) of these fuels assigned by AFRL along with the manufacturer. For these fuels, the CAS# is used as fuel identification number.

Fuel	Fuel Identification	Manufacturer
n-Hexan	CAS # 110-54-3	Acros Organics
n-Octane	CAS # 111-65-9	Acros Organics
iso-Octane	CAS #540-84-1	Chevron Philips
HRJ-Tallow	POSF# 6308	UOP
HRJ-Camelina	POSF# 10301	UOP
FT-Natural Gas	POSF# 5018	Syntroleum Corp.
n-Dodecane	CAS# 112-40-3	Alfa Aesar
Alcohol-based Jet	POSF# 8092	GEVO Inc.
Jet-A	POSF# 10325	Shell Chemicals
135-TMB	CAS# 108-67-8	TCI America
Toluene	CAS# 108-88-3	Sigma-Aldrich

Table A.1: List of fuels with product numbers and manufacturer.

A.2 Detailed Fuel Composition

Fuel composition of alternative fuels and jet-A is presented in detail in Table A.2. The data are attained using two-dimensional gas chromatography by AFRL.

Table A.2: Two dimensional gas chromatography data for the jet fuels used in this study provided by AFRL. The values provided in this table has the unit of weight %.

Fuel	Jet-A	FT-Natural Gas	HRJ-Camelina	HRJ-Tallow	Alcohol-based Jet
POSF #	10325	5018	10301	6308	8092
Aromatics					
Alkylbenzenes					
benzene (C06)	<0.01	<0.01	<0.01	<0.01	<0.01
toluene (C07)	0.16	<0.01	<0.01	<0.01	<0.01
C2-benzene (C08)	1.11	0.02	0.02	0.01	<0.01
C3-benzene (C09)	3.03	0.03	0.04	0.01	<0.01
C4-benzene (C10)	3.33	0.03	0.03	<0.01	<0.01
C5-benzene (C11)	2.23	0.03	0.02	<0.01	<0.01
C6-benzene (C12)	1.32	0.02	0.01	<0.01	<0.01
C7-benzene (C13)	0.76	0.02	0.01	<0.01	0.01
C8-benzene (C14)	0.52	0.01	<0.01	<0.01	<0.01
C9-benzene (C15)	0.30	<0.01	<0.01	<0.01	<0.01
C10+-benzene (C16+)	0.14	<0.01	<0.01	<0.01	<0.01
Total Alkylbenzenes	**12.90**	**0.16**	**0.14**	**0.05**	**0.02**
Diaromatics					
diaromatic-C10	0.22	<0.01	<0.01	<0.01	<0.01
diaromatic-C11	0.66	<0.01	<0.01	<0.01	<0.01
diaromatic-C12	0.86	<0.01	<0.01	<0.01	0.01
diaromatic-C13	0.41	<0.01	<0.01	<0.01	<0.01
diaromatic-C14+	0.18	<0.01	<0.01	<0.01	<0.01
Total Alkylnaphthalenes	**2.33**	**<0.01**	**<0.01**	**<0.01**	**0.02**
Cycloaromatics					

cycloaromatic-C09	0.03	<0.01	<0.01	<0.01	<0.01
cycloaromatic-C10	0.28	<0.01	<0.01	<0.01	<0.01
cycloaromatic-C11	0.67	<0.01	<0.01	<0.01	<0.01
cycloaromatic-C12	0.93	<0.01	<0.01	<0.01	0.01
cycloaromatic-C13	0.86	<0.01	<0.01	<0.01	<0.01
cycloaromatic-C14	0.45	<0.01	<0.01	<0.01	<0.01
cycloaromatics-C15+	0.22	<0.01	<0.01	<0.01	<0.01
Total Cycloaromatics	**3.43**	**0.03**	**0.03**	**0.02**	**0.02**
Total Aromatics	**18.66**	**0.20**	**0.18**	**0.08**	**0.06**
Paraffins					
iso-Paraffins					
C07 and lower-iso	0.18	0.01	0.02	<0.01	0.09
C08-isoparaffins	0.55	1.48	1.39	2.10	0.36
C09-isoparaffins	1.20	6.28	10.87	9.40	0.08
C10-isoparaffins	4.07	8.29	11.67	9.69	0.18
C11-isoparaffins	5.68	9.89	10.24	9.69	0.32
C12-isoparaffins	5.41	10.93	8.54	9.25	79.74
C13-isoparaffins	4.27	11.50	8.48	9.53	1.20
C14-isoparaffins	4.16	11.16	6.41	7.84	0.00
C15-isoparaffins	2.41	9.92	5.75	11.75	0.00
C16-isoparaffins	0.98	5.84	10.95	12.83	15.99
C17-isoparaffins	0.38	0.56	11.56	5.92	0.00
C18-isoparaffins	0.11	0.02	0.81	0.34	0.00
C19-isoparaffins	0.05	<0.01	<0.01	<0.01	0.00
C20-isoparaffins	0.01	<0.01	<0.01	<0.01	1.20
C21-isoparaffins	<0.01	<0.01	<0.01	<0.01	0.00
C22-isoparaffins	<0.01	<0.01	<0.01	<0.01	0.00
C23-isoparaffins	<0.01	<0.01	<0.01	<0.01	0.00
C24-isoparaffins	<0.01	<0.01	<0.01	<0.01	0.00
Total iso-Paraffins	**29.45**	**75.88**	**86.70**	**88.34**	**99.14**
n-Paraffins					
n-C07	0.14	0.03	0.02	0.00	<0.01

n-C08	0.56	1.37	1.31	1.49	<0.01
n-C09	1.45	3.04	1.89	1.45	<0.01
n-C10	3.29	4.00	1.54	1.23	<0.01
n-C11	4.31	4.24	1.14	1.18	<0.01
n-C12	3.74	3.87	1.01	1.09	<0.01
n-C13	2.80	3.10	0.89	1.04	<0.01
n-C14	2.03	2.26	0.77	0.88	<0.01
n-C15	1.02	1.32	0.99	1.57	<0.01
n-C16	0.42	0.14	1.22	0.68	<0.01
n-C17	0.20	<0.01	0.17	0.07	<0.01
n-C18	0.04	<0.01	<0.01	<0.01	<0.01
n-C19	0.01	<0.01	<0.01	<0.01	<0.01
n-C20	<0.01	<0.01	<0.01	<0.01	<0.01
n-C21	<0.01	<0.01	<0.01	<0.01	0.00
n-C22	<0.01	<0.01	<0.01	<0.01	0.00
n-C23	<0.01	<0.01	<0.01	<0.01	0.00
Total n-Paraffins	**20.03**	**23.37**	**10.96**	**10.69**	**<0.01**
Cycloparaffins					
Monocycloparaffins					
C07-monocyclocycloparaffins	0.33	<0.01	<0.01	<0.01	<0.01
C08-monocyclocycloparaffins	0.80	0.12	0.37	0.26	0.05
C09-monocyclocycloparaffins	2.27	0.16	0.86	0.25	0.02
C10-monocyclocycloparaffins	4.57	0.12	0.38	0.13	0.02
C11-monocyclocycloparaffins	5.42	0.07	0.14	0.07	0.27
C12-monocyclocycloparaffins	3.77	0.02	0.07	0.02	0.06
C13-monocyclocycloparaffins	3.73	<0.01	0.09	0.04	<0.01
C14-monocyclocycloparaffins	2.06	<0.01	0.01	<0.01	<0.01
C15-monocyclocycloparaffins	1.27	<0.01	<0.01	<0.01	<0.01
C16-monocyclocycloparaffins	0.43	<0.01	<0.01	<0.01	<0.01
C17-monocyclocycloparaffins	0.18	<0.01	<0.01	<0.01	0.17
C18-monocyclocycloparaffins	0.04	<0.01	<0.01	<0.01	<0.01
C19+-monocyclocycloparaffins	0.02	<0.01	<0.01	<0.01	0.04
Total Monocycloparaffins	**24.87**	**0.50**	**1.92**	**0.77**	**0.64**

Dicycloparaffins					
C08-dicycloparaffins	0.04	<0.01	<0.01	<0.01	<0.01
C09-dicycloparaffins	0.45	<0.01	0.02	<0.01	<0.01
C10-dicycloparaffins	0.46	0.01	0.03	0.01	0.13
C11-dicycloparaffins	1.63	0.01	0.06	0.03	<0.01
C12-dicycloparaffins	1.72	0.01	0.06	0.04	<0.01
C13-dicycloparaffins	1.50	<0.01	0.03	0.02	0.01
C14-dicycloparaffins	0.79	<0.01	0.01	<0.01	<0.01
C15-dicycloparaffins	0.14	<0.01	<0.01	<0.01	<0.01
C16-dicycloparaffins	0.02	<0.01	<0.01	<0.01	<0.01
C17+-dicycloparaffins	0.02	<0.01	<0.01	<0.01	<0.01
Total Dicycloparaffins	**6.78**	**0.05**	**0.23**	**0.12**	**0.16**
Tricycloparaffins					
C10-tricycloparaffins	0.02	<0.01	<0.01	<0.01	<0.01
C11-tricycloparaffins	0.07	<0.01	<0.01	<0.01	<0.01
C12-tricycloparaffins	0.11	<0.01	<0.01	<0.01	<0.01
Total Tricycloparaffins	**0.21**	**<0.01**	**<0.01**	**<0.01**	**<0.01**
Total Cycloparaffins	**31.86**	**0.55**	**2.15**	**0.89**	**0.80**
Total Paraffins	81.34	99.80	99.82	99.92	99.94

A.3 Calibration of fuel and air flow meters

This section provides pictures of the fuel and air handling equipments used on the combustion rig as well as the calibration data for fuels and air.

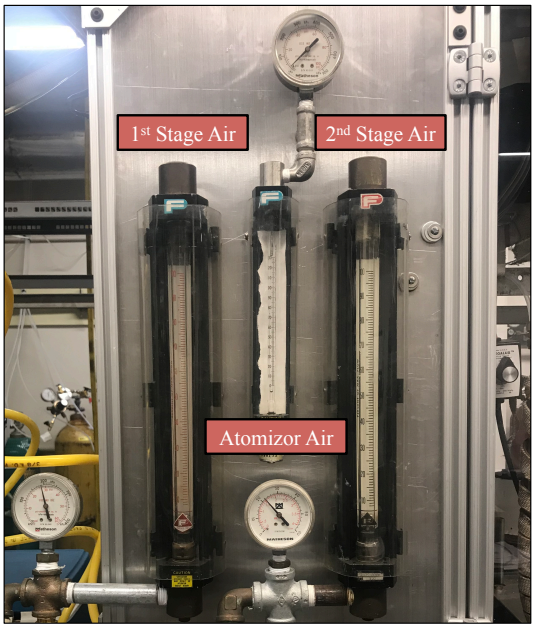

Figure A.1: Rotameters used to measure 1^{st} stage, 2^{nd} stage, and atomizor air.

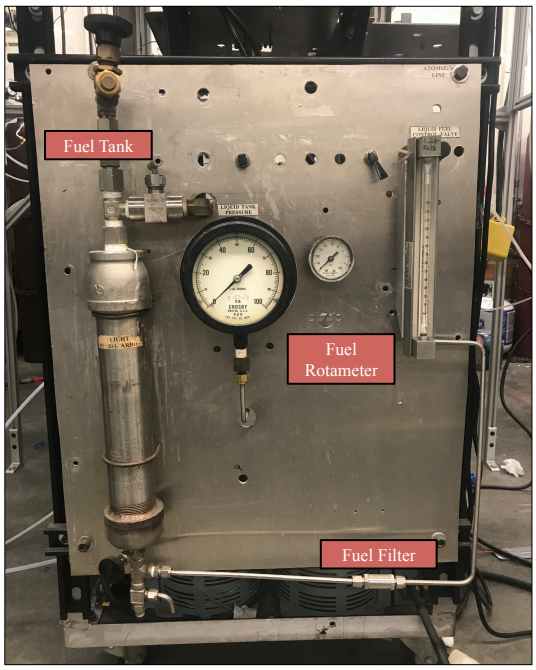

Figure A.2: Fuel tank used for handling fuel and rotameter utilized to vary fuel mass flow rate in the experiments for liquid fuels.

A.3.1 Iso-octane

Table A.3: Calibration data for iso-octane

Pressure [$psig$]	60
Density [kg/m^3]	680

Rotameter Setting	**time [s]**	**Volume [mL]**		**Mass Flow Rate [g/s]**	
		Trial 1	Trial 2	Trial 1	Trial 2
0	300	2.2	2	0.003	0.003
10	300	7.2	7.8	0.017	0.014
20	600	27.0	27.0	0.030	0.030
30	600	43.0	43.2	0.049	0.048
40	600	62.5	63.0	0.074	0.075

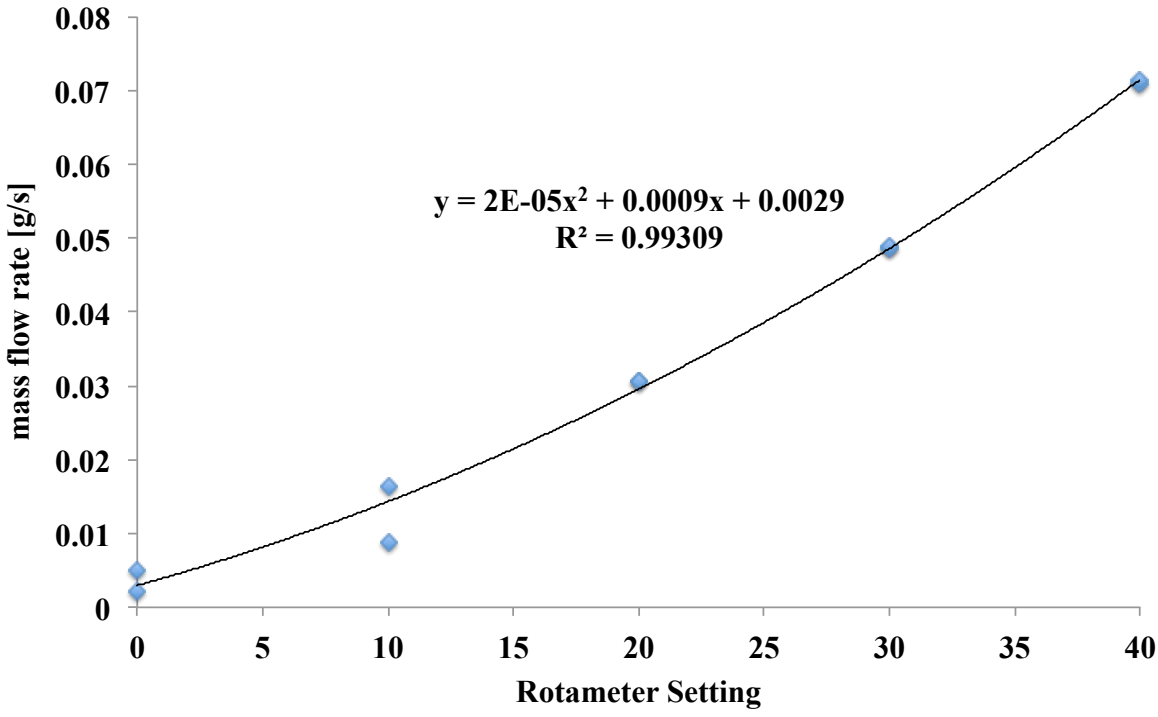

Figure A.3: Iso-octane calibration curve

A.3.2 Octane

Table A.4: Octane calibration curve

Pressure [$psig$]	60
Density [kg/m^3]	696

Rotameter Setting	**Time [s]**	**Flow Rate [mL/s]**		**Mass Flow Rate [g/s]**	
		Trial 1	Trial 2	Trial 1	Trial 2
0	300	2.200	2.200	0.005	0.005
10	300	14.400	7.200	0.017	0.017
20	600	26.500	26.200	0.031	0.030
30	600	39.500	39.900	0.046	0.046
40	600	57.800	59.800	0.067	0.069
50	600	85.800	85.800	0.100	0.100

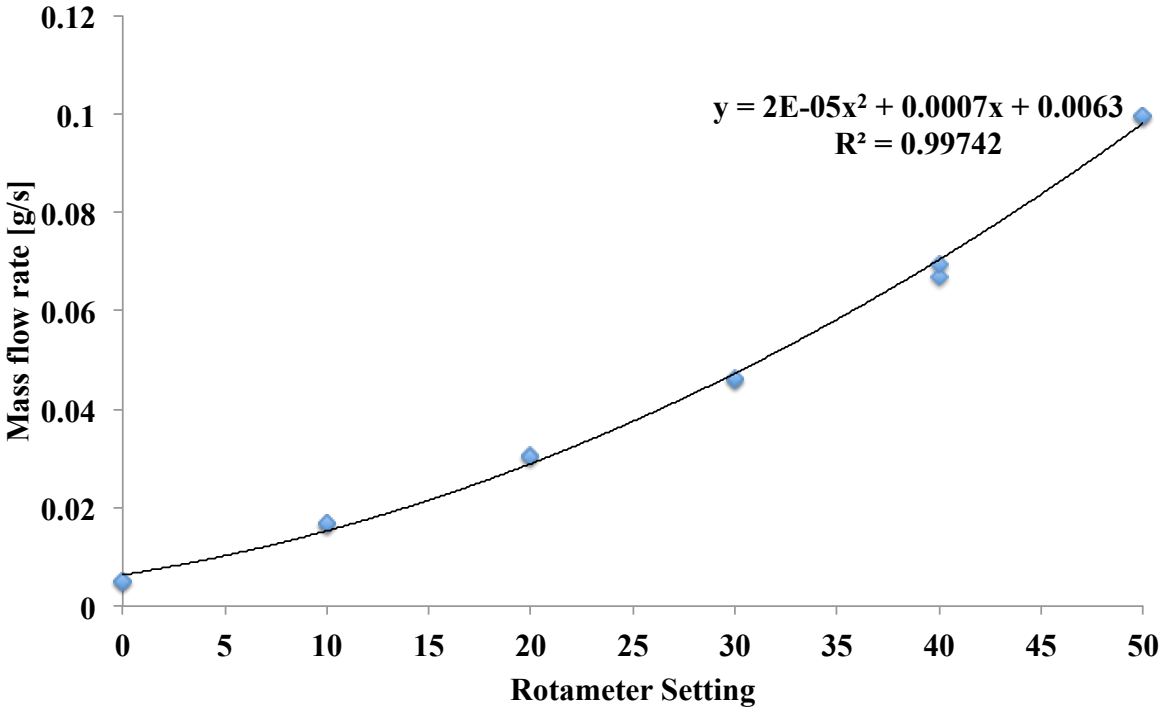

Figure A.4: Octane calibration curve

A.3.3 Hexane

Table A.5: Hexane calibration curve

Pressure [$psig$]	60
Density [kg/m^3]	654

Rotameter Setting	**Time [s]**	**Flow Rate [mL/s]**		**Mass Flow Rate [g/s]**	
		Trial 1	Trial 2	Trial 1	Trial 2
0	600	6.800	6.800	0.007	0.007
10	600	21.000	21.000	0.023	0.023
20	600	35.800	35.000	0.039	0.038
30	600	71.100	71.700	0.077	0.078
40	600	101.000	101.000	0.110	0.110

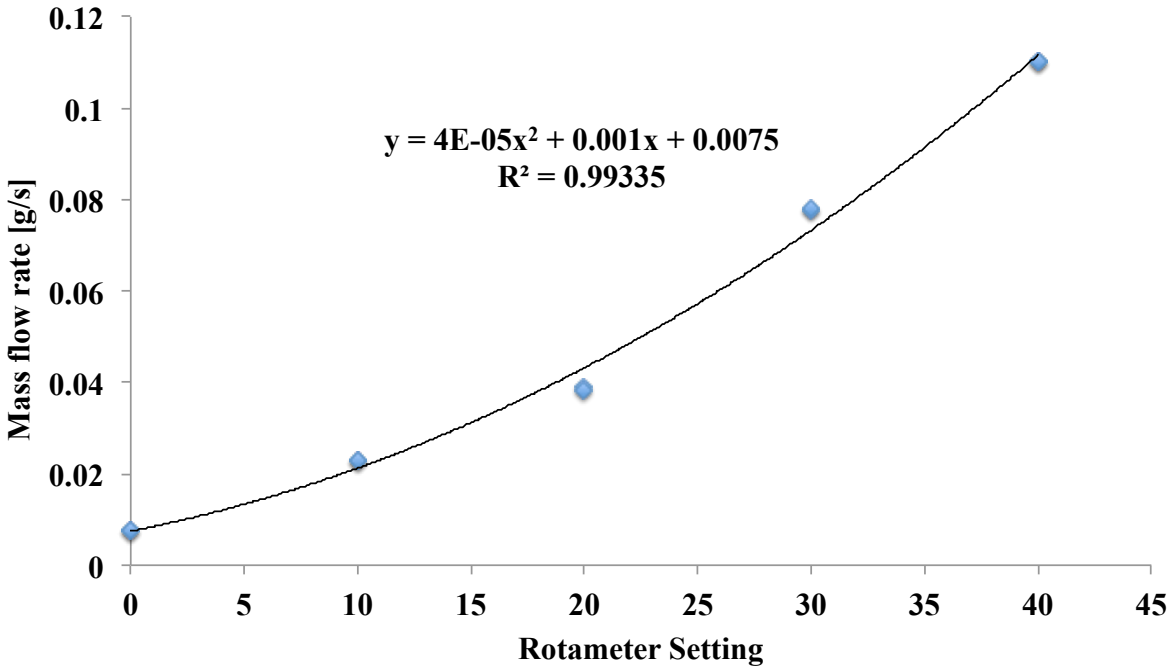

Figure A.5: Hexane calibration curve

A.3.4 Cyclo-hexane

Table A.6: Cyclo-hexane calibration curve

Pressure[*psig*]	60
Density [kg/m^3]	768

Rotameter Setting	**Time [s]**	**Flow Rate [mL/s]**		**Mass Flow Rate [g/s]**	
		Trial 1	Trial 2	Trial 1	Trial 2
0	300	1.280	1.300	0.003	0.003
10	300	4.300	4.200	0.011	0.011
20	600	16.900	17.000	0.022	0.022
30	600	27.000	27.500	0.035	0.035
40	600	37.600	38.200	0.048	0.049
50	600	51.700	52.500	0.066	0.067

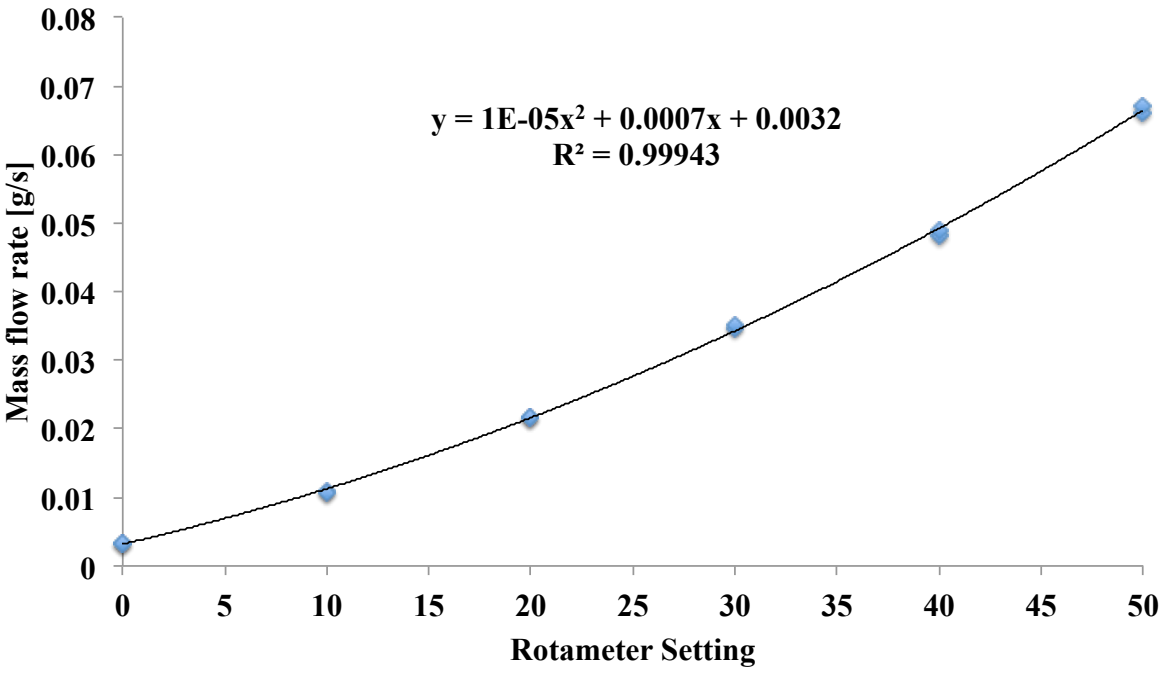

Figure A.6: Cyclo-hexane calibration curve

A.3.5 Toluene

Table A.7: Toluene calibration curve

Pressure[*psig*]	60
Density [kg/m^3]	860

Rotameter Setting	**Time [s]**	**Flow Rate [mL/s]**		**Mass Flow Rate [g/s]**	
		Trial 1	Trial 2	Trial 1	Trial 2
0	600	3.600	3.800	0.005	0.005
10	600	12.400	13.000	0.018	0.019
20	600	23.500	23.600	0.034	0.034
30	600	35.100	35.000	0.050	0.050
40	600	52.000	52.900	0.075	0.076
50	600	71.000	71.000	0.102	0.102

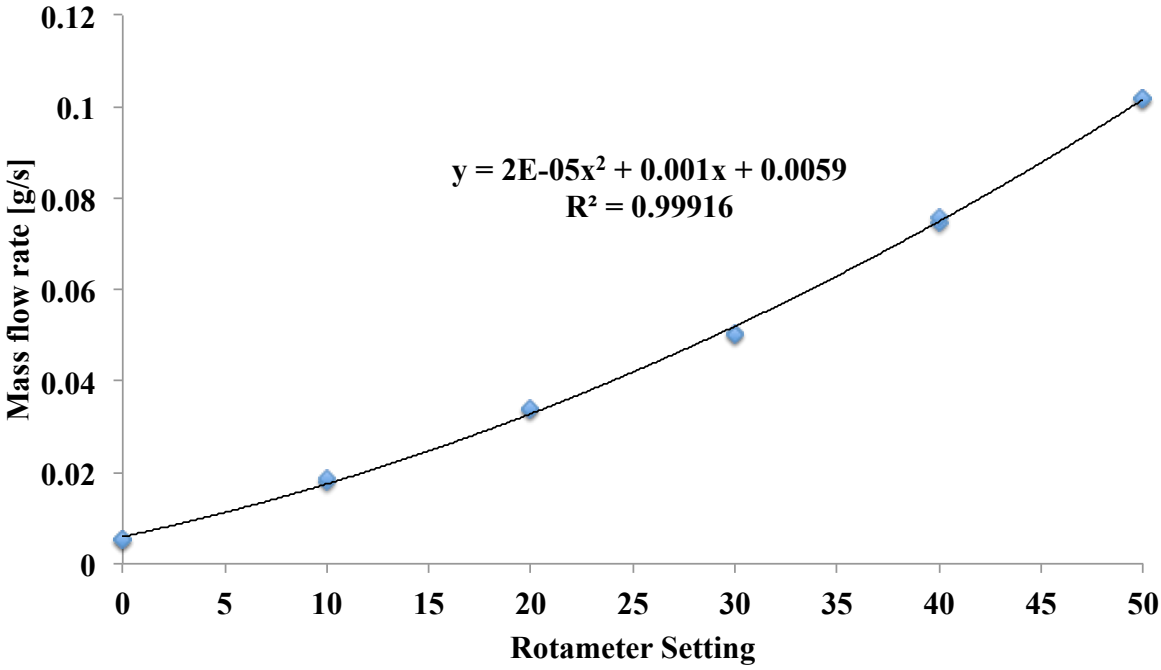

Figure A.7: Toluene calibration curve

A.3.6 135-TMB

Table A.8: Toluene calibration data

Pressure [$psig$]	60				
Density [kg/m^3]	856				
Rotameter Setting	**Time [s]**	**Flow Rate [mL/s]**		**Mass Flow Rate [g/s]**	
		Trial 1	Trial 2	Trial 1	Trial 2
0	600	3.200	3.100	0.005	0.004
10	600	11.500	11.200	0.016	0.016
20	600	22.000	21.500	0.031	0.031
30	600	32.000	31.500	0.046	0.045
40	600	45.400	45.200	0.065	0.064
50	600	62.500	63.000	0.089	0.090

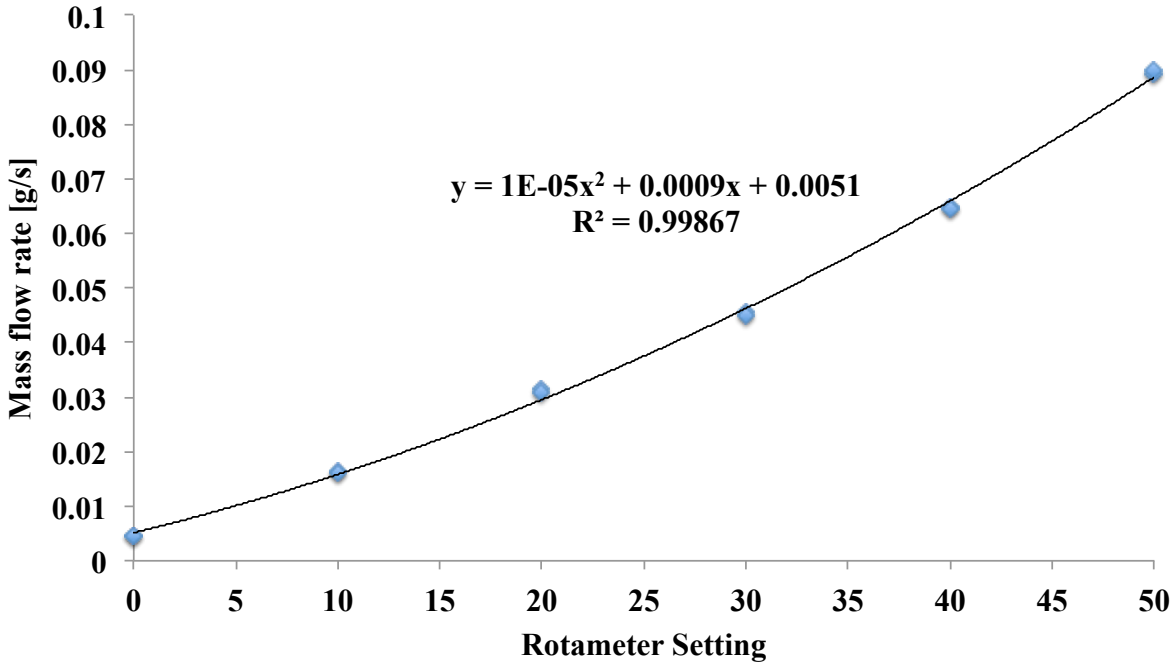

Figure A.8: 135-TMB calibration curve

A.3.7 Methane

Table A.9: Methane calibration data

Pressure [psig]	30
Density [kg/m^3]	0.66

Rotameter Setting	**Time [s]**		**Average Time [s]**	**Mass Flow Rate [g/s]**
	Trial 1	Trial 2		
2	117	116	116.5	0.0153
4	52	52	52.0	0.0352
6	33	33	33.2	0.0559
8	24	24	24.2	0.0766
10	19.31	19.29	19.3	0.0970

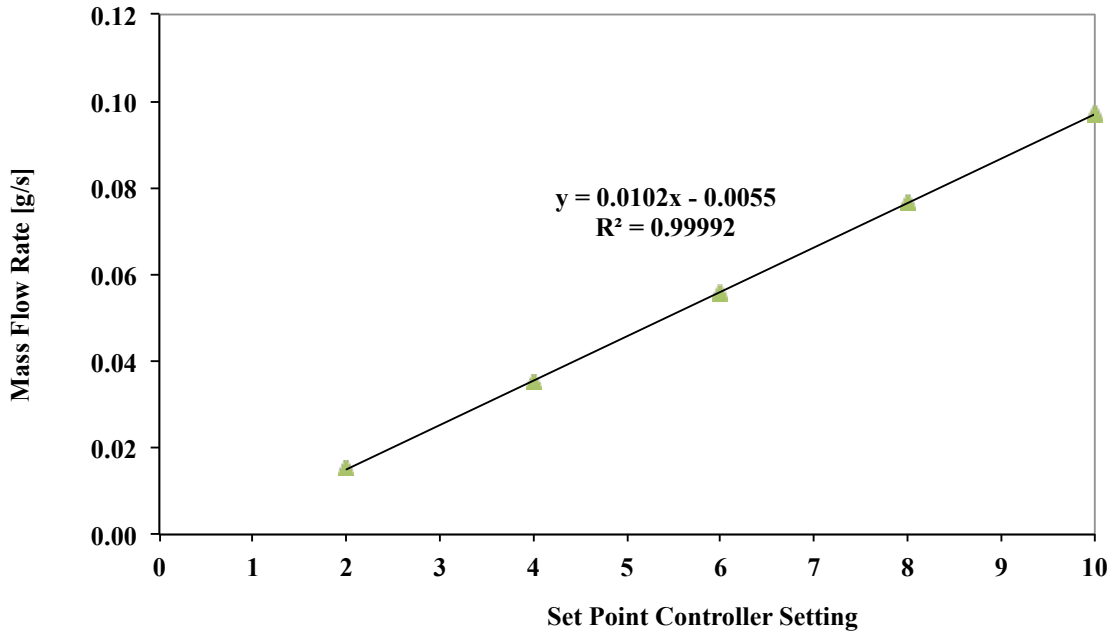

Figure A.9: Methane calibration curve

A.3.8 Air

Table A.10: First stage air rotamer calibration data

1st Stage Air	
Pressure [psig]	30
Density [kg/m^3]	1.2

Rotameter Setting	**Time [s]**		**Average Time [s]**	**Flow Rate [scfm]**
	Trial 1	Trial 2		
0	0	0	0.0	0.00
20	111	112	111.5	0.54
30	74	74	74.0	0.81
40	60	60	60.0	1.00

Table A.11: Second stage air rotamer calibration data

2nd Stage Air	
Pressure [psig]	30
Density [kg/m^3]	1.2

Rotameter Setting	**Time [s]**		**Average Time [s]**	**Flow Rate [scfm]**
	Trial 1	Trial 2		
0	0	0	0.0	0.00
20	128	129	128.5	0.47
30	90	90	90.0	0.67
40	70	70	70.0	0.86
50	60	61	60.5	0.99

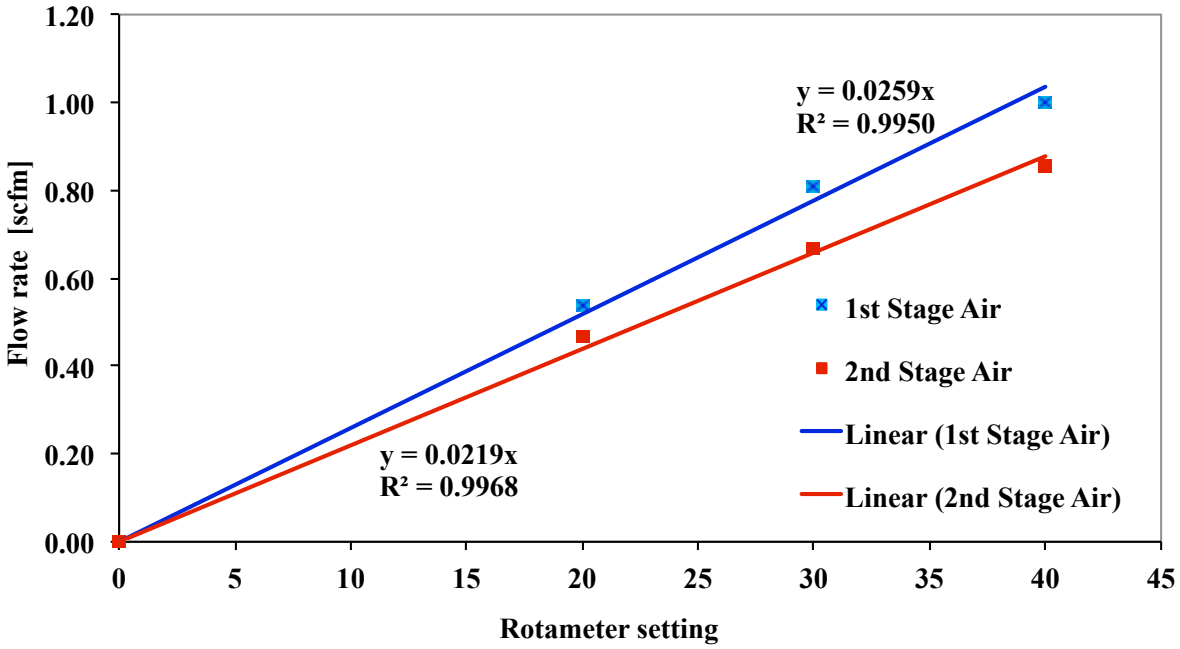

Figure A.10: 1^{st} and 2^{nd} stage air calibration curves.

Table A.12: Atomizor air rotamer calibration data

Atomizer Air

Pressure [psig]	48
Density [kg/m^3]	1.2

Rotameter Setting	**Time [s]**		**Average Time [s]**	**Flow Rate [scfm]**
	Trial 1	Trial 2		
0	0	0	0.0	0.000
5	138	142	140.0	0.043
10	120	121	120.5	0.100
15	147	149	148.0	0.162
20	107	107	107.0	0.224
25	83	83	83.0	0.289

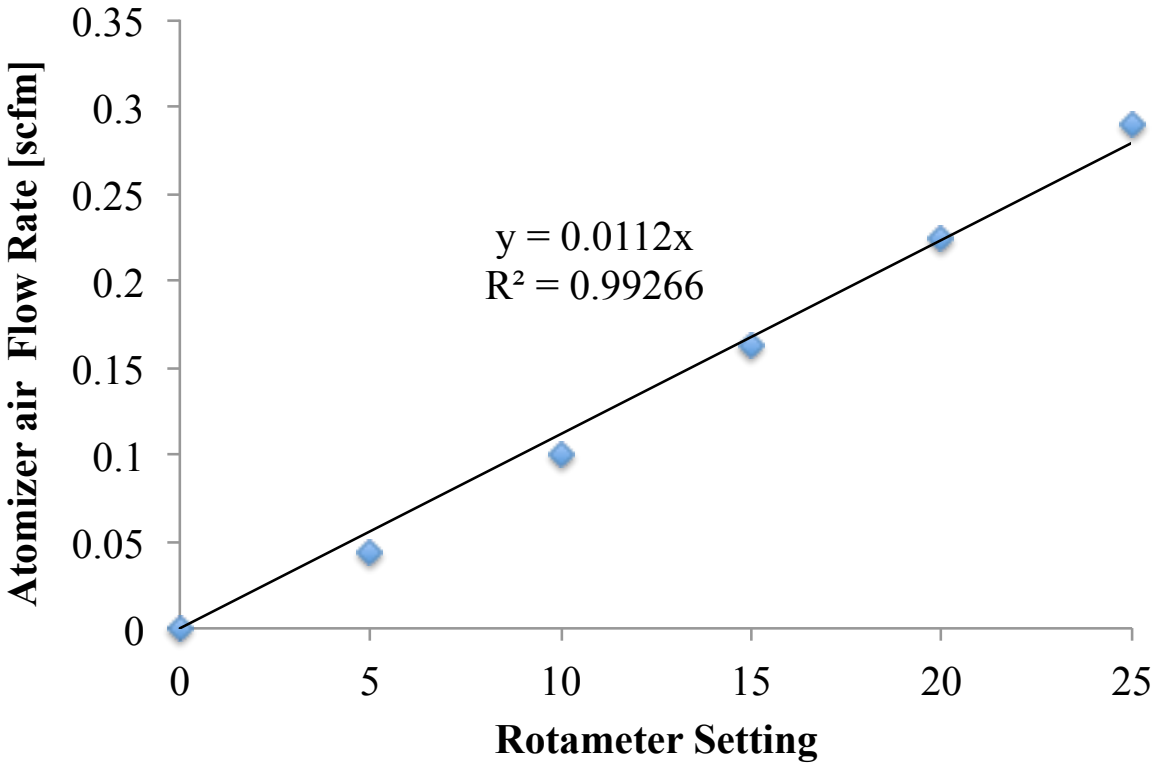

Figure A.11: Atomizor air calibration curves.

Appendix B

DETAILED EXPERIMENTAL DATA

B.1 NO_x *Experiments*

This section includes all the experimental data taken. The gas concentration data have been corrected for instrument drift in zero and span. In the table below, $\dot{m}_{air}$ is the mass flow of air, $\dot{m}_{Fuel}$ is the mass flow rate of fuel, $T_{R,raw}$ is the raw thermocouple temperature measured, $T_{R,cor}$ is the corrected temperature, T_P is the pre-mixed fluid temperature before it enters the reactor, ϕ_{gas} is the fuel-air equivalence ratio calculated using CO, CO_2, and O_2 measured using gas analyzers, and ϕ_{flow} is the fuel-air equivalence ratio calculated using the rotameters.

Fuel	Test Date	$\dot{m}_{air}$ [g/s]	$\dot{m}_{Fuel}$ [g/s]	$T_{R,raw}$ [C]	$T_{R,cor}$ [K]	T_P [C]	ϕ_{gas}	ϕ_{flow}	NO_x *dry* (ppm,Actual O_2)	NO_x *dry* (ppm,15% O_2)	CO [%,dry]	CO_2 [%,dry]	O_2 [%,dry]
CH4	10/22/15	1.070	0.045	1485	1800	320	0.700	0.719	10.20	4.28	0.106	7.78	6.79
CH4	10/22/15	1.070	0.045	1485	1800	320	0.700	0.719	10.55	4.40	0.134	7.82	6.69
CH4	12/3/15	1.070	0.045	1485	1800	336	0.691	0.729	10.59	4.50	0.315	7.27	6.94
CH4	12/3/15	1.070	0.045	1485	1800	336	0.676	0.732	10.40	4.38	0.335	7.30	6.84
Isooctane	10/26/15	1.056	0.046	1390	1700	330	0.626	0.685	6.54	3.11	0.26	8.58	8.45
Isooctane	10/26/15	1.054	0.051	1485	1800	332	0.688	0.765	13.04	5.63	0.290	9.52	7.17
Isooctane	10/26/15	1.056	0.046	1578	1900	336	0.756	0.849	24.17	9.41	0.414	10.49	5.67

Isooctane	12/4/15	1.056	0.046	1390	1700	333	0.600	0.685	7.38	3.56	0.414	8.32	7.88
Isooctane	12/4/15	1.053	0.051	1485	1801	336	0.662	0.765	14.50	6.66	0.490	8.85	6.90
Isooctane	12/4/15	1.052	0.057	1580	1902	341	0.731	0.856	26.88	10.70	0.573	9.25	6.44
Isooctane	12/10/15	1.051	0.052	1485	1800	338	0.666	0.783	14.36	6.22	0.432	8.65	7.22
Isooctane	12/10/15	1.056	0.042	1297	1601	332	0.539	0.625	3.82	2.08	0.434	7.02	10.02
Isooctane	12/10/15	1.050	0.038	1172	1468	328	0.488	0.564	1.71	1.02	0.742	5.81	11.39
Isooctane	12/10/15	Blowout	Blowout	1072	1362	Blowout	Blowout	Blowout	Blowout	Blowout	Blowout	Blowout	Blowout
Isooctane	6/6/16	1.054	0.048	1486	1801	327	0.684	0.717	14.25	6.07	0.406	8.98	6.98
Isooctane	6/6/16	1.056	0.039	1295	1599	326	0.552	0.58	3.40	1.84	0.389	7.32	9.97
Isooctane	6/6/16	1.052	0.033	1194	1492	320	0.497	0.499	1.48	0.89	0.63	6.13	11.02
Isooctane	6/6/16	Blowout	Blowout	1180	1477	Blowout	Blowout	Blowout	Blowout	Blowout	Blowout	Blowout	Blowout
Toluene	12/7/15	1.056	0.053	1391	1701	332	0.583	0.671	10.03	4.96	0.511	8.87	8.92
Toluene	12/7/15	1.056	0.060	1485	1801	336	0.652	0.757	19.25	8.54	0.650	9.74	7.55
Toluene	12/7/15	1.056	0.065	1580	1902	341	0.712	0.835	33.94	13.82	0.839	10.50	6.34
Toluene	12/7/15	1.058	0.049	1281	1583	327	0.523	0.615	4.51	2.52	0.548	7.93	10.19
Toluene	12/7/15	1.052	0.044	1200	1498	327	0.491	0.567	2.50	1.50	0.688	7.24	10.90
Toluene	12/7/15	Blowout	Blowout	1056	1345	Blowout	Blowout	Blowout	Blowout	Blowout	Blowout	Blowout	Blowout
Toluene	10/29/15	1.056	0.053	1390	1699	330	0.612	0.671	9.59	4.65	0.312	10.15	8.67
Toluene	10/29/15	1.056	0.058	1486	1801	334	0.684	0.743	18.87	8.10	0.383	11.25	7.09
Toluene	10/29/15	1.056	0.063	1578	1899	339	0.746	0.803	32.87	13.00	0.616	12.21	5.90

Toluene	6/9/16	1.056	0.050	1390	1700	327	0.568	0.630	9.98	4.98	0.470	8.52	9.02
Toluene	6/9/16	1.058	0.045	1275	1578	325	0.513	0.576	4.11	2.27	0.498	7.63	10.16
Toluene	6/9/16	1.052	0.042	1200	1498	322	0.478	0.541	2.25	1.35	0.640	7.00	11.06
Toluene	6/9/16	Blowout	Blowout	1161	1457	Blowout	Blowout	Blowout	Blowout	Blowout	Blowout	Blowout	Blowout
135-TMB	10/28/15	1.055	0.046	1390	1700	329	0.633	0.600	9.12	4.19	0.348	9.79	8.01
135-TMB	10/28/15	1.054	0.051	1486	1801	333	0.673	0.659	18.58	8.13	0.415	10.92	7.36
135-TMB	10/28/15	1.052	0.055	1580	1902	335	0.757	0.719	33.25	12.75	0.553	11.94	5.43
135-TMB	12/11/15	1.055	0.047	1390	1700	333	0.600	0.611	10.20	5.01	0.621	8.66	8.83
135-TMB	12/11/15	1.054	0.052	1486	1801	336	0.658	0.675	18.97	8.44	0.663	9.40	7.57
135-TMB	12/11/15	1.051	0.056	1579	1901	341	0.713	0.730	33.10	13.60	0.814	10.10	6.47
135-TMB	12/11/15	1.056	0.042	1302	1606	330	0.539	0.550	5.65	3.11	0.713	7.73	9.98
135-TMB	12/11/15	1.056	0.039	1201	1499	328	0.499	0.501	2.64	1.59	0.882	6.92	10.89
135-TMB	12/11/15	Blowout	Blowout	1110	1402	Blowout	Blowout	Blowout	Blowout	Blowout	Blowout	Blowout	Blowout
135-TMB	1/12/16	1.056	0.047	1390	1700	334	0.589	0.610	9.95	4.91	0.630	8.59	8.89
135-TMB	1/12/16	1.053	0.052	1486	1801	336	0.647	0.675	19.68	8.98	0.670	9.40	7.91
135-TMB	1/12/16	1.051	0.056	1581	1902	341	0.717	0.730	34.35	13.85	0.849	10.20	6.19
135-TMB	1/12/16	1.055	0.042	1286	1589	333	0.530	0.540	4.86	2.58	0.755	7.61	10.26
135-TMB	1/12/16	1.056	0.038	1180	1476	329	0.476	0.492	2.15	1.26	0.966	6.53	11.48
135-TMB	1/12/16	Blowout	Blowout	1111	1403	Blowout	Blowout	Blowout	Blowout	Blowout	Blowout	Blowout	Blowout

n-Octane	11/3/15	1.059	0.043	1390	1700	328	0.613	0.614	7.57	3.62	0.261	8.25	8.53
n-Octane	11/3/15	1.059	0.047	1486	1801	331	0.680	0.668	15.07	6.46	0.323	9.12	7.08
n-Octane	11/3/15	1.059	0.052	1581	1903	336	0.756	0.738	26.39	10.13	0.434	9.92	5.46
n-Octane	12/30/15	1.056	0.043	1390	1700	333	0.598	0.616	7.55	3.63	0.341	7.64	8.57
n-Octane	12/30/15	1.056	0.048	1485	1801	338	0.660	0.685	15.37	6.66	0.406	8.35	7.21
n-Octane	12/30/15	1.052	0.054	1579	1901	342	0.726	0.772	28.66	11.54	0.588	9.22	6.17
n-Octane	12/30/15	1.058	0.038	1287	1590	333	0.504	0.539	3.59	2.17	0.386	6.71	11.09
n-Octane	12/30/15	1.060	0.033	1200	1498	328	0.455	0.471	1.67	1.16	0.547	5.96	12.40
n-Octane	12/30/15	Blowout	Blowout	1036	1323	Blowout	Blowout	Blowout	Blowout	Blowout	Blowout	Blowout	Blowout
n-Octane	6/7/16	1.056	0.036	1390	1700	326	0.594	0.54	6.49	3.22	0.328	7.90	8.94
n-Octane	6/7/16	1.057	0.032	1285	1588	325	0.53	0.479	3.07	1.71	0.36	6.94	10.30
n-Octane	6/7/16	1.053	0.030	1205	1503	320	0.494	0.446	1.44	0.85	0.496	6.13	10.82
n-Octane	6/7/16	Blowout	Blowout	1130	1424	Blowout	Blowout	Blowout	Blowout	Blowout	Blowout	Blowout	Blowout
n-Hexane	10/30/15	1.056	0.046	1391	1700	325	0.622	0.665	6.86	3.24	0.187	8.40	8.36
n-Hexane	10/30/15	1.055	0.050	1486	1801	328	0.696	0.725	14.18	6.03	0.300	9.53	6.96
n-Hexane	10/30/15	1.052	0.056	1581	1902	334	0.764	0.810	26.78	10.33	0.434	10.40	5.53
cyclo-Hexane	12/2/15	1.054	0.047	1390	1699	330	0.659	0.663	8.09	3.69	0.277	9.71	7.89
cyclo-Hexane	12/2/15	1.053	0.053	1486	1801	332	0.738	0.740	16.55	6.69	0.378	10.95	6.22
cyclo-Hexane	12/2/15	1.051	0.057	1581	1903	336	0.793	0.809	30.31	11.45	0.551	12.03	5.19
cyclo-Hexane	12/8/15	1.054	0.046	1390	1700	333	0.599	0.642	7.84	3.77	0.375	8.13	8.58

cyclo-Hexane	12/8/15	1.052	0.051	1485	1801	337	0.669	0.718	15.50	6.68	0.457	8.87	7.14
cyclo-Hexane	12/8/15	1.050	0.055	1579	1901	342	0.730	0.777	27.59	10.94	0.625	9.61	5.95
cyclo-Hexane	2/8/16	1.057	0.045	1389	1699	333	0.592	0.630	6.69	3.21	0.342	7.29	8.57
cyclo-Hexane	2/8/16	1.050	0.040	1289	1592	332	0.532	0.560	3.62	1.99	0.399	7.13	10.12
cyclo-Hexane	2/8/16	1.058	0.037	1170	1466	328	0.472	0.520	1.32	0.82	0.613	6.01	11.40
cyclo-Hexane	2/8/16	Blowout	Blowout	1020	1307	Blowout	Blowout	Blowout	Blowout	Blowout	Blowout	Blowout	Blowout
FT-Natural Gas	12/14/15	1.054	N/A	1390	1699	332	0.560	N/A	7.58	3.68	0.346	7.77	8.69
FT-Natural Gas	12/14/15	1.053	N/A	1485	1801	336	0.610	N/A	14.04	6.22	0.395	8.50	7.51
FT-Natural Gas	12/14/15	1.051	N/A	1579	1901	340	0.685	N/A	27.80	11.24	0.558	9.19	6.23
FT-Natural Gas	12/14/15	1.055	N/A	1310	1614	332	0.507	N/A	4.36	2.32	0.325	7.08	9.78
FT-Natural Gas	12/14/15	1.058	N/A	1217	1515	328	0.494	N/A	2.64	1.47	0.432	6.92	10.26
FT-Natural Gas	12/14/15	Blowout	Blowout	1031	1318	Blowout	Blowout	Blowout	Blowout	Blowout	Blowout	Blowout	Blowout
FT-Natural Gas	1/7/16	1.054	N/A	1390	1699	332	0.540	N/A	7.04	3.52	0.348	7.77	9.03
FT-Natural Gas	1/7/16	1.053	N/A	1485	1800	336	0.607	N/A	14.38	6.46	0.407	8.57	7.70
FT-Natural Gas	1/7/16	1.051	N/A	1580	1902	341	0.697	N/A	28.77	11.42	0.580	9.41	5.97
FT-Natural Gas	1/7/16	1.058	N/A	1288	1591	332	0.499	N/A	3.47	1.88	0.415	6.88	9.96
FT-Natural Gas	1/7/16	1.058	N/A	1192	1489	328	0.454	N/A	1.49	0.88	0.612	5.98	10.88
FT-Natural Gas	1/7/16	Blowout	Blowout	1042	1330	Blowout	Blowout	Blowout	Blowout	Blowout	Blowout	Blowout	Blowout
HRJ-Camelina	12/15/17	1.054	N/A	1391	1701	330	0.560	N/A	7.85	3.76	0.354	7.64	8.54

HRJ-Camelina	12/15/17	1.053	N/A	1486	1801	336	0.620	N/A	14.67	6.48	0.420	8.43	7.48
HRJ-Camelina	12/15/17	1.051	N/A	1580	1902	340	0.682	N/A	26.29	10.62	0.569	9.07	6.22
HRJ-Camelina	12/15/17	1.055	N/A	1310	1615	332	0.488	N/A	4.17	2.37	0.380	6.97	10.47
HRJ-Camelina	12/15/17	1.058	N/A	1187	1484	328	0.435	N/A	1.69	1.07	0.663	5.83	11.54
HRJ-Camelina	12/15/17	Blowout	Blowout	1047	1335	Blowout	Blowout	Blowout	Blowout	Blowout	Blowout	Blowout	Blowout
HRJ-Camelina	1/5/16	1.055	N/A	1389	1699	334	0.560	N/A	7.89	4.11	0.372	7.84	9.53
HRJ-Camelina	1/5/16	1.053	N/A	1485	1800	338	0.629	N/A	15.72	7.21	0.447	8.64	7.97
HRJ-Camelina	1/5/16	1.051	N/A	1580	1902	344	0.698	N/A	30.50	12.11	0.616	9.34	5.96
HRJ-Camelina	1/5/16	1.055	N/A	1312	1617	335	0.495	N/A	4.29	2.41	0.392	7.11	10.38
HRJ-Camelina	1/5/16	1.058	N/A	1192	1489	328	0.456	N/A	1.58	0.93	0.615	6.11	10.85
HRJ-Camelina	1/5/16	Blowout	Blowout	1040	1328	Blowout	Blowout	Blowout	Blowout	Blowout	Blowout	Blowout	Blowout
Alcohol-based Jet	12/16/15	1.054	N/A	1389	1699	332	0.550	N/A	7.31	3.61	3.770	7.69	8.90
Alcohol-based Jet	12/16/15	1.053	N/A	1485	1800	336	0.616	N/A	13.81	6.12	0.433	8.38	7.51
Alcohol-based Jet	12/16/15	1.052	N/A	1580	1902	340	0.683	N/A	27.40	11.09	0.585	9.07	6.24
Alcohol-based Jet	12/16/15	1.056	N/A	1303	1607	332	0.497	N/A	4.08	2.23	0.419	6.90	10.06
Alcohol-based Jet	12/16/15	1.058	N/A	1187	1484	328	0.439	N/A	1.69	1.05	0.663	5.83	11.37
Alcohol-based Jet	12/16/15	Blowout	Blowout	1063	1352	Blowout	Blowout	Blowout	Blowout	Blowout	Blowout	Blowout	Blowout
Alcohol-based Jet	1/4/16	1.053	N/A	1389	1699	333	0.564	N/A	7.93	3.82	0.402	7.79	8.60
Alcohol-based Jet	1/4/16	1.052	N/A	1485	1800	338	0.632	N/A	14.90	6.67	0.477	8.57	7.65
Alcohol-based Jet	1/4/16	1.051	N/A	1580	1901	341	0.710	N/A	30.39	11.93	0.665	9.47	5.79

Alcohol-based Jet	1/4/16	1.054	N/A	1308	1613	333	0.514	N/A	4.59	2.42	0.431	7.07	9.67
Alcohol-based Jet	1/4/16	1.057	N/A	1193	1491	328	0.449	N/A	1.88	0.59	0.649	6.05	1.88
Alcohol-based Jet	1/4/16	Blowout	Blowout	1054	1343	Blowout	Blowout	Blowout	Blowout	Blowout	Blowout	Blowout	Blowout
HRJ-Tallow	12/17/15	1.053	N/A	1390	1700	331	0.558	N/A	7.55	3.67	0.360	7.70	8.70
HRJ-Tallow	12/17/15	1.053	N/A	1485	1800	337	0.617	N/A	14.36	6.33	0.426	8.44	7.46
HRJ-Tallow	12/17/15	1.051	N/A	1579	1901	342	0.692	N/A	27.06	10.73	0.577	9.12	5.94
HRJ-Tallow	12/17/15	1.056	N/A	1274	1577	332	0.480	N/A	3.13	1.78	0.399	6.77	10.48
HRJ-Tallow	12/17/15	1.056	N/A	1197	1494	325	0.443	N/A	1.66	1.04	0.560	6.14	11.51
HRJ-Tallow	12/17/15	Blowout	Blowout	1041	1329	Blowout	Blowout	Blowout	Blowout	Blowout	Blowout	Blowout	Blowout
HRJ-Tallow	1/11/16	1.054	N/A	1390	1700	334	0.565	N/A	6.80	3.30	0.350	7.58	8.71
HRJ-Tallow	1/11/16	1.052	N/A	1485	1800	337	0.620	N/A	13.97	6.10	0.387	8.30	7.31
HRJ-Tallow	1/11/16	1.051	N/A	1580	1901	342	0.693	N/A	26.33	10.59	0.559	9.39	6.16
HRJ-Tallow	1/11/16	1.056	N/A	1263	1565	332	0.473	N/A	2.89	1.64	0.464	6.46	10.50
HRJ-Tallow	1/11/16	1.056	N/A	1194	1492	328	0.440	N/A	1.51	0.94	0.639	5.89	11.39
HRJ-Tallow	1/11/16	Blowout	Blowout	1049	1338	Blowout	Blowout	Blowout	Blowout	Blowout	Blowout	Blowout	Blowout
n-Dodecane	1/14/16	1.055	N/A	1390	1699	335	0.558	N/A	7.10	3.46	0.377	7.74	8.72
n-Dodecane	1/14/16	1.053	N/A	1485	1801	336	0.621	N/A	14.30	6.31	0.437	8.54	7.46
n-Dodecane	1/14/16	1.051	N/A	1581	1902	340	0.704	N/A	27.55	10.95	0.609	9.37	5.98
n-Dodecane	1/14/16	1.056	N/A	1302	1606	333	0.504	N/A	3.85	2.08	0.411	7.02	9.94

n-Dodecane	1/14/16	1.056	N/A	1180	1478	329	0.445	N/A	1.57	0.96	0.601	6.01	11.25
n-Dodecane	1/14/16	Blowout	Blowout	1044	1332	Blowout	Blowout	Blowout	Blowout	Blowout	Blowout	Blowout	Blowout
n-Dodecane	1/15/16	1.054	N/A	1392	1701	334	0.553	N/A	7.02	3.42	0.340	7.68	8.74
n-Dodecane	1/15/16	1.052	N/A	1486	1801	340	0.625	N/A	14.01	6.11	0.405	8.52	7.31
n-Dodecane	1/15/16	1.051	N/A	1580	1902	346	0.689	N/A	26.84	10.72	0.563	9.16	6.06
n-Dodecane	1/15/16	1.056	N/A	1302	1606	333	0.490	N/A	3.40	1.90	0.391	6.92	10.32
n-Dodecane	1/15/16	1.056	N/A	1208	1506	330	0.437	N/A	1.53	0.97	0.569	6.00	11.56
n-Dodecane	1/15/16	Blowout	Blowout	1047	1335	Blowout	Blowout	Blowout	Blowout	Blowout	Blowout	Blowout	Blowout
Jet-A	11/18/15	1.061	N/A	1389	1699	328	0.581	N/A	7.72	3.89	0.299	8.36	9.16
Jet-A	11/18/15	1.054	N/A	1485	1801	333	0.668	N/A	15.43	6.64	0.378	9.28	7.13
Jet-A	11/18/15	1.052	N/A	1581	1903	336	0.745	N/A	28.55	11.01	0.472	10.24	5.52
Jet-A	11/18/15	Blowout	Blowout	1022	1309	Blowout	Blowout	Blowout	Blowout	Blowout	Blowout	Blowout	Blowout
Jet-A	11/19/15	1.054	N/A	1390	1700	330	0.602	N/A	8.65	3.98	0.347	7.87	8.01
Jet-A	11/19/15	1.048	N/A	1486	1801	334	0.670	N/A	13.84	5.78	0.414	8.69	6.69
Jet-A	11/19/15	1.054	N/A	1579	1901	338	0.740	N/A	23.32	8.90	0.574	9.36	5.35
Jet-A	11/19/15	1.055	N/A	1265	1567	336	0.535	N/A	3.30	1.11	0.417	7.20	3.30
Jet-A	11/19/15	1.056	N/A	1098	1390	317	0.456	N/A	1.09	0.33	0.758	11.80	1.00
Jet-A	11/19/15	Blowout	Blowout	1030	1317	Blowout	Blowout	N/A	Blowout	Blowout	Blowout	Blowout	Blowout
Jet-A+1% Cresol	11/20/15	1.056	N/A	1389	1698	330	0.580	N/A	6.80	3.42	0.286	8.55	9.12
Jet-A+1% Cresol	11/20/15	1.056	N/A	1485	1800	334	0.662	N/A	12.95	5.63	0.306	9.38	7.27

Jet-A+1% Cresol	11/20/15	1.053	N/A	1580	1901	337	0.726	N/A	25.10	10.04	0.432	10.23	6.07
Jet-A+1% Cresol	11/20/15	1.058	N/A	1260	1561	329	0.515	N/A	3.20	1.83	0.412	7.22	10.56
Jet-A+1% Cresol	11/20/15	1.060	N/A	1119	1412	325	0.455	N/A	1.48	0.90	0.760	5.47	11.18
Jet-A+1% Cresol	11/20/15	Blowout	Blowout	1037	1324	Blowout	Blowout	Blowout	Blowout	Blowout	Blowout	Blowout	Blowout
Jet-A+1% Cresol	11/24/15	1.056	N/A	1389	1698	333	0.5698	N/A	7.6	N/A	0.374	8.20	N/A
Jet-A+1% Cresol	11/24/15	1.053	N/A	1485	1801	337	0.611	N/A	16	N/A	0.471	8.76	N/A
Jet-A+1% Cresol	11/24/15	1.053	N/A	1580	1902	337	0.677	N/A	29.7	N/A	0.653	9.63	N/A
Jet-A+1% Cresol	11/24/15	1.058	N/A	1249	1550	329	0.487	N/A	2.81	N/A	0.51	6.79	N/A
Jet-A+1% Cresol	11/24/15	1.061	N/A	1083	1374	336	0.425	N/A	1.42	N/A	0.87	5.25	N/A
Jet-A+1% Cresol	11/24/15	Blowout	Blowout	1043	1331	Blowout	Blowout	Blowout	Blowout	Blowout	Blowout	Blowout	Blowout
Jet-A+5% Cresol	12/21/15	1.053	N/A	1390	1700	332	0.600	N/A	8.29	4.02	0.397	8.10	8.68
Jet-A+5% Cresol	12/21/15	1.052	N/A	1485	1801	336	0.630	N/A	15.86	6.93	0.477	8.85	7.34
Jet-A+5% Cresol	12/21/15	1.051	N/A	1580	1902	340	0.700	N/A	29.07	11.74	0.659	9.72	6.21
Jet-A+5% Cresol	12/21/15	1.056	N/A	1278	1580	329	0.487	N/A	3.80	2.24	0.452	7.13	10.85
Jet-A+5% Cresol	12/21/15	1.056	N/A	1184	1480	325	0.447	N/A	1.90	1.21	0.647	6.24	11.65
Jet-A+5% Cresol	12/21/15	Blowout	Blowout	1056	1345	Blowout	Blowout	Blowout	Blowout	Blowout	Blowout	Blowout	Blowout
Jet-A+5% Cresol	12/29/15	1.055	N/A	1390	1700	333	0.608	N/A	8.57	4.19	0.391	7.99	8.78
Jet-A+5% Cresol	12/29/15	1.052	N/A	1486	1801	337	0.665	N/A	16.51	7.24	0.477	8.85	7.39
Jet-A+5% Cresol	12/29/15	1.051	N/A	1580	1901	342	0.732	N/A	32.08	12.78	0.657	9.52	6.01

Jet-A+5% Cresol	12/29/15	1.056	N/A	1281	1584	333	0.533	N/A	4.08	2.03	0.439	7.10	9.02
Jet-A+5% Cresol	12/29/15	1.059	N/A	1189	1486	329	0.478	N/A	1.95	1.08	0.654	6.13	10.18
Jet-A+5% Cresol	12/29/15	Blowout	Blowout	1050	1339	Blowout	Blowout	Blowout	Blowout	Blowout	Blowout	Blowout	Blowout

B.2 Lean Flame Blowout

Resistance to lean-flame blowout (LFBO) of the fuels is studied by measuring the JSR temperature immediately prior to blowout. A low blowout temperature implies greater resistance to blowout, and thus, improved flame stability. This set of experiments is done by lowering the mass flow rate of the liquid fuel while the air flow rate is fixed. This procedure is done by carefully allowing the reactor to reach a steady temperature before fuel flow rate is reduced at each step. This method minimizes the influence of transient heating (from the more slowly cooling reactor walls) on blowout. This process continues until the flame can no longer be sustained.

The blowout temperature for all fuels is given in Figure B.1. Blowout tests are performed at least twice for each fuel on different days. The variation in LFBO measurements is plotted as error bars in Figure B.1.

It appears that 135-TMB tends to blowout at a significantly higher temperature compared to all other fuels. Based on these blowout temperature measurements, the renewable/alternative jet fuels appear to show slightly lower flame stability than jet-A. Cyclohexane has the lowest LFBO temperature among all fuels. The present study shows some differences to Blust's flame stability tests [8]. Blust measured the following pattern for blowout temperature in a toroidal JSR at a fixed residence time (5.3 ms): jet-A $<$ cyclohexane $<$ Toluene $<$ n-dodecane. Blowout tests by Vijlee [84] using a TSR showed little difference between flame stability of alternative jet fuels which is consistent with the findings of this study.

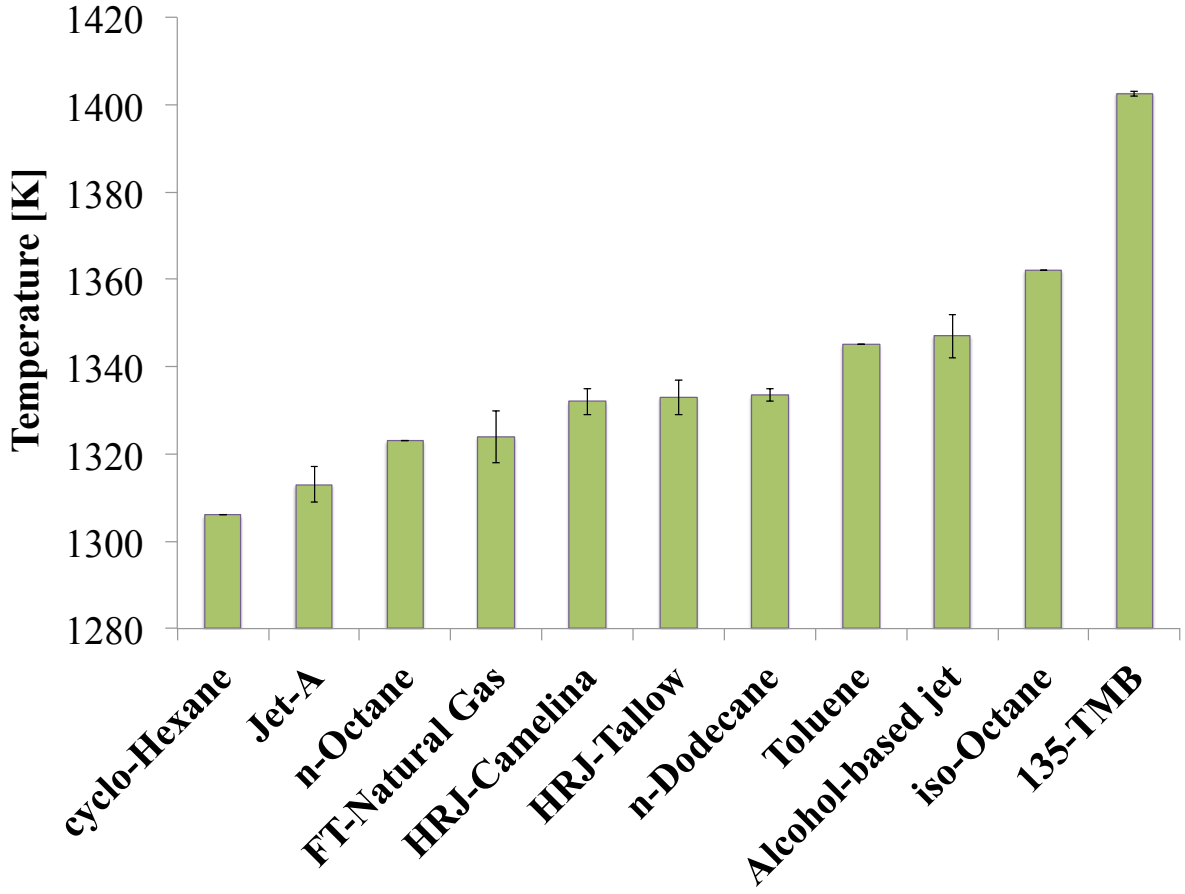

Figure B.1: Lean flame blowout temperature vs fuels with daily variation shown as error bars.

B.3 Fuel Oxygenates

Acceptable thermal stability requires that the alternative aviation fuels have very low oxygen content, which may increase the production cost of the bio-based fuels. Some oxygen functionalities may exhibit less thermal instability than others and may decrease soot tendency. Recent measurements at Washington State University [30] show that phenols are the most likely oxygenates remaining from fuel processing and that the phenolic concentrations in the fuels used in this study are low, below about 10 to 100 ppm by weight, depending on the fuel type.

A short set of experiments is conducted to ascertain the amount of oxygenate required to cause a measurable change in the soot threshold, NO_x, and LFBO. Table B.2 shows a summary of this result.

The oxygenate chosen is 2-methyl phenol (o-cresol). 1% by weight of this phenol in Jet-A produces a measurable 0.03±0.005 phi increase in the soot threshold. However, NO_x (at 1900K) and LFBO temperature also increase: respectively, 1.3± 4.7 ppmvd and 15±7 degrees C. Furthermore, tests at another lab indicate that 1% 2-methyl phenol in Jet-A leads to unacceptable fuel thermal stability [30].

	NO_x $[ppmv, dry, actual O_2]$			LFBO Temperature	Sooting Threshold
	1700 K	1800K	1900K	$[K]$	ϕ
Jet-A	8.2 ± 0.5	14.6± 0.8	25.9± 2.6	1313± 4	1.36± 0.2
Jet-A+1% O-Cresol	7.2± 0.4	14.5± 1.5	27.2± 2.1	1328± 3	1.39± 0.3
Jet-A+5% O-Cresol	8.4± 0.1	16.2± 0.3	30.6± 1.5	1342± 3	1.43± 0.5

Table B.2: NO_x, blowout temperature, and soothing threshold for JET-A and the mixture that contains 1% and 5% O-Cresol .

The addition of 1 and 5% of o-Cresol to Jet-A decreased the stability of the flame while it increased the the threshold at which flame starts to soot. NO_x does not show much variation when 1% of o-Cresol mixture is burnt in the JSR. However, using a mixture of 5% o-Cresol and Jet-A, NO_x emissions seem to be higher by about 2-20% from 1700K to 1900K compared to pure Jet-A.

Appendix C

CFD SUPPLEMENTARY PLOTS

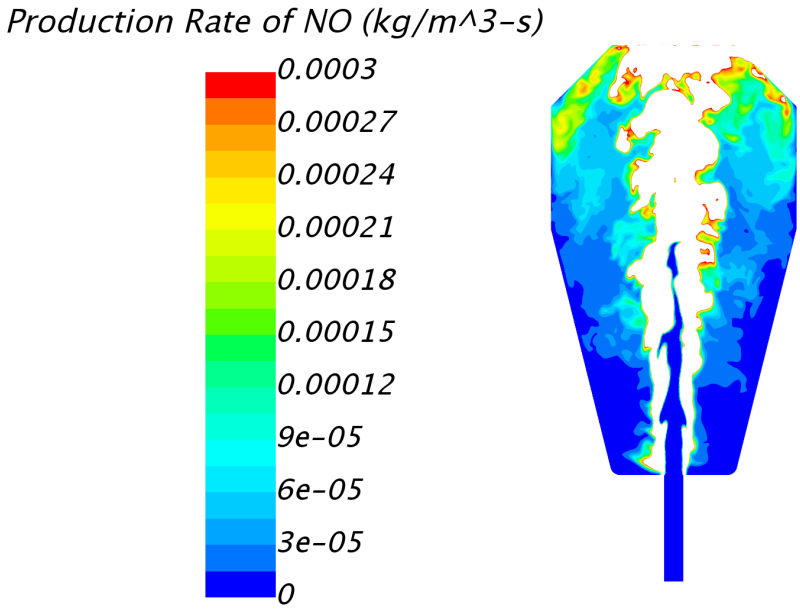

Figure C.1: ROP of NO for LES solution for combustion of hydrogen with NO_x chemistry. This plot have higher resolution in the recirculation zone while the values above the maximum value in the legend is cropped.

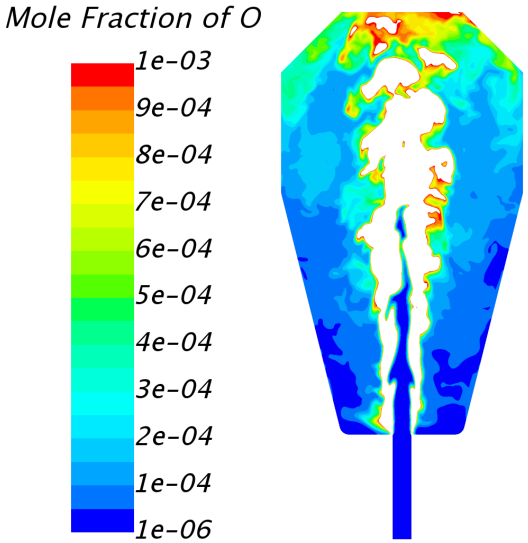

(a) CH_4 Mole Fraction

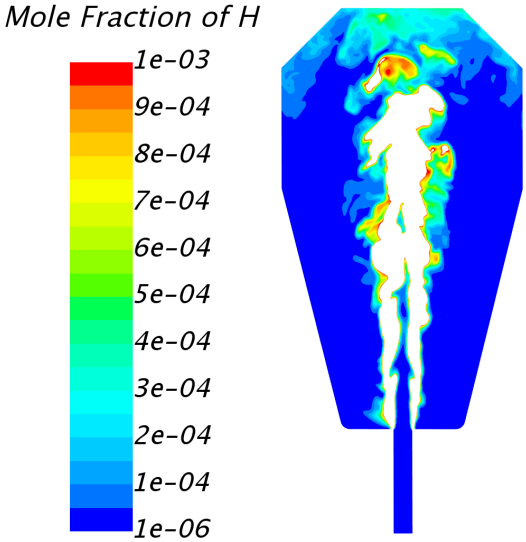

(b) CH Mole Fraction

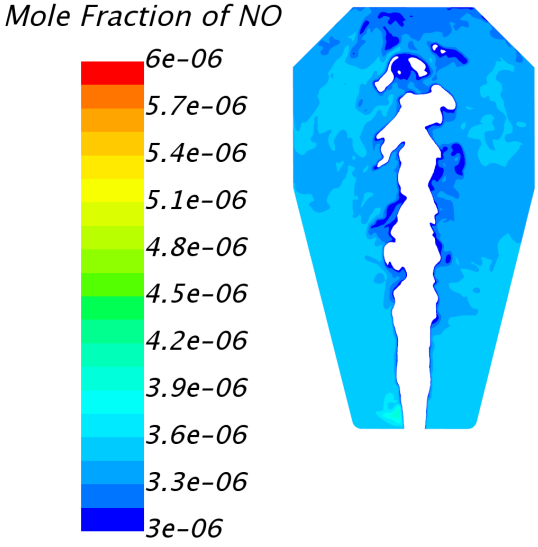

(c) NO Mole Fraction

Figure C.2: LES solution for combustion of hydrogen with NO_x chemistry. These plots have higher resolution in the recirculation zone while the values above the maximum value in the legend is cropped.

Appendix D

CRN SUPPLEMENTARY PLOTS

D.1 CRN Diagram

A CHEMKIN-PRO diagram of the 3-zone CRN is shown in Figure D.1. Note that two splitters are used to separate the flow entering PSR1 and PSR2 as well as the exiting flow from the recycling flow. A mixer is also used to combine the flow from PSR1 and PSR2 before they enter the PST. Either of the splitter or mixer have no effect on the thermodynamics or energy balance of the flow.

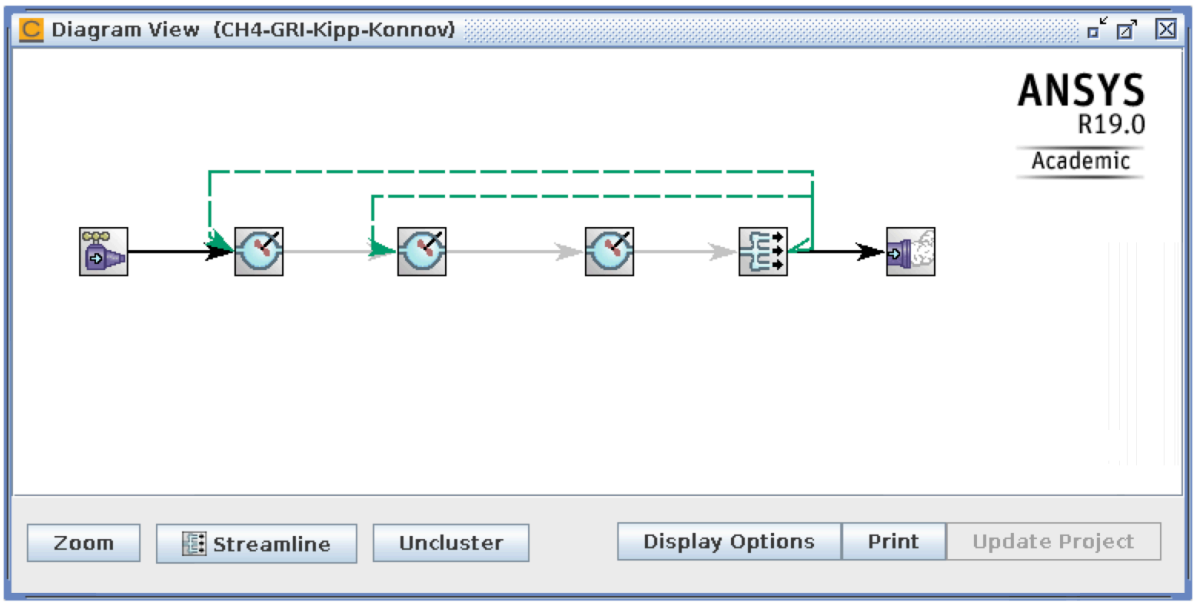

Figure D.1: CHEMKIN-PRO CRN diagram for the 3-zone configuration.

D.2 CH Pathway Analysis

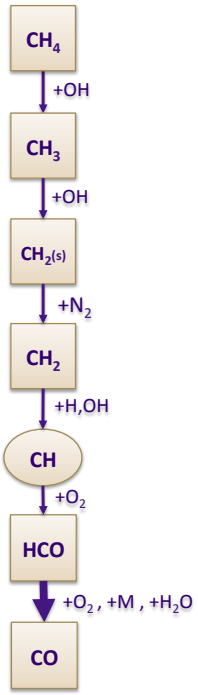

Figure D.2: CH pathway for methane

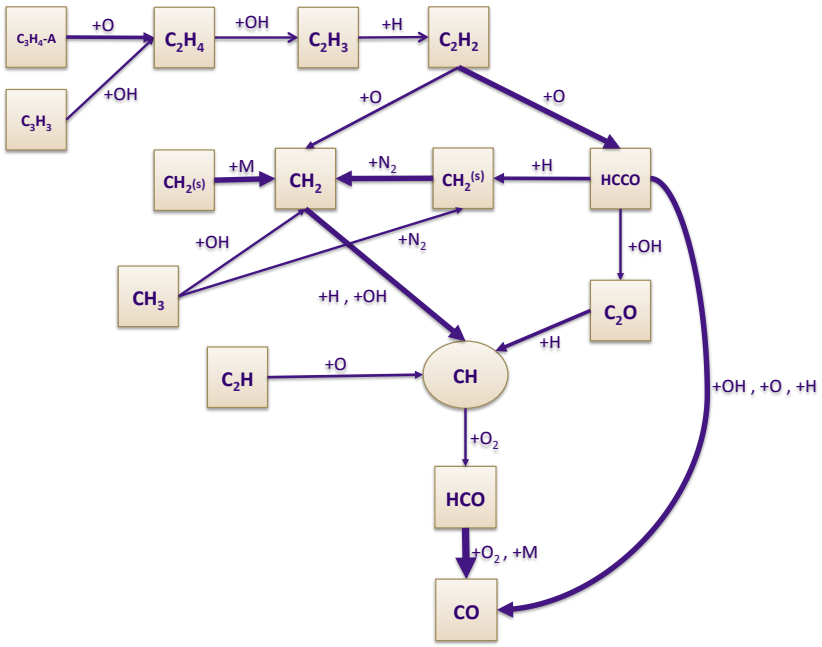

Figure D.3: CH pathway for isooctane

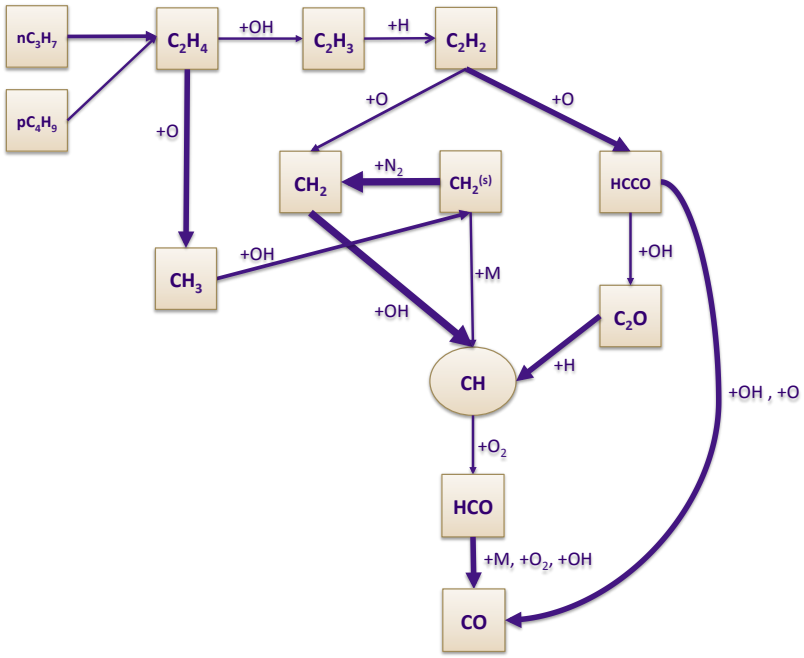

Figure D.4: CH pathway for n-octane

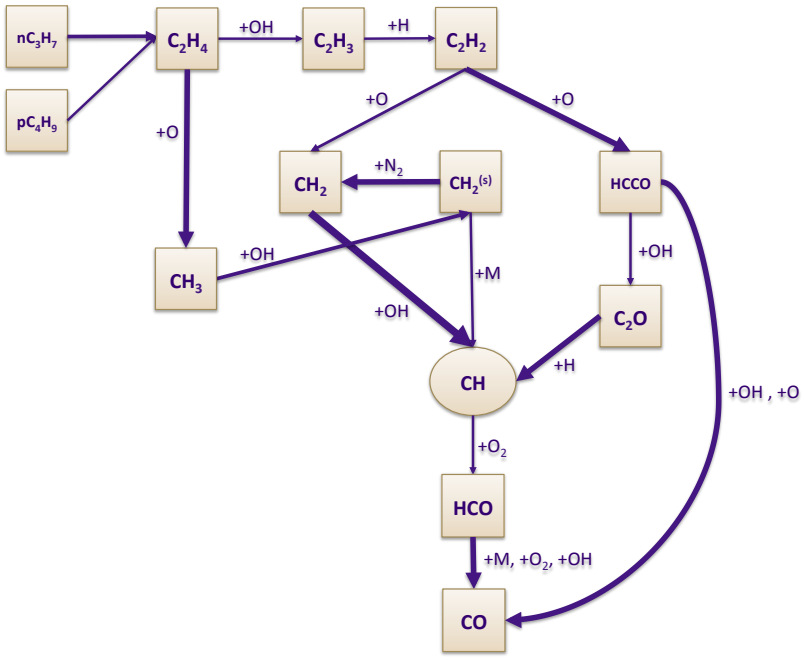

Figure D.5: CH pathway for n-dodecane

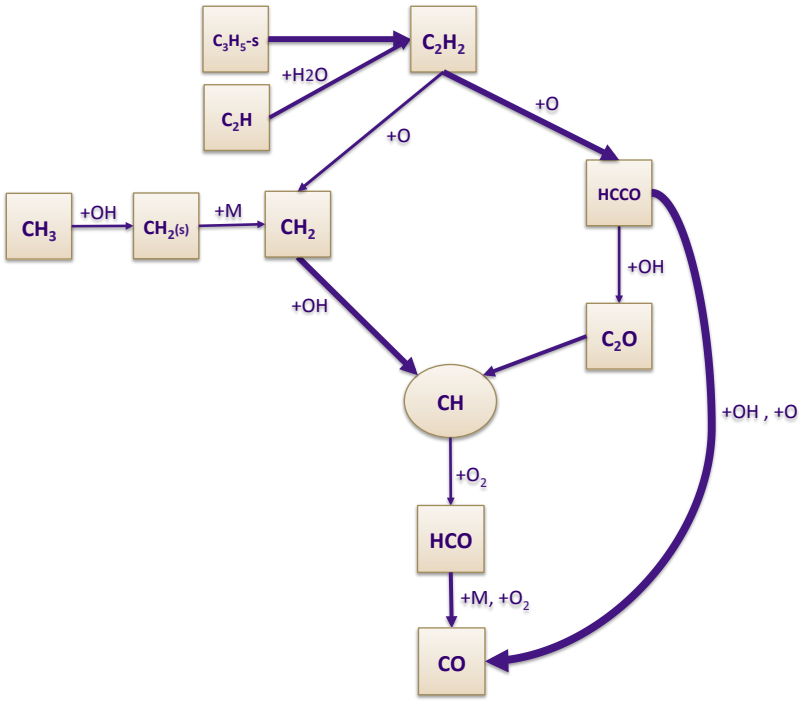

Figure D.6: CH pathway for 135-TMB

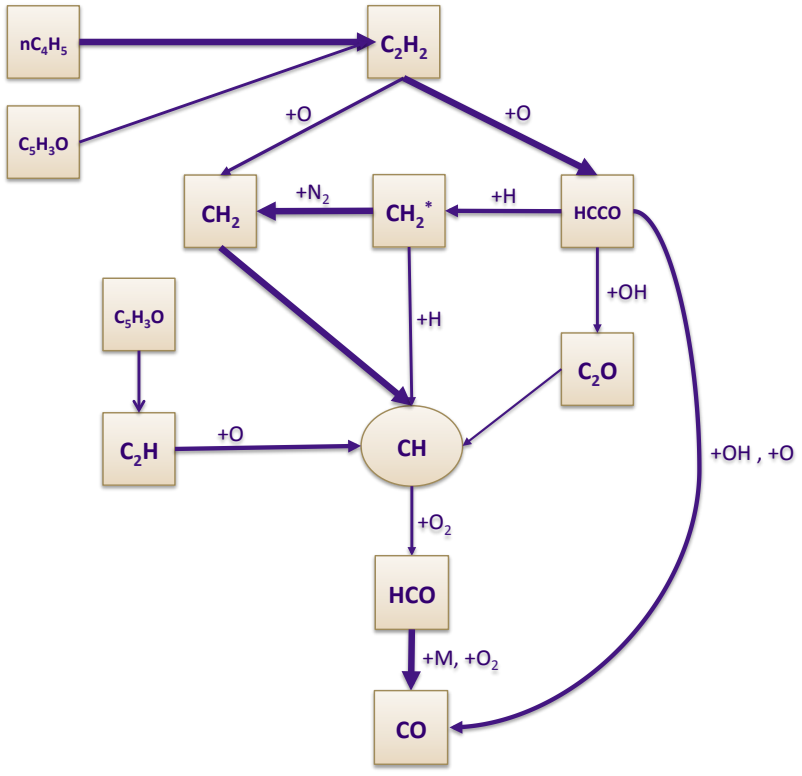

Figure D.7: CH pathway for toluene